



ON THE ORIGIN OF METALS

*Understanding the role of mixing in galactic
chemical evolution*

Dissertation submitted for the degree of

PHILOSOPHIÆ DOCTOR

to the PhD School at the Faculty of Science,
University of Copenhagen

Anne Noer Kolborg

EXAMINERS

Prof. Irene Tamborra

Prof. Kate Daniel

Prof. Sheila McBreen

SUPERVISORS

Prof. Enrico Ramirez-Ruiz

Prof. Steen Harle Hansen

PUBLICATIONS RELATED TO THIS THESIS

This thesis includes material from the following first-authored publications:

- *Supernova-driven turbulent metal mixing in high redshift galactic disks: metallicity fluctuations in the interstellar medium and its imprints on metal poor stars in the Milky Way*
Anne Noer Kolborg, Davide Martizzi, Enrico Ramirez-Ruiz, Hugo Pfister, Charli Sakari, Risa H. Wechsler & Melinda Soares-Furtado
APJL, Volume 936, Issue 2, article id. L26, 14 pp. (2022). [arXiv:2111.02619](https://arxiv.org/abs/2111.02619)
- *Constraints on the frequency and mass content of r-process events derived from turbulent mixing in galactic disks*
Anne Noer Kolborg, Davide Martizzi, Phil Macias, Melinda Soares-Furtado & Enrico Ramirez-Ruiz
Under review in the Astrophysical Journal

ACKNOWLEDGEMENTS

Completing a PhD is a marathon, not a sprint and as I approach the finish line I think back on all the people who have run with me and cheered me on from the side lines - I am fortunate that there have been many. So many that am bound to forget some in the following, to those people; I am sorry and truly grateful for your support.

First and foremost, thank you to Enrico; for giving me this opportunity, for your unwavering support, mentorship, and advice; and for your patience with me and this process, when I did not have any.

Thank you, Steen for your advice and encouragement.

There are many people who, on a daily basis, have reminded me that science is fun and astrophysicists are a really cool bunch of people; Sophie, Charlotte, Luca, Adriano, Katie, Davide, Hugo, Rosa, Sierra, Phil, James and Amanda. Thank you!

Thank you to Deana in Santa Cruz and Michelle at DARK for putting up with my many questions and requests about all things office, travel, rules and visa appointments.

A special thank you to my family; mor, far, Louise og Thor. For supporting me in changing directions and for encouraging me to follow this path.

To Nicholas, who has been by my side every step of the way. You, more than anyone, have witnessed the good, the bad and the ugly. Thank you for staying the course with me, thank you for listening when I needed to vent and thank you for being my tech support when yet an other broken python path threw a wrench in my plan. Jeg elsker dig herfra og til stjernerne.

ABSTRACT

The abundance dispersion of metal-poor stars in the halo of the Milky Way (MW) suggests that the interstellar medium (ISM) was not chemically well-mixed at early times. The degree to which turbulence, driven by core collapse supernovae (cc-SNe), mixes the metals produced in those same events should provide constraints on the local star formation conditions at the time of formation of the metal-poor stars. Furthermore, the difference in scatter observed for different elements, particularly α - and r-process elements, holds important clues to the formation processes of these elements.

The focus of this thesis has been to use a series of simulations of gas dynamics in galactic disks to isolate the processes by which cc-SNe drive turbulent mixing in the gas, with the aim of understanding how the mixing process imprints on the abundance dispersion of the gas. By resolving the metal mixing effects on parsec scales, in set-ups that mimic different galaxy types it is possible to measure the turbulent diffusion coefficient in different environments. The diffusion coefficient is an important input parameter for larger simulations which are currently forced to model mixing at a sub-grid level.

This work shows that it is possible to use the star-to-star abundance dispersion of α -elements to derive constraints for the star formation rate (SFR) of the birth environment of the metal-poor stars, and that this spread is compatible with star formation conditions in a dwarf or a low SFR MW progenitor.

This new insight into the relationship between turbulent mixing and abundance dispersion is subsequently applied to understanding the shape of the r-process element distribution. By exploring a large parameter space of rates and masses per event it is shown that the relative rate of r-process events to cc-SNe directly informs the shape of the element distribution. This is a useful result for future endeavours to constrain the

astrophysical site(s) of r-process production.

The observed star-to-star dispersion in r-process abundances can be used to constrain the the relative rate of r-process enrichment which in turn places new constraints on the expected total production rate of r-process elements in the MW. The new constraints are compatible with previous, independent measurements and constitute a significant reduction in the allowed parameter space.

Finally, the galaxy patch simulations done in this thesis are well suited to understanding the fraction of metals that are lost from galaxy systems of different masses. It is found that smaller systems, e.g. dwarf galaxies, should loose a significant fraction of new metals (both α and r-process elements), specifically for r-process enrichment this results suggests that smaller systems may require a higher rate of enrichment to explain the observed abundances.

DANSK RESUMÉ

Spredningen i metalindhold af metalfattige stjerner i Mælkevejens halo indikerer at det interstellare stof ikke var kemisk homogent tidligt i galaksens historie. Til hvilken grad turbulens, drevet af supernovaer, er i stand til at blande metallerne, som også producers i disse katastrofiske begivenheder, bør pege i retning af hvad de lokale forhold for stjernedannelse var da stjernerne blev født. Endvidere, indeholder forskellen på spredningen af forskellige grundstoffer, især α og r-process grundstofferne, vigtige spor om dannelsesprocesserne af disse stoffer.

Fokus for denne afhandling har været at anvende en række simuleringer af gas dynamik i galakseskiver til at isolere de processer hvormed supernovaer driver turbulens og derved blander gasserne, med et mål om at forstå hvordan disse blandingsprocesser indprentes på metalfordelingen. Opløsningen af simuleringerne er høj nok til at fange blandingsprocesserne i parsec størrelsesorden og ved at opstille modeller som emulerer forskellige typer af galakser, er det muligt at måle den turbulente diffusionskoefficient i forskellige miljøer. Diffusionskoefficienten er en vigtig inputparameter for større simuleringer som, på nuværende tidspunkt, er nødsaget til at behandle turbulente blandingsprocesser med sub-grid modeller.

Dette arbejde viser at det er muligt at bruge spredningen i α -metalindholdet fra stjerne til stjerne til at udlede begrænsninger for raten af stjernedannelse i de miljøer hvor de metalfattige stjerner er født, samt at denne spredning er kompatibel med stjernedannelses betingelser som dem der forventes i dværggalakser eller i en tidlig Mælkevejsgalakse med lav stjernedannelses rate.

Denne nye indsigt i forholdet mellem turbulente blandingsprocesser og metalindholdsspredningen anvendes herefter til at forstå formen af fordelingen af r-process

grundstoffer. Ved at udforske et stort parametersæt af rater og masse per begivenhed vises det at den relative rate af r-process begivenheder til supernovaer kan ses direkte på formen af r-process fordelingen. Dette er et brugbart resultat for fremtidige bestræbelser på at fastlægge det astrofysiske ophav til r-processen.

Den observerede spredning af r-process grundstoffer fra stjerne til stjerne kan bruges til at rammesætte den relative begivenheds rate, hvilket igen kan bruges til at rammesætte den forventede, samlede produktionsrate af r-process grundstoffer i Mælkevejen. Disse nye begrænsninger er kompatible med tidligere, uafhængige målinger og udgør en væsentlig begrænsning i det tilladte parameterområde.

Simuleringerne, anvendt i dette afhandlingsarbejde, er velegnede til at måle andelen af metal som forsvinder ud af en galaskeskive som funktion af galaksens masse. Det findes at mindre systemer, f.eks. dværggalakser, bør tabe en større andel af nye metaller (både α - og r-process metaller), særligt for r-process berigelse peger dette resultat på at mindre systemer muligvis kræver en højere rate af berigelse for at kunne forklare de observerede metalindhold.

CONTENTS

ACKNOWLEDGEMENTS	iii
ABSTRACT	iv
DANSK RESUMÉ	vi
CONTENTS	viii
1 INTRODUCTION	1
Motivation	1
Metal synthesis	2
The rapid neutron capture process	4
Mixing of metals	7
Supernova feedback	9
Modelling metal mixing	12
Stellar abundances	13
Stellar archaeology	14
Origin of the MW stellar halo stars	17
Open questions	17
2 SUPERNOVA DRIVEN TURBULENT METAL MIXING	19
3 R-PROCESS PRODUCTION CONSTRAINTS FROM MIXING ARGUMENTS	34
4 CONCLUSIONS & OUTLOOK	60

CONTENTS

ix

BIBLIOGRAPHY

62

INTRODUCTION

The nitrogen in our DNA, the calcium in our teeth, the iron in our blood, the carbon in our apple pies were made in the interiors of collapsing stars. We are made of starstuff.

— Carl Sagan

MOTIVATION

The Universe is made up, almost entirely, of hydrogen and helium, 74 and 24 % by mass, respectively. Less than 1% of the mass is shared among the remaining approximately 90 naturally occurring elements. Astrophysicists typically refer to this diverse group of elements simply as "metals".

Despite their universal rarity these elements are hugely important for human life; they are the iron in red blood cells, the oxygen in the air, the lithium in batteries and the gold in jewelry. Also on galactic scales does the presence of metals matter: for the evolution of a star, the initial mass function of a group of stars depends on the metal content of the gas from which they form; the masses at which stars end their lives as core collapse supernovae (cc-SNe) depends on the metal content of the star; and, the ability of a stellar system to form planets appears to require the presence of metals in the system. The aim of this thesis work has been to help shed light on why metals are distributed in

galaxies in the ways that they are, as well as, what this distribution says about the origin of, especially the heaviest, elements. The present chapter introduces the fundamental concepts necessary to understand the context of the work done in this thesis. It begins by considering the production mechanisms of groups of elements; moves on to how metals are mixed through the gaseous parts of galaxies, paying special attention to feedback from cc-SNe; before attention is turned to stars and what their metal content can teach us about the origins of metals; and about the origin of the stars themselves. The chapter closes with an outline of the open questions in the field of galactic chemical evolution and how the works presented in chapters 2 and 3 help address some of these questions. Chapters 2 and 3 are the bulk of the work of this thesis, they constitute the written work contributed to the research field. Finally, chapter 4 summarizes the work and the most important conclusions drawn from this thesis.

METAL SYNTHESIS

Figure 1.1 shows the periodic table, but instead of the familiar color coding by chemical properties of the elements, each element has been color coded by their expected astrophysical production site (Johnson, n.d.). The basis of the division of elements according to their production sites in the Universe goes back to the seminal paper by Burbidge et al. (1957) (importantly also Cameron, 1957; Suess & Urey, 1956), in which it was outlined how different groups of elements are produced in stars at various stages of their lives, as well as, how the stars return the elements to the interstellar medium (ISM). A full walk-through of all the sites of metal production is beyond the scope of this introduction, but in broad strokes the elements up to and including iron are synthesised in stars during their lifetimes (Cowan & Sneden, 2006), the more massive the star the more massive elements it is capable of synthesizing.

Among the lighter elements (between B and Fe) a group deserves special attention, these are the so called α -elements (O, Ne, Mg, Si, S, Ar, Ca and Ti), so named because their nuclear structure can be thought of as an integer number of He nuclei (α -particles), i.e. two protons and two neutrons. These elements are synthesized in massive stars and/or during the explosive burning stages of cc-SNe at the end of the massive star's life (Knödelsder, 2003), a process which also returns these metals to the ISM. Cc-SNe and the return of metals to the ISM is discussed in much greater detail under [Supernova](#)

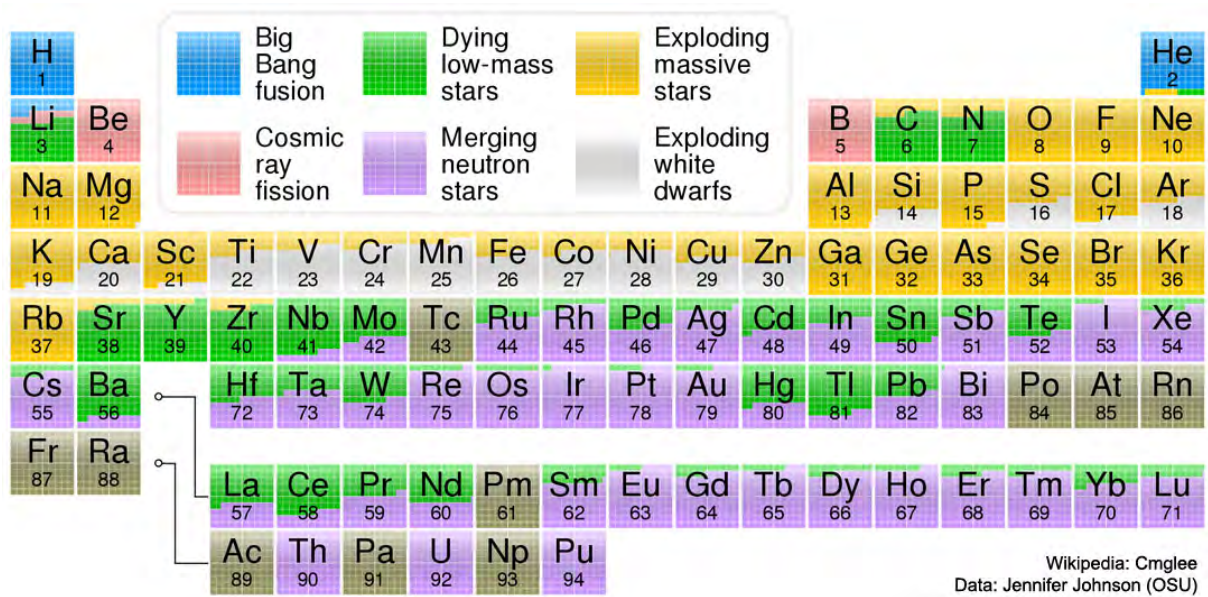


FIGURE 1.1 – The periodic table of elements. The color indicates the (likely) astrophysical production site of each element (see legend), but see the text for important nuances. Elements with multiple colors have isotopes which are produced in multiple sites, the fraction of shading by each color roughly indicates the fraction of the element mass that is produced in each site. The dark gray color (e.g. Tc) indicates elements without long-lived or stable isotopes. By Jennifer Johnson (Johnson, *n.d.*).

feedback.

The metals around iron, the iron peak elements, are also synthesized in supernova (SN) explosions, both core collapse and type Ia (Cowan & Sneden, 2006). Type Ia SNe are the end point of stars less massive than $M_{\text{ZAMS}} \lesssim 8 M_{\odot}^1$, in a binary star system. At the end of its lifetime the star will eject its envelope and leave behind a white dwarf. If its companion in the binary pair swells to a size greater than its Roche Lobe mass transfer can occur between the two stars. The transfer may push the mass of the white dwarf over the limit which can be supported by degenerate electron pressure causing thermonuclear ignition and a SN explosion.

Elements beyond the iron peak are difficult to synthesize because their high proton numbers make fusion an energetically disfavoured process (Cowan & Sneden, 2006). Instead these elements are synthesized by neutron capture, that is, the bombardment

¹ZAMS is the abbreviation for Zero Age Main Sequence and refers to the mass of the star when it begins hydrogen fusion in its core, which marks the transition from a proto-star to a main sequence star

of a nuclei with neutrons (which are electrically neutral) creating a heavy isotope of the element. These isotopes are generally unstable and will β -decay² to a stable isotope of a higher atomic number element. Based on the timescale of neutron capture to the timescale of β -decay the neutron capture process is split into two groups: the slow (s-) and the rapid (r-) process.

The s-process happens in the envelopes of Red Giant stars (the life stage following main sequence for stars less massive than $M_{\text{ZAMS}} \lesssim 8 M_{\odot}$ (e.g. Cowan & Sneden, 2006)) and produces about half the elements above the iron group (green color in Figure 1.1). The r-process has been a central theme in this thesis. The astrophysical site(s) capable of supporting this nuclear process is still widely debated. The following sections treat first the nuclear process itself in greater detail and subsequently the current best candidates for its site are introduced and discussed, with special emphasis on binary neutron star mergers and collapsars.

The rapid neutron capture process

Approximately half the elements heavier than iron are produced by the r-process. This includes notably silver, gold, thorium and uranium, among many others, indicated in purple color in Figure 1.1. Despite the long standing knowledge that these elements must be built in this nuclear process (Burbidge et al., 1957), and the apparent certainty of Figure 1.1, many open questions remain about how the process proceeds, as well as, where in the Universe the conditions are right for the process to take place.

On the nuclear physics side, knowledge about the r-process is limited by the extreme conditions required for the process to happen making it extremely difficult to study in a laboratory (e.g. Sneden et al., 2008; Cowan et al., 2021). In order for the capture of neutrons to be rapid compared to the timescale for β -decay a high density of free neutrons is required. This is a difficult thing to emulate in the laboratory which means very little experimental data exists about the exact production mechanisms of the r-process.

On the astrophysical side, the search is still on-going for one or more sites which reliably: supply the right conditions to support the r-process, eject enough mass of r-process elements, and, do so at the right time to explain the abundances of r-process

²Specifically, negative β -decay in which the atom emits an electron and an anti-neutrino, thereby, turning a neutron into a proton.

elements we observe in the galaxy (see also [Stellar abundances](#)).

Burbidge et al. (1957) proposed cc-SNe as the site of r-process production and this idea has been extensively studied since then (e.g. Woosley et al., 1994; Takahashi et al., 1994; Cowan & Thielemann, 2004; Mathews et al., 1992; Wheeler et al., 1998; Ishimaru & Wanajo, 1999). Today the census is forming that ordinary cc-SNe cannot be the site of r-process production. Simulations of cc-SN explosions indicate that the environment is not appropriate for the production of heavy r-process elements, although lighter element production may be possible (Cowan et al., 2021, and references therein). Measurements of ^{244}Pu (an r-process element) in deep sea sediments (on Earth) points at a rare source of r-process enrichment (Hotokezaka et al., 2015), which is inconsistent with the rates of cc-SNe. Furthermore, if r-process elements are produced mainly in cc-SNe one would expect the observed scatter in stellar abundances of these elements to be similar to that of α -elements, which is in strong contradiction to observations (see [Stellar abundances](#) and Figure 1.4).

Currently, two major groups of possible sites for r-process production are discussed in the research field: rare types of cc-SNe (either magneto rotational SNe with jets or collapsars) and mergers of compact objects (two neutron stars, or a neutron star and a black hole)(Cowan et al., 2021). This introduction is limited to detailed discussion of the mergers of binary neutron stars and collapsars.

Neutron star mergers A neutron star is the compact object left behind by an intermediate mass star ($M_{\text{ZAMS}} \approx 8M_{\odot} \sim 10M_{\odot}$) after it explodes as a cc-SN. As the name suggests these objects are comprised almost entirely of neutrons making them an attractive candidate for the neutron rich environment required for the r-process. When two neutron stars exist in a binary pair they may in-spiral through emission of gravitational waves and eventually merge in a binary neutron star merger ((B)NSM).

During the merger strong tidal forces tear the two neutron stars apart freeing neutron rich material and ejecting it into the ISM surrounding the binary pair (e.g. Rosswog et al., 1999; Goriely et al., 2011; Roberts et al., 2011). These events were predicted to host r-process production (e.g. Symbalisty & Schramm, 1982; Lattimer & Schramm, 1974; Rosswog et al., 2000; Goriely et al., 2011; Ramirez-Ruiz et al., 2015) and on August 17th 2017 the observation of GW170817 (AT2017gfo) (Abbott et al., 2017; Coulter et al., 2017; Murguia-Berthier et al., 2017) confirmed that indeed the merger of a pair of binary neutron stars can host r-process production and significant

masses of heavy metals can be ejected from these systems (Kasen et al., 2017; Metzger, 2017; Siegel et al., 2019; Watson et al., 2019).

Despite the observational evidence that NSM are capable of producing r-process elements questions remain about whether these events happen frequently enough to explain the total mass of heavy elements in the galaxy (Hotokezaka et al., 2018; Argast et al., 2004). This problem is exacerbated by the fact that the binary pair receives a kick when the second star explodes as a SN, these kicks can impart the system with large velocities which may cause it to escape its parent galaxy before the merger (e.g. Safarzadeh et al., 2019; van de Voort et al., 2022). Finally, NSM are challenged as the primary source of r-process production in the early Universe because of the time required for two neutron stars to form and in-spiral (e.g. Beniamini & Piran, 2019). This last point will be discussed in detail in under [Stellar abundances](#).

Collapsars A collapsar, early on also termed a failed SN, is expected to occur when massive stars ($M_{\text{ZAMS}} \gtrsim 30M_{\odot}$) explodes as a cc-SN. Due to its large size the iron core of the star is expected to also be very large, making it very difficult to explode (Woosley, 1993). Instead the core collapses to a black hole and the stellar material which is not blown away falls towards the center forming an accretion disk around the black hole (MacFadyen & Woosley, 1999). This accretion disk may be able to synthesize r-process elements (MacFadyen & Woosley, 1999; Siegel, 2019; Siegel & Metzger, 2017; Janiuk, 2017). Astronomers have yet to make unequivocal observations of this production mode in these types of explosions (Cowan et al., 2021).

Due to the large mass of the progenitor star of a collapsar these events would happen early after star formation. Furthermore, the large mass required makes these events inherently rare as more massive stars form less frequently than less massive ones (Macias & Ramirez-Ruiz, 2019; Bartos & Márka, 2019).

The preceding sections have outlined, in broad strokes, how metals are synthesized in stellar sites and how the stars return these metals to the tenuous gas between them, the ISM. Now we turn our attention to this medium itself and consider how the metals are moved through galaxies and incorporated into new stars.

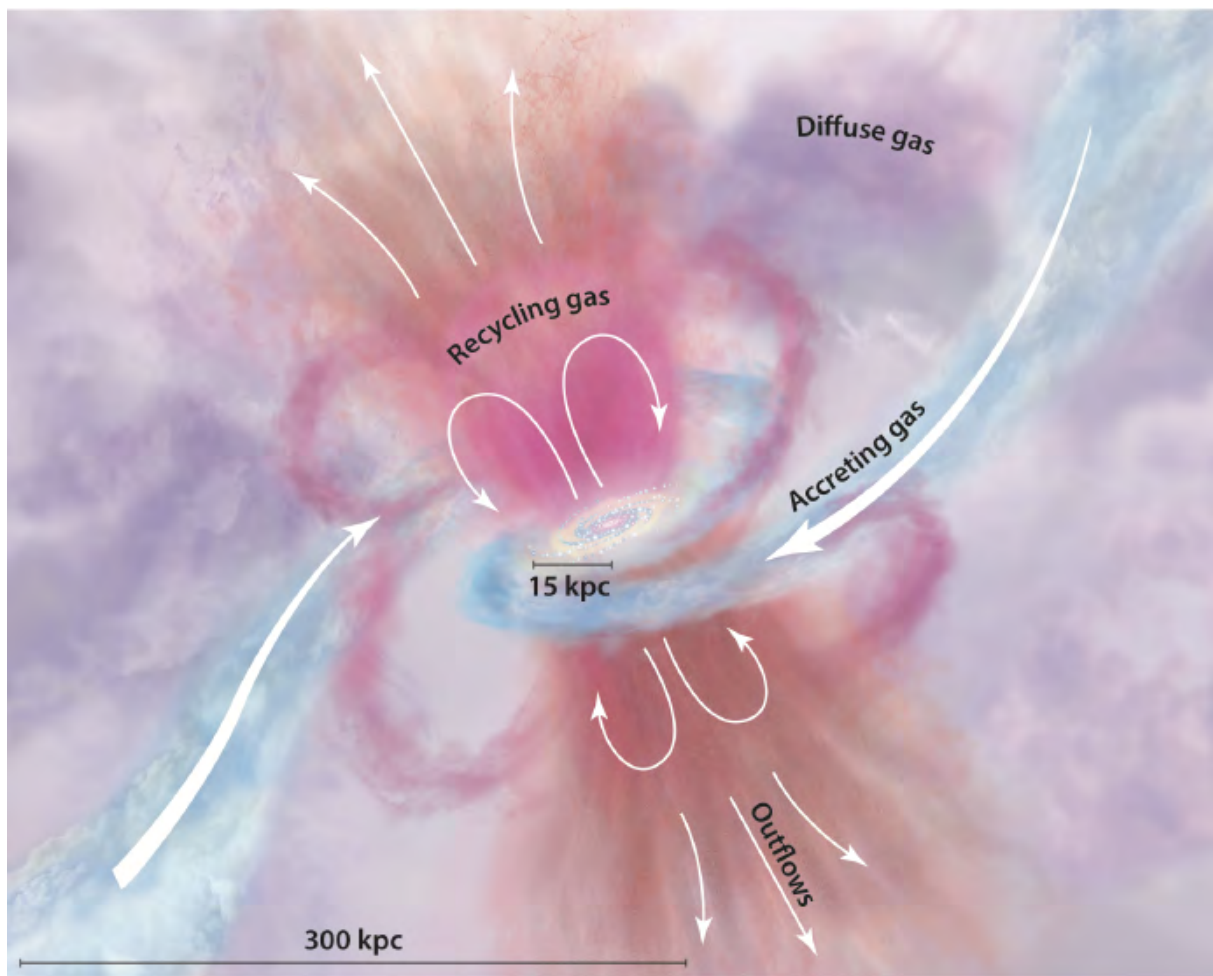


FIGURE 1.2 – Cartoon of gas mixing around a disk galaxy. The disk of the galaxy is depicted as the central ~ 15 kpc and the white arrows along with the coloring indicates how gas moves into and out of the galaxy. From Tumlinson et al. (2017).

MIXING OF METALS

As outlined above, metals are synthesized in stars and ejected into the ISM when the star dies. Once in the ISM the metals move through the galaxy or perhaps even out of the galaxy all together, dragged along by gas flow. Eventually the gas, of which the metals are a part, will cool, collapse and form a new generation of stars. This is a process that spans several orders of magnitude in both space and time.

Starting from the largest physical scales, an individual galaxy is part of a broader network of galaxies and exchanges gas with its surrounding inter galactic medium

(IGM) (see Figure 1.2). The gas accreted from the IGM generally contains fewer metals than that already in the galaxy and therefore this inflow tends to dilute the concentration of metals in the ISM. On the other hand galaxies also lose a significant fraction of their gas and metal mass on galactic winds (Dalcanton, 2007). The exact driving mechanisms behind galactic winds and the degree to which they are able to completely remove gas from a galaxy is still an actively researched topic (e.g. Fielding et al., 2017; Martizzi et al., 2016; Li & Bryan, 2020). Some of the gas that is launched out of the disk into the galactic wind is expected to return to the disk, this process is referred to as a galactic fountain (see "recycling gas" in Figure 1.2) (e.g. Tumlinson et al., 2017). Gas recycling in the galactic fountain generally does not change the overall metal concentration of the galaxy, but it does tend to even out the distribution of metals within the system by moving gas across large distances. While the exact mechanisms that launch galactic winds are not yet fully understood, contributions from SNe are expected to play a central role (e.g. Dalcanton, 2007; Martizzi et al., 2015; Martizzi et al., 2016; Fielding et al., 2017).

On intermediate to small scales, turbulence is an important mixing process within the disk of a galaxy. A turbulent fluid flow is characterized by a random, unpredictable nature, but often the statistical properties of the flow can be described. In a turbulent flow state the fluid will develop eddies, small vortices where the material circulates as it propagates. These eddies are central to how turbulence contributes to mixing processes (e.g. Scalo & Elmegreen, 2004; Pan & Scannapieco, 2010).

Figure 1.3 is a visualisation of the gas density in a turbulent flow, which highlights the eddies present in the gas. Eddies of many different sizes are apparent. The largest eddies in a flow are on the size scale of the driving mechanism of the turbulence. These large eddies break up into smaller ones, which break up into still smaller ones, down to a length scale where fluid viscosity dampens out the fluctuation. This cascade of energy from large eddies to small ones is central to understanding how turbulence leads to mixing of metals in the ISM. Essentially, the metals will travel with the fluid from the injection scale down to microscopic scales where ultimately Brownian motion of individual particles is responsible for the actual mixing (Pan & Scannapieco, 2010). Turbulence in astrophysical context can be driven by many different processes, such as; galactic rotation, shear forces and star formation. In the ISM continued injection of energy and momentum by multiple cc-SNe are important drivers of turbulence (e.g.

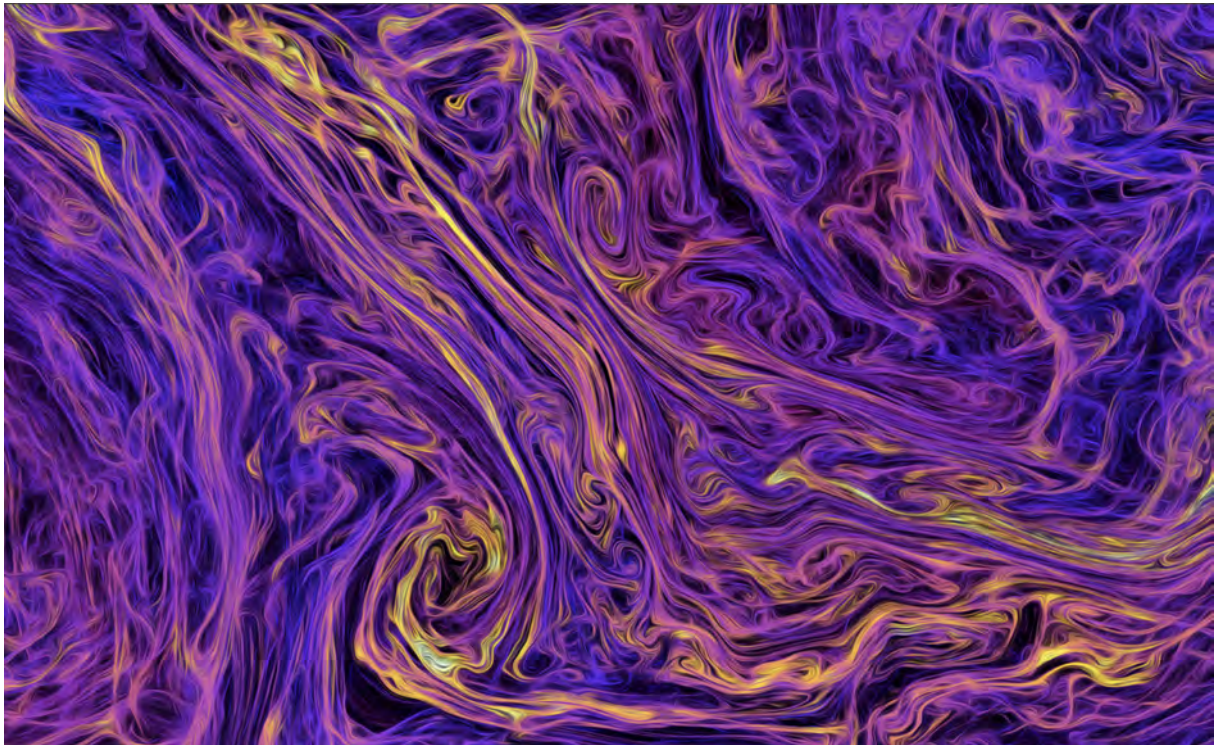


FIGURE 1.3 – Visualisation of eddies in a turbulent flow. Color indicates the logarithmic gas density. The turbulent cascade of energy from large to smaller eddies are important for mixing metals in the ISM. Image by James Beattie.

Scalo & Elmegreen, 2004, and references therein). This thesis has focused specifically on the mixing driven by SN feedback which is discussed in the following section.

Supernova feedback

Throughout its lifetime a star is kept (roughly) in hydrostatic equilibrium, supporting itself against gravitational collapse by continued injection of energy released by the fusion processes in its core. Eventually the star will reach a point at which it is no longer able to ignite the fusion process of the next element, it has run out of fuel. For sufficiently massive stars the transition from continued energy injection by nuclear burning to fusion shut-off can be very dramatic and becomes the starting point for the stellar explosion. The exact mechanism by which massive stars explode continues to puzzle the astrophysical community and efforts are still ongoing to map the exact physics responsible for the star exploding (e.g. Nomoto et al., 2013). However, the

overall picture is as follows: the sudden drop in energy injection at the center of the star causes the core to contract as the temperature drops, during this collapse of the core most of the elements synthesized during the star's lifetime disintegrate under the growing pressure as mass is pushed closer together, this collapse and disintegration continues until the atoms in the core have reduced to neutrons. Due to the Pauli exclusion principle the neutrons will strongly resist further compression causing the core to become suddenly extremely rigid. Material further out in the star does not yet "know" about this fundamental change in the matter at the center and continues to accelerate as it falls towards the middle, the abrupt resistance of the core to further collapse however causes a strong bounce. This bounce works similarly to a piston in an engine and forces the material to rapidly change direction, at speeds significantly above the speed of sound in the material, thus creating a shock front in the star. This shock front travels through the outer envelopes of the star tearing it apart.

Roughly 1×10^{53} erg of potential energy is released as the material collapses in the gravitational potential. The vast majority of this energy is radiated away as neutrinos. Only about 1% ($\sim 1 \times 10^{51}$ erg) is associated with the shock front and only about 1% of this energy (1×10^{49} erg) is observable as visible light associated with the supernova. The energy in the shock front, while constituting only a small percentage of the total energy budget of the explosion has huge implications for the star's surroundings. As the shock front travels through interstellar space it sweeps up and heats the surrounding material, forming a supernova remnant (SNR) which can be observable on the sky for hundreds of years after the explosion which caused it.

Supernova remnants The expansion of the shock front through the ISM has been extensively studied for decades (e.g. Chevalier, 1977; Kim & Ostriker, 2015; McKee & Ostriker, 1977; Taylor, 1950). While the exact behaviour of any individual remnants depends heavily on the properties of the local medium (such as density, homogeneity and metal content) (e.g. Martizzi et al., 2015) the general evolution can be categorized into a series of distinct phases.

The first of these phases is the free-expansion phase, so named because the shock front is able to propagate freely through the surrounding material as the mass of material from the star (the ejecta mass, M_{ej}) is much greater than the total mass of material swept up by the remnant (M_{swept}), it therefore presents a limited challenge to the progress

of the front which is able to expand at constant velocity. Eventually, enough material will have been swept up to begin to pose a hindrance to the evolution and the SNR enters the adiabatic expansion phase (also called the Sedov-Taylor phase) (Taylor, 1950). This phase is characterised by the formation of a shell of material at the shock front. The formation of the shell itself gives rise to an additional shock travelling backwards into the interior of the remnant (the reverse shock), heating the interior gas to high temperatures. The phase is named for the adiabatic nature of the expansion; that is, the material in the shell has not yet begun to cool significantly. However, as more and more mass is swept up cooling eventually sets in and the remnant moves into its third stage. The size of the remnant when cooling becomes important has been estimated as (Cioffi et al., 1988; Thornton et al., 1998):

$$R_{\text{cool}} \approx 14 \text{ pc} \left(\frac{n_{\text{H}}}{1 \text{ cm}^{-3}} \right)^{-3/7} \left(\frac{E_{\text{tot}}}{1 \times 10^{51} \text{ erg}} \right)^{2/7} \left(\frac{Z}{Z_{\odot}} \right)^{-1/7} \quad (1.1)$$

n_{H} is the number density of the surrounding material, E_{tot} is the energy of the shock and Z is the metallicity, the fraction of mass of metals to the total mass of gas, of the surrounding material. The onset of cooling in the shell causes the shock to begin to lose energy at a significant rate, the material in the shell will collapse slightly forming a thin, high density shell. The high pressure of the interior of the remnant (caused by the high temperatures of the rarefied gas which is unable to efficiently cool) compared to that of the cold gas outside the shell propels the shell forward and gives name to this stage of the evolution: the pressure driven snowplough phase.

As the shell continues to expand the interior pressure drops and the remnant is propelled forward less efficiently. This is the on-set of the final stage of the SNR evolution: the momentum driven snowplough phase. During this final phase the velocity of the shock front continues to drop as more material is swept up, increasing the mass of shell. Eventually the speed of the shock front drops below the sound speed, c_s , of the local medium and the remnant dissipates. The size of the remnant when it fades has can be estimated as (Draine, 2011):

$$R_{\text{fade}} \approx 67 \text{ pc} \left(\frac{n_{\text{H}}}{1 \text{ cm}^{-3}} \right)^{-0.37} \left(\frac{E_{\text{tot}}}{1 \times 10^{51} \text{ erg}} \right)^{-0.37} \left(\frac{c_s}{10 \text{ km s}^{-1}} \right)^{-2/5} \quad (1.2)$$

Through the interactions with their surroundings SNR impart energy and momentum to the ISM of a galaxy thereby leading to turbulence in the gas and contributing to the

acceleration of mass into galactic winds. As sources of new metals SNe contribute to a patchy distribution of elements in a galaxy, while simultaneously contributing to the processes by which those metals are mixed and distributed in the galaxy. Thus, they play an important dual role in the metal dispersion of the system.

Modelling metal mixing

As the preceding sections have outline the processes by which metals are mixed through galaxies span many orders of magnitude in both space and time and as such pose great problems for researchers trying to build models that adequately capture all the relevant processes at sufficient resolution. The growing capabilities of modern computers holds promise for future endeavours of ever more complete models, but in the mean time important progress can be made by breaking the problem down and studying its various components separately. This has been just the approach taken by the galactic chemical evolution community of researchers.

Beginning from the least complicated mixing models important progress on understanding the sources and rates of different metal groups can be made by ignoring mixing effects altogether. This approach is commonly referred to as instantaneous mixing models and has been applied to both α -element mixing (Matteucci & Greggio, 1986; Wheeler et al., 1989; Timmes et al., 1995; Kobayashi et al., 2006; Nomoto et al., 2013) and r-process element mixing (Ishimaru & Wanajo, 1999; Travaglio et al., 1999; De Donder & Vanbeveren, 2004; Wanajo & Ishimaru, 2006; Matteucci et al., 2014; Ishimaru et al., 2015; Vangioni et al., 2016; Côté et al., 2017; Côté et al., 2018; Côté et al., 2019). These models capture the overall evolution of individual elements in whole galaxies well (i.e. they recover the mean behaviour as a function of time or metallicity), furthermore, their comparatively lower computational costs (relative to full hydro treatment of the problem) allows for searching large parameter spaces to in order to find the best matching combinations. This is especially useful for the problem of understanding the source of r-process enrichment because combinations of many different delay time distributions can be modelled easily. However, by virtue of the assumption of instantaneous mixing, these models are not able to recover any dispersion in abundance across a galaxy, limiting their usefulness in fully constraining the sources of metals (Arnone et al., 2005).

It is possible to off-set some of the issues of the instantaneous mixing assumption by in-

incorporating a model for the mixing on smaller scales, as is done in many inhomogeneous mixing models. These types of models can be roughly divided into two groups: the semi-analytical kinds (e.g. Chiappini et al., 2001; Recchi et al., 2001; Argast & Samland, 2004; Argast et al., 2004; Dvorkin et al., 2021; Recchi et al., 2009; Cescutti et al., 2006; Spitoni et al., 2009) which incorporate a model for metal diffusion into a stochastic enrichment framework and the hydrodynamic models (e.g. Hirai et al., 2015, 2017; Hirai et al., 2022; Shen et al., 2015; Wehmeyer et al., 2015; van de Voort et al., 2015; van de Voort et al., 2020; van de Voort et al., 2022; Haynes & Kobayashi, 2019; Wehmeyer et al., 2019; Emerick et al., 2020). The hydrodynamic treatment of metals mixing in galaxies is computationally very expensive, and even for small systems (such as Ultra Faint Dwarf (UFD) galaxies) the maximum resolution achievable is often of the order $1 \times 10^3 M_{\odot}$. Below the resolution limit these models are essentially instantaneously mixing the metals and the current resolution limits therefore pose important problems for our understanding of mixing on intermediate to small scales.

The work done in this thesis aims to contribute specifically to the small body of knowledge (especially Armillotta et al., 2018; Feng & Krumholz, 2014; Yang & Krumholz, 2012; Pan et al., 2012; de Avillez & Mac Low, 2002) of how metal mixing proceeds at these intermediate scales. By isolating mixing from SNR and studying metal distributions in patches of galaxy disks it is possible to resolve the driving scales of the turbulence.

STELLAR ABUNDANCES

The previous sections outlined how metals are synthesized in stellar processes, injected into the ISM and how a subset of stars drive important feedback processes which mix the metals through the gas. However, metals also become locked up into stars when new stars form from the metal-enriched gas. Especially low mass stars, which have exceedingly long lifetimes, preserve a record of the metal content of the gas from which they formed for very long times. These stars thus provide a fossil record of the chemical evolution history of the galaxy (Frebel, 2010; Frebel & Norris, 2015). The sub-field of astronomy concerned with measuring and interpreting the patterns of abundances of old stars in the MW and its satellite galaxies has been termed stellar archaeology (Frebel, 2010) for its similarities with archaeology.

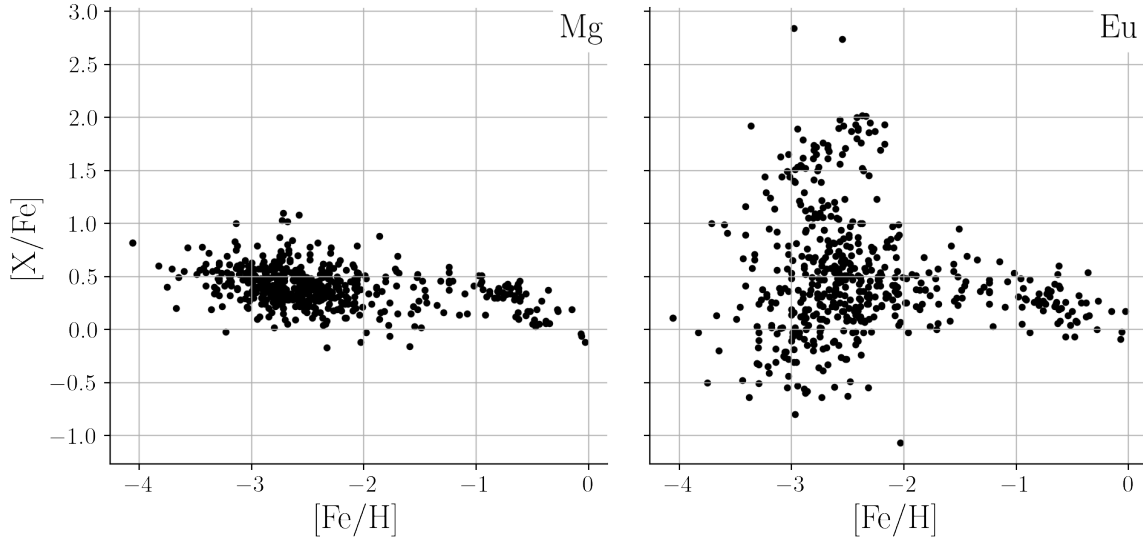


FIGURE 1.4 – Abundances of $[\text{Mg}/\text{Fe}]$ and $[\text{Eu}/\text{Fe}]$ as a function of $[\text{Fe}/\text{H}]$ in the Milky Way halo. Values are obtained from Jinabase (Abohalima & Frebel, 2018)

By "abundance" astronomers mean the amount of a given element present in a star (or gas). This is expressed as a fraction of the element, A, to another element, B (very often either H or Fe), and related to the fraction of the same elements measured in the Sun:

$$[\text{A}/\text{B}] = \log_{10} \left(\frac{N_{\text{A}}}{N_{\text{B}}} \right) - \log_{10} \left(\frac{N_{\text{A},\odot}}{N_{\text{B},\odot}} \right) \quad (1.3)$$

An accurate measurement of the amount of an element present in a given star requires a fairly high signal-to-noise spectrum of that star's light (Frebel, 2010). This sets a limit on which stars we are able to measure the abundances of, with reasonable precision. Therefore, we only have these measurements for stars in our own galaxy, as well as, a handful of individual stars in certain dwarf galaxy satellites of the Milky Way (see [Origin of the MW stellar halo stars](#)).

Stellar archaeology

Low mass stars have exceedingly long lifetimes, longer than the age of the Universe for stars with initial mass $M_{\text{ZAMS}} < 0.8M_{\odot}$ (Frebel, 2008). Because stars inherit the

metallicity of the gas from which they formed old, low mass stars preserve a record of the evolution of metals in their parent galaxy. Studying these stars we can learn a lot about the chemical history of our own galaxy (Frebel, 2008), as well as, the history of the galaxies with which it has merged during its history.

To first order the metal content of a galaxy increases with time as more stars form, fuse metals and return them to the ISM at the ends of their lives. For this reason the total metal content of a star is often used a proxy for the age of that star (e.g. Cayrel et al., 2004; Frebel, 2010). Furthermore, the $[\text{Fe}/\text{H}]$ abundance of a star is often used a proxy for the overall metal content (the metallicity) of a star (Frebel, 2008). The assumed correlation between metallicity and age is not perfect and researchers have shown that groups of stars have complicated relationships between their ages and metallicities (e.g. Xiang & Rix, 2022).

In Figure 1.4 is plotted the abundance and $[\text{Mg}/\text{Fe}]$ and $[\text{Eu}/\text{Fe}]$ of metal-poor stars in the MW halo from Jinabase (Abohalima & Frebel, 2018). Mg is often used as a representative of the α -elements, while Eu is a common representative of the r-process elements. The patterns of abundances of these two elements and what can be inferred from them are discussed in turn below.

α -elements Abundances of α -elements (e.g. Mg) show a flat trend as a function of $[\text{Fe}/\text{H}]$ for $[\text{Fe}/\text{H}] \lesssim -1$ (see left hand panel of Figure 1.4). The scatter of abundances about the mean for these elements is typically quite small (Cayrel et al., 2004; Ryan et al., 1996; Frebel & Norris, 2015). These two effects are interpreted as caused by Mg and Fe (below $[\text{Fe}/\text{H}] = -1$) both being cc-SNe products. The small scatter suggests that the chemical diversity of cc-SNe is fairly small (Frebel, 2010; Woosley & Weaver, 1995) and that the elements are generally fairly evenly distributed in the galaxy (Cayrel et al., 2004), causing most stars to form with very similar chemical abundances (Yang & Krumholz, 2012; Xiang & Rix, 2022).

At $[\text{Fe}/\text{H}] \approx -1$ there is a knee (a downwards turn in $[\text{Mg}/\text{Fe}]$). This is caused by the onset of type Ia's which contribute significantly to the Fe content of the galaxy (Frebel, 2010), but not to the α -elements, leading to the downward turn in $[\alpha/\text{Fe}]$. The $[\text{Fe}/\text{H}]$ abundance at which this knee happens is different for galaxies with different star formation histories (SFH) (Robertson et al., 2005). This happens because the off-set in time between when cc-SNe begin and when type Ias begin is similar across different galaxies (the physical processes are the same), however, the total number of stars that

form in the galaxy influences how many cc-SNe will happen before the first Ia is likely to happen and this directly influences how much Fe is mixed into the galaxy when Ias begin to contribute to the Fe content. Thus, in smaller systems where fewer stars form and fewer cc-SNe are likely to happen before the first type Ia, the knee will tend to move to lower $[\text{Fe}/\text{H}]$.

R-process elements While the α -elements show a clear trend with a small, constant scatter over a wide range of $[\text{Fe}/\text{H}]$ abundances the same is not true for the r-process elements (Frebel, 2008; Hansen, 2022). Eu is often used as a representative of the r-process elements, because this element is synthesized, almost exclusively, by the r-process (see Figure 1.1), the abundance of $[\text{Eu}/\text{Fe}]$ as a function of $[\text{Fe}/\text{H}]$ (see right hand panel of figure 1.4) does not have a well constrained trend and shows very large scatter, especially at low $[\text{Fe}/\text{H}]$. These patterns hint several things about the source of r-process.

The first is that the presence of r-process enhanced stars at very low metallicities indicates that the site of r-process production must occur early in the history of the Universe and not long after star formation (Cowan & Sneden, 2006; Sneden et al., 2008; Thielemann et al., 2017).

Second, the pattern of the spread; large at low $[\text{Fe}/\text{H}]$ and declining with increasing metallicity, suggests that the r-process elements were less evenly distributed in the galaxy compared to α -elements (e.g. Cayrel et al., 2004; Arnone et al., 2005; McWilliam et al., 1995; Cowan & Sneden, 2006). It has been argued that this difference is likely caused by the source of r-process elements happening much less frequently than the cc-SNe (Frebel, 2008).

Finally, $[\text{Eu}/\text{Fe}]$ also has a knee at $[\text{Fe}/\text{H}] \approx -1$ suggesting that the site of r-process production cannot have the same delay time distribution as type Ias (if this were the case Eu and Fe would increase in step with one another and lead to no change in mean abundance) (Côté et al., 2017; Côté et al., 2018; Côté et al., 2019; Simonetti et al., 2019).

Robustness of r-process Comparing the abundance patterns of multiple low metallicity, r-process enhanced stars can teach us a great deal about how the r-process operates. Firstly, the patterns of abundance of r-process elements is remarkably similar across stars with very different metallicities (Frebel, 2010; Barklem et al., 2005; Sneden et al., 1996; Cowan & Sneden, 2006). This suggests that the r-process elements are synthesized

in very similar relative abundances wherever the r-process may happen. There is some scatter among the lower atomic mass r-process elements ($Z < 56$, the so-called first peak r-process elements) (Cowan & Sneden, 2006; Cowan et al., 2021) which has been interpreted as evidence that perhaps more than one astrophysical site is capable of producing the lighter r-process elements.

Origin of the MW stellar halo stars

In order to correctly interpret the chemical history of a galaxy using the abundances of metal poor stars it is necessary to know where those stars formed. Increasingly, evidence is mounting that a significant fraction of the stars in the MW halo were not in fact born in the MW (in-situ formation (Eggen et al., 1962)) but instead formed in smaller satellite galaxies which subsequently merged with the MW (ex-situ formation (Searle & Zinn, 1978)).

This is predicted by the hierarchical structure formation theory and many cosmological simulations have shown this accretion to occur (e.g. Johnston et al., 2008; Robertson et al., 2005; Wang et al., 2021; Bullock et al., 2001; Deason et al., 2016). More recently the wealth of kinematic data provided by the GAIA-ESO Survey (Gilmore et al., 2012) has allowed astronomers to group stars with similar kinematic properties suggesting a common origin for those stars (Naidu et al., 2021; Shank et al., 2022; Xiang & Rix, 2022; Roederer et al., 2018; Santistevan et al., 2021).

Observations of stars in dwarf galaxies in the MW halo suggest that most of these systems are not strongly enriched in r-process elements (e.g. Ji et al., 2019), notable exceptions to this are Reticulum-II (Ji et al., 2016) and Tucana-III (Beniamini et al., 2016) both of which show strong r-process enhancements.

OPEN QUESTIONS

The preceding sections have outlined, in a general sense, the current state of the field of galactic chemical evolution, focusing on SNe feedback, metal mixing and the astrophysical site of r-process production. This section outlines some open questions in the field which this thesis work contributes towards the answers of.

Different elements are synthesized in different astrophysical sites and the abundance dispersion of metal poor stars should be tied to the degree of mixing of that element in

the ISM at the time of star formation. However, the exact relationship between mixing and dispersion is not well understood, partly because mixing is a multi-scale process which requires high resolution simulations to be adequately captured. Cosmological zoom-in simulations and isolated disk galaxy simulations still struggle to achieve the required resolution and hence sub-grid models of mixing are employed. But these models mask the underlying relationships. By simulating patches of galactic disks and isolating the physics relevant to mixing on these scales the work in this thesis aims to shed light on the relationship between mixing processes and element abundance dispersion.

Because the rate of cc-SNe is closely tied with the rate of star formation, due to the short lifetimes of the cc-SNe progenitor stars, and cc-SNe are important drivers of metal mixing there may be a close link between the SFR of galaxy and the α -element dispersion of the stars which formed from that gas. Such a relationship holds great promise for characterising the birth environments of kinematically tagged groups of stars in the MW halo. The work presented in Chapter 2 uses the well understood α -elements to study the relationship between SNe-driven mixing processes and stellar abundance dispersion.

In Chapter 3 the focus is shifted from understanding the mixing process itself to understanding what it indicates about the origin of heavy elements, specifically the r-process elements. As the previous sections have outlined many open questions exist about the astrophysical site of r-process production. Playing to the strengths of the galaxy patch simulations done in this work focus has been on the dispersion of these elements. Similarly, to the α -elements the rate of enrichment and metal mass per enrichment event are expected to carry over into the shape of the element distributions, although the exact relationship has so far not been well characterised.

The MW halo stars are expected to originate, at least in part, from smaller galaxy systems (dwarfs or UFDs) that have been accreted by the MW. As such the ability of these systems to retain the metal mass from cc-SNe and NSM has important implications for our interpretation of the abundances of the MW halo stars. The fraction of gas and metal mass that is lost from dwarf galaxy systems has important implications for the expected abundances of the gas that remains in the system. The work presented in both Chapters 2 and 3 contributes to our understanding of how cc-SNe may be launching galactic winds and driving both α - and r-process elements out of dwarf galaxies.

SUPERNOVA DRIVEN TURBULENT METAL MIXING

This chapter includes the following article:

Supernova-driven Turbulent Metal Mixing in High-redshift Galactic Disks: Metallicity Fluctuations in the Interstellar Medium and its Imprints on Metal-poor Stars in the Milky Way

Published in The Astrophysical Journal Letters (ApJ Letters), 936, 2, id.26, 14 pp. (2022).

Authors: Anne Noer Kolborg, Davide Martizzi, Enrico Ramirez-Ruiz, Hugo Pfister, Charli Sakari, Risa H. Wechsler and Melinda Soares-Furtado



Supernova-driven Turbulent Metal Mixing in High-redshift Galactic Disks: Metallicity Fluctuations in the Interstellar Medium and its Imprints on Metal-poor Stars in the Milky Way

Anne Noer Kolborg^{1,2} , Davide Martizzi^{1,2} , Enrico Ramirez-Ruiz^{1,2} , Hugo Pfister^{1,3} , Charli Sakari⁴ ,
Risa H. Wechsler^{5,6} , and Melinda Soares-Furtado^{7,8}

¹ Niels Bohr Institute, University of Copenhagen, Blegdamsvej 17, DK-2100 Copenhagen, Denmark; anne.kolborg@nbi.ku.dk

² Department of Astronomy & Astrophysics, University of California, Santa Cruz, CA 95064, USA

³ Department of Physics, The University of Hong Kong, Pokfulam Road, Hong Kong, People's Republic of China

⁴ Department of Physics & Astronomy, San Francisco State University, 1600 Holloway Avenue, San Francisco, CA 94132 USA

⁵ Kavli Institute for Particle Astrophysics and Cosmology and Department of Physics, Stanford University, 382 Via Pueblo Mall, Stanford, CA 94305, USA

⁶ Kavli Institute for Particle Astrophysics and Cosmology, SLAC National Accelerator Laboratory, 2575 Sand Hill Road, Menlo Park, CA 94025, USA

⁷ Department of Astronomy, University of Wisconsin-Madison, 475 N. Charter Street, Madison, WI 53703, USA

Received 2021 November 3; revised 2022 August 15; accepted 2022 August 22; published 2022 September 12

Abstract

The extent to which turbulence mixes gas in the face of recurrent infusions of fresh metals by supernovae (SN) could help provide important constraints on the local star formation conditions. This includes predictions of the metallicity dispersion among metal-poor stars, which suggests that the interstellar medium was not very well mixed at these early times. The purpose of this *Letter* is to help isolate, via a series of numerical experiments, some of the key processes that regulate turbulent mixing of SN elements in galactic disks. We study the gas interactions in small simulated patches of a galaxy disk with the goal of resolving the small-scale mixing effects of metals at parsec scales, which enables us to measure the turbulent diffusion coefficient in various galaxy environments. By investigating the statistics of variations of α elements in these simulations, we are able to derive constraints not only on the allowed range of intrinsic yield variations in SN explosions but also on the star formation history of the Milky Way. We argue that the observed dispersion of $[\text{Mg}/\text{Fe}]$ in metal-poor halo stars is compatible with the star-forming conditions expected in dwarf satellites or in an early low-star-forming Milky Way progenitor. In particular, metal variations in stars that have not been phase-mixed can be used to infer the star-forming conditions of disrupted dwarf satellites.

Unified Astronomy Thesaurus concepts: [Stellar feedback \(1602\)](#); [Galaxy formation \(595\)](#); [Milky Way formation \(1053\)](#); [Galaxy mergers \(60\)](#); [Metallicity \(1031\)](#); [Chemical abundances \(224\)](#); [Interstellar medium \(847\)](#)

1. Introduction

The distribution of chemical abundances in stars serves as a “fossil record” of the Galaxy’s evolutionary history and provides clues about the types of nucleosynthetic processes that occurred early in the history of the Milky Way (MW). Of particular interest for core-collapse supernova (cc-SN) enrichment is the α element composition of Galactic halo stars. In the metallicity regime $[\text{Fe}/\text{H}] \approx -4.0$ to -2.0 (e.g., Audouze & Silk 1995; Macias & Ramirez-Ruiz 2018), α elements have been found to be pure core-collapse products with a fairly characteristic $[\alpha/\text{Fe}]$ abundance ratio but with a star-to-star bulk scatter in their $[\alpha/\text{H}]$ concentrations (Ryan et al. 1996; Cayrel et al. 2004; Frebel & Norris 2015). The presence of these elements demonstrates that their synthesis operated in a fairly robust manner in the early MW while their abundance dispersions should yield clues about the formation rate of the massive stellar progenitor systems that lived and dwindled before them. The reason is that metal injection rates can help establish how chemically unmixed and inhomogeneous the interstellar medium (ISM) was when these stars formed

(Audouze & Silk 1995; Krumholz & Ting 2018). At later times, these localized inhomogeneities are expected to be smoothed out as more events take place and cc-SN products are given more time to migrate and mix throughout the progenitor galaxy (de Avillez & Mac Low 2002; Pan et al. 2013; Krumholz & Ting 2018).

To this end, a comprehensive understanding of the inhomogeneous enrichment of the ISM holds great promise for our attempts to decipher the MW’s stellar assembly history (e.g., Wang et al. 2021) and, in particular, the origin of halo stars. The relative contribution between stars formed in situ (e.g., Eggen et al. 1962) and those formed ex situ (e.g., Searle & Zinn 1978) to the MW halo has been long debated. While recent studies of the respective importance of these different star formation (SF) channels to the halo have primarily supported ex situ assembly (e.g., Robertson et al. 2005; Johnston et al. 2008), a comprehensive picture remains elusive and a series of issues are still pressing, in particular issues concerning the specific merger and star formation histories (SFHs) of the individual satellite galaxies.

Comprehensive numerical modeling aimed at addressing the mixing of metals in the MW requires a suite of codes to treat the diverse range of physics and timescales at play. Simulations performed in a cosmological context (e.g., Few et al. 2014; Shen et al. 2017; Naiman et al. 2018) are required to capture the large-scale mixing mechanisms including satellite mergers, gas inflows, galactic winds and fountains, and shearing disk

⁸ NASA Hubble Postdoctoral Fellow.



Table 1
Parameters for all the Galaxy Models Examined in this Project

Galaxy type	Σ_{gas} $M_{\odot} \text{ pc}^{-2}$	$\dot{\Sigma}_{\text{SFR}}$ $M_{\odot} \text{ kpc}^{-2} \text{ Myr}^{-2}$	Γ $\text{kpc}^2 \text{ Myr}^{-1}$	f_{gas}	ρ_0 g cm^{-3}	L pc	z_{eff} pc	$\langle \sigma_v \rangle$ km s^{-1}	t_r Myr	κ pc km s^{-1}
MW progenitor, high SFR	50	3×10^4	300	0.100	3.47×10^{-23}	1000	40	11	19	147
MW progenitor, low SFR	5	1×10^3	10	0.088	2.08×10^{-24}	1000	80	8	39	213
Satellite galaxy	5	8×10^2	8	0.496	4.67×10^{-25}	4000	365	12	120	1460
MW progenitor, low ϵ_*	5	2×10^2	2	0.088	2.08×10^{-24}	1000	80	4	73	107
High redshift, high ϵ_*	5	5.5×10^3	55	0.088	2.08×10^{-24}	1000	80	14	23	373

Note. The results of the supporting simulations (in gray) are presented in Appendix B. Columns are: Simulation Name, Gas Surface Density, Star Formation Rate Surface Density, Surface Density of Rate of SNe ($\Gamma = \dot{\Sigma}_{\text{SFR}}/100M_{\odot}$), Fraction of Gas Mass to Stellar Mass, Initial Density of Gas in the Midplane of the Disk, Simulation Box Size, Effective Scale Height of the Disk, Mean Velocity Dispersion of the Gas, Characteristic Relaxation Time, and Turbulent Diffusion Coefficient.

instabilities, all of which are unquestionably important to comprehend the enrichment and dissemination of metals. On the other hand, as cosmological simulations today are limited by resolutions of a few tens to hundreds of parsecs, they inevitably entail “subgrid” models for turbulent mixing, SF, and stellar feedback. As such, ample uncertainties still exist at the 100 pc scale. For turbulent mixing, the trade-offs are even more pronounced and require a large range of scales to be resolved simultaneously (e.g., de Avillez & Mac Low 2002; Yang & Krumholz 2012; Colbrook et al. 2017). As a consequence, a single simulation of the full problem incorporating all the aforementioned effects would not only be prohibitively expensive but also difficult to interpret because of the complexity of the interplay between the various physical mechanisms at different scales. Instead, in this *Letter* we study the inhomogeneous enrichment of the ISM via a series of numerical experiments that isolate the key processes that regulate the mixing of SN elements into the ISM.

In addition to being computationally feasible, this approach enables a thorough understanding of the relevant processes. To this end, we present models that study the gas interactions in small patches of a galaxy disk in order to study the small-scale mixing effects of metals at parsec scales from SN into the ISM. Resolving the cooling length of individual SN remnants allows us to self-consistently capture the mixing of metals in the ISM, which enables us to calculate the turbulent diffusion coefficient in various galaxy environments. Additionally, investigating the distribution of α elements in these simulations and comparing them with the observational data can, in turn, provide useful constraints on the star-forming conditions (Audouze & Silk 1995; Armillotta et al. 2018) within the early MW and/or the infalling satellites that built up the stellar halo. Given the relatively nascent stage of modeling in the field, the results we present in this *Letter* amount to a considerable improvement in our understanding of the physical mechanism leading to the inhomogeneous enrichment of the ISM and the mixing of α elements in the early MW.

2. Methods and Metal Mixing Experiments

We use the hydrodynamical, adaptive mesh refinement (AMR) code RAMSES (Teyssier 2002) to model the gas interactions in small patches of a galaxy disk to study the small-scale mixing effects of metals from SNe into the ISM. The simulation setup is described in detail in Martizzi et al. (2016) and here we summarize the salient features and provide details for those aspects of the setup that are different to their investigations.

The setup studies small patches of galaxy disks at relatively high resolution. In particular, we are able to capture the momentum injection and thermal energy of individual SNe, as the cooling phase of individual remnants is well resolved. By changing the parameters of the gravitational potential, gas fraction, gas density, and star formation efficiency (ϵ_*), we are also able to replicate the characteristics of different local galactic environments that might be representative of the early MW or its accreted satellites.

For the purposes of this *Letter* we have chosen to focus on two different possible MW progenitors as well as one likely satellite candidate. The MW progenitors are chosen to model two different high-redshift cases. One is a gas-rich, highly star-forming model (van Dokkum et al. 2013; Shen et al. 2015; Naiman et al. 2018). The other one has a lower star formation rate (SFR) and is motivated by the recent findings of Wang et al. (2021), whereby the presence of the Large Magellanic Cloud (LMC) satellite hints at a MW progenitor with a less vigorous SFR. Finally, we include a dwarf-like satellite galaxy in order to examine the viability of an ex situ birth environment for the halo stars. In order to study how mixing is altered by changes in the gas-to-light ratio, we have also run two additional versions of the low-SFR MW progenitor model with the same gas density but with two different star formation efficiencies. The results of these additional simulations are included in Appendix B. Table 1 summarizes the parameters of all the models used in this work.

The size of the computational domain changes between different models. It increases for the satellite galaxy simulation to accommodate the larger scale height of the disk, which is caused by the reduced gravity of the galaxy. We use a regular Cartesian grid (all cells within the box have the same physical size but not the same mass resolution) and fix the resolution at 2^8 cells. This is sufficient to ensure that the cooling radius is resolved by at least a few resolution elements for the majority of the supernova remnants (SNR) in all models. The cooling radius is calculated using (Martizzi et al. 2016):

$$R_c \approx 14 \left(\frac{n_{\text{H}}}{1 \text{ cm}^{-3}} \right)^{-3/7} \left(\frac{E_{\text{SNe}}}{10^{51} \text{ erg}} \right)^{2/7} \left(\frac{Z}{Z_{\odot}} \right)^{-1/7} \text{ pc}. \quad (1)$$

In each model the percentage of SNe that are not resolved by at least 2 (5) cells at their cooling size are: MW progenitor, high SFR 0.6% (6.1%); MW progenitor low, SFR 0% (1.6%); and satellite galaxy 0% (3.8%).

The SNe are seeded following the “fixed” distribution scheme used in Martizzi et al. (2016); in this framework a scale

height for explosions is defined and the SNe have equal probability of happening anywhere in the volume contained within this height and zero probability outside. In all the models used here, this height is twice the gaseous scale height of the disk ($z_{\text{SNe}} = 2z_{\text{eff}}$); z_{eff} is defined in Section 3.1. Each SN injects a mass of $M_{\text{ej}} = 6.8 M_{\odot}$ and an energy of $E_{\text{SNe}} = 10^{51}$ erg. This energy is partitioned into thermal energy and momentum injection using the subgrid model of Martizzi et al. (2016), which also distributes the mass among the neighboring cells of the explosion. The rate of SNe per unit area, Γ , is given by the SFR as $\Gamma = \frac{\Sigma_{\text{SFR}}}{100 M_{\odot}}$.

The evolutionary timescale (t) of each simulation is dictated by the SFR and differs between simulations in order to account for the gentler evolution of galaxies with lower surface densities of gas (efficient cooling is impaired) and lower rate of SNe (feedback is reduced). The time between consecutive snapshots (δt) is also adjusted to ensure that there are not too many SNe happening in each snapshot, i.e., models with higher rates of SNe have lower δt . This allows us to follow the interaction between the remnant and the ISM more closely. The specific time intervals are: MW progenitor, high SFR: $\delta t = 5 \times 10^4$ yr; MW progenitor, low SFR: $\delta t = 5 \times 10^4$ yr; and satellite: $\delta t = 1 \times 10^5$ yr.

2.1. Metal Injection

We monitor individual elements as passive scalars. For the purposes of this *Letter* we focus on Mg (as our representative α element, see Appendix A) and Fe (as a tracer of the global metallicity), in relation to the background element H. Metals are introduced into the gas by SNe, which are initially assumed to be chemically identical. An assumption that we relax to include intrinsic SN yield variations.

In the first case, each SN yields masses of $M_{\text{Mg}} = 0.10 M_{\odot}$ and $M_{\text{Fe}} = 0.08 M_{\odot}$. These values are chosen to achieve a yield ratio of $\frac{M_{\text{Mg}}}{M_{\text{Fe}}} = 1.27$, equivalent to the best fitting value for the observational set we wish to compare with (see Appendix A). This approach is similar to assuming that the mean abundances are fixed by the mean yields, which is a commonly used conjecture when studying metal mixing (e.g., Dalcanton 2007). This allows us to isolate the effects that turbulent mixing has on the abundance spread of metals within the ISM.

After studying the mixing of Fe as a function of the global mean $[\text{Fe}/\text{H}]$ abundance, $\langle [\text{Fe}/\text{H}] \rangle$, in simulations with no intrinsic spread in SN yields, we then proceed to alter the $[\text{Mg}/\text{Fe}]$ yields. We do this by introducing an intrinsic spread in yields from SN to SN. This assumption is supported by our finding in Figure A3 that the spread in $[\text{Mg}/\text{Fe}]$ can only be produced by altering the SN yields. We model the yield variation by introducing two types of SNe with different $[\text{Mg}/\text{Fe}]$ yields. We choose these yields such that their mean corresponds to the mean $[\text{Mg}/\text{Fe}]$ abundance of the observational data set in the metallicity range $-3.5 < [\text{Fe}/\text{H}] \leq -1.0$. This range of metallicity was selected in order to exclude a handful of very-low-metallicity stars with large associated uncertainties and to ensure that the chosen range is wider than the range of metallicities within which the simulations are evaluated (Figure 1 and Section 4.2). The higher yield value in the spread is chosen to be similar to the most highly enriched star in the sample, and the lower yield value is then fixed such that the desired mean is achieved. This results in yield values of

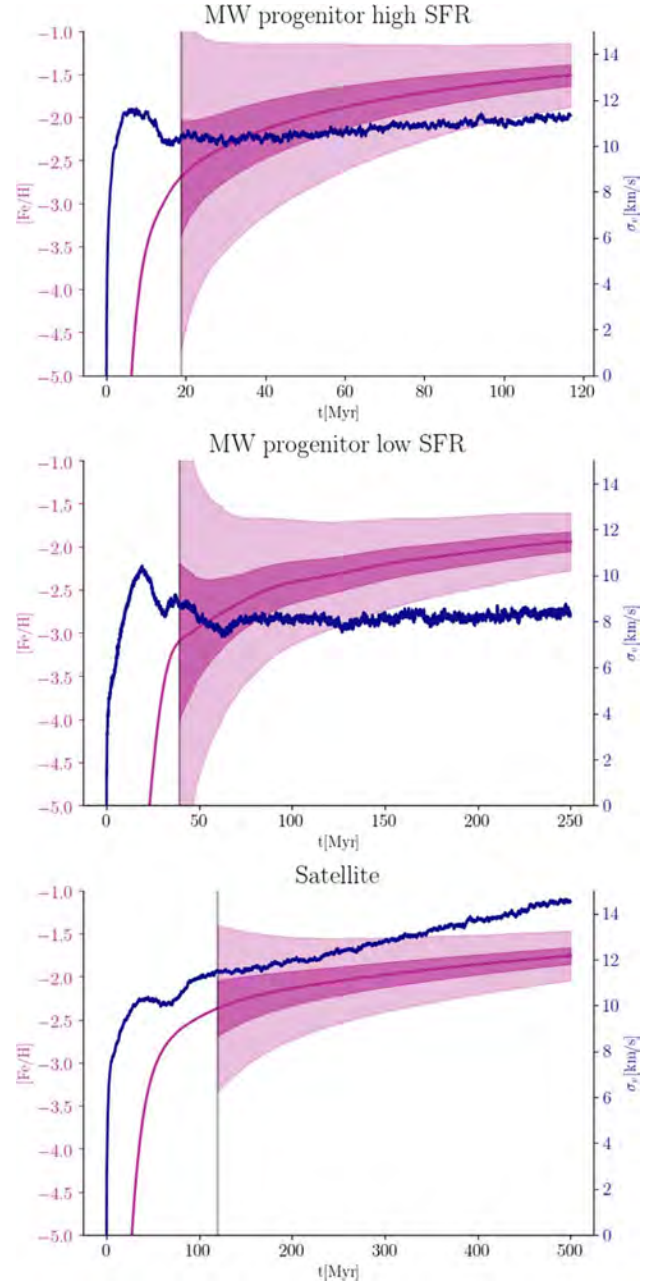


Figure 1. Evolution of the velocity dispersion, σ_v (blue) and the mean $[\text{Fe}/\text{H}]$ abundance ($\langle [\text{Fe}/\text{H}] \rangle$; purple line) as well as 1σ and 3σ spreads (shaded regions) as a function of time. The relaxation time, t_r , for each model is marked by the vertical gray line in each panel. The panel titles indicate the simulation. Models with lower SFR have a more slowly evolving $\langle [\text{Fe}/\text{H}] \rangle$ but tend to have smaller spread at the same mean abundance as models with higher SFR.

$[\text{Mg}/\text{Fe}] = 0.72$ and $[\text{Mg}/\text{Fe}] = -1.39$ for the two types of SN injection sites.

The reader is referred to Section 4.2 for a discussion on the implications of our findings in the context of abundance determinations of metal-poor stars. One key aspect of the comparison between our simulations and the observations is that we are directly comparing how the spread in $[\text{Mg}/\text{Fe}]$ evolves with the $\langle [\text{Fe}/\text{H}] \rangle$, which is initially sensitive to the assumed SN-to-SN yield variance and is then subsequently smoothed out by turbulent diffusion.

3. Simulating Supernova Feedback and Mixing in Galaxy Disk Patches

3.1. Steady State

The early time of the simulations is characterized by a relaxation from the initial conditions. Initially the disk is supported by thermal pressure, while at later times the disk is supported in part by turbulent pressure. As a result, the true effective scale height differs slightly from what one would calculate assuming hydrostatic equilibrium with the unchanging gravitational potential. To address this, Martizzi et al. (2016) defined the effective scale height, z_{eff} as:

$$z_{\text{eff}} = \frac{\Sigma_{\text{gas}}}{2\rho_0} = \frac{1}{2\rho_0} \int_{-L/2}^{L/2} \rho_{\text{gas}}(z) dz,$$

where Σ_{gas} is the surface density of gas, and ρ_0 is the gas density in the disk midplane during initial conditions. Both ρ_0 and z_{eff} are listed in Table 1 for all models.

We use z_{eff} to define a characteristic relaxation time, t_r , for our disk models:

$$t_r = \frac{4z_{\text{eff}}}{\langle\sigma_v\rangle}, \quad (2)$$

$\langle\sigma_v\rangle$ is the time averaged, mass-weighted velocity dispersion of the gas. We calculate the mass-weighted velocity dispersion as:

$$\sigma_v = \sqrt{\frac{\sum_i^N (\mathbf{v}_i - \langle\mathbf{v}\rangle)^2 M_i}{\sum_i^N M_i}},$$

where N is the number of cells in the simulation volume, M_i is the mass of gas in the cell, \mathbf{v}_i is the gas 3D velocity, and $\langle\mathbf{v}\rangle$ is the mean velocity of the gas. The parameter $\langle\sigma_v\rangle$ is set by the properties of the turbulence in the disk and depends weakly on the surface density of gas (Martizzi et al. 2016). The evolution of the velocity dispersion is shown in Figure 1. We calculate the mean of the velocity dispersion over the entire evolution time of the model and report this value in Table 1.

The factor of 4 in Equation (2) is a choice we made to ensure that information has been communicated effectively to all regions and that turbulent motions in the bulk of the disk reach a statistical steady state (Martizzi et al. 2016). This choice is validated by comparing the evolution of the velocity dispersion before and after t_r ; in almost all cases the velocity dispersion has a fairly gradual (or even flat) development after the relaxation time and a much more volatile development before (Figure 1). This dynamical timescale results from complex interplay between the gas density, the shape of the gravitational potential, and the SFR. For instance, when the gas density increases, the disk tends to relax more promptly, because as gas cools it comes into a quasi-equilibrium with the gravitational potential and higher-density gas will cool more efficiently thus reaching steady state sooner. This process is nicely exemplified in the top and middle panels of Figure 1. In Appendix B we compare models with the same gas density and gravitational potential but varying SFR; here we find that t_r increases with increasing SNe feedback. In all cases we find that steady state is reached at $t \approx t_r$. In the remainder of this work, we only show results for $t > t_r$, when turbulent motions in the bulk of the disk have reached a statistical steady state.

In both MW progenitor cases, the velocity dispersion flattens out at or soon after the relaxation time, indicating that these

models are dynamically stable over long periods of time. The dwarf model however shows a continually increasing velocity dispersion with time, indicating that this model is in fact not dynamically stable. Over the course of the simulation, the dwarf model loses $\approx 35\%$ of its initial mass in SNe-driven winds. In comparison, the two MW progenitor models lose $\lesssim 5\%$. This behavior is consistent with what is routinely observed when modeling dwarf galaxy systems (e.g., Mac Low & Ferrara 1999; Fragile et al. 2003; Fielding et al. 2017). We see a similar behavior in the MW progenitor with low SFR and high ϵ_* (see Appendix B), which loses $\approx 10\%$ of its mass to SNe-driven winds during its lifetime.

3.2. Connecting Metal Abundance Variations to Star-forming Gas Conditions

Over time, the material within the disk is progressively enriched as subsequent SNe increase the mean metallicity of the gas. At the same time, SNe drive turbulent mixing, which causes the metals to spread from their localized injection sites. In general, models with fewer SNe take longer to arrive at the same mean metallicity. As such, their products are given more time to migrate throughout the disk. This implies that galactic disks with lower SFRs show more homogeneity at a comparable average abundance. This can be seen in the evolution of $\langle[\text{Fe}/\text{H}]\rangle$ shown in Figure 1.

$[\text{Fe}/\text{H}]$ is often used, for convenience, as a rough proxy for age when thinking about the assembly of metal-poor stars (e.g., Cayrel et al. 2004; Frebel 2010). This relation is shown in Figure 1 and is, as expected, nonlinear. Thus, a given galaxy disk patch spends significantly longer time at higher abundance values than at lower ones. This relationship is useful to keep in mind as we study the scatter in $[\text{Fe}/\text{H}]$ of the gas at a given $\langle[\text{Fe}/\text{H}]\rangle$.

In all simulations, an early, chemically unmixed and inhomogeneous galactic disk is observed. As time evolves, these localized inhomogeneities within the gas are smoothed out as more events take place and SN products are granted more extended periods to migrate and mix across the disk. Figure 2 shows slice maps for each of the three galaxy models considered in this work. Individual SNR are clearly visible as pockets of lower-density (higher-pressure) gas with high metal abundances. The influence of the density and density gradients is also clearly seen when comparing between different models. The lower-density gas of the MW progenitor with low SFR allows each remnant to reach larger physical sizes than remnants in the higher-density environment of the MW progenitor with high SFR, leading to a higher degree of homogeneity in the $[\text{Fe}/\text{H}]$ abundance of the gas at given $\langle[\text{Fe}/\text{H}]\rangle$ in the lower SFR models. In Appendix B we show that for identical surface density of gas (and galaxy potential) a lower rate of SNe also leads to a higher degree of homogenization of the gas at a given mean metallicity, which is caused by the slower evolution with time, giving each SNR longer to evolve before the required metallicity is reached.

In essence, we see a direct connection between the rate of metal-enriching events (which follows the SFR) and the degree of spread in the abundance of the ISM at a given global average metallicity. As the SFR increases, so does the extent of metal disparity across the simulation. This is because newly formed gas is injected at a faster rate than the rate at which turbulent mixing smooths them down.

The nearly uniform density along the disk plane compels the remnants to remain nearly circular, while the density gradient

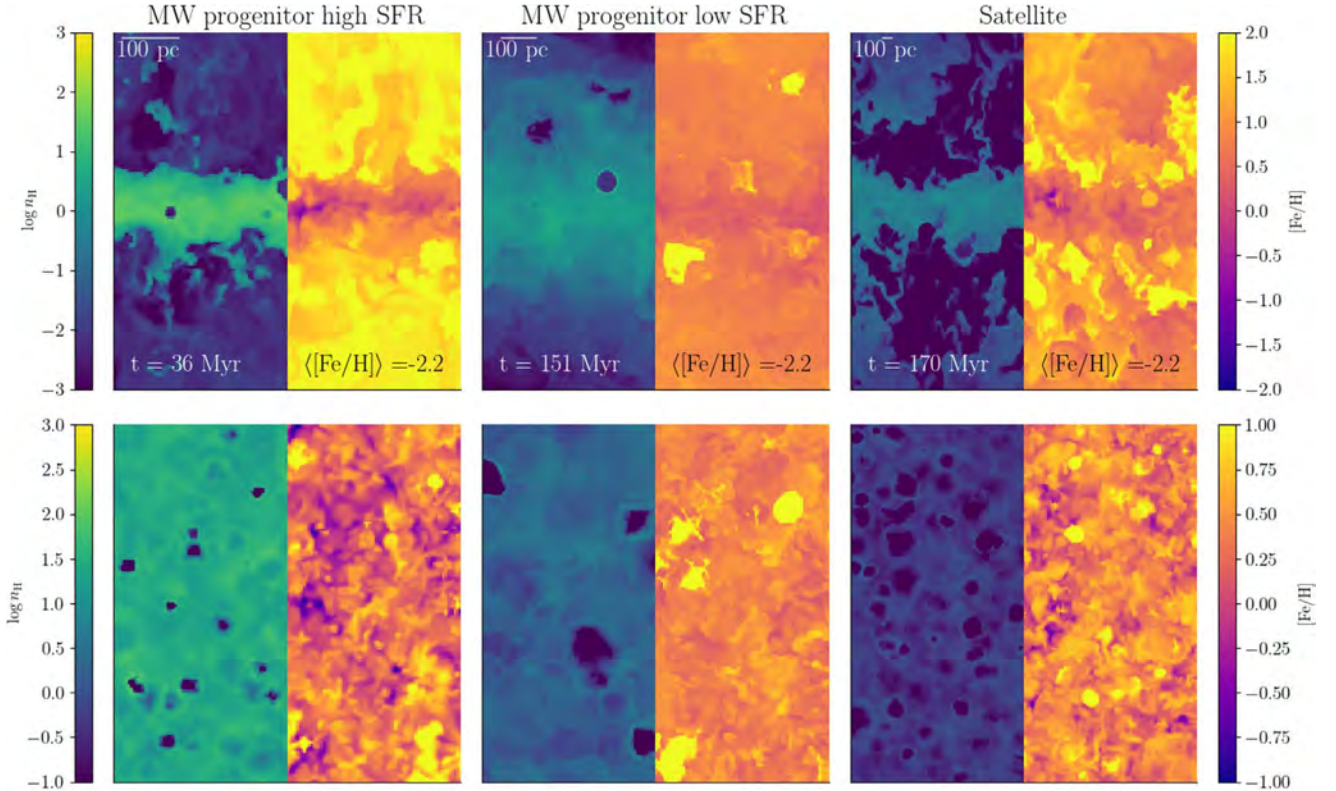


Figure 2. Slice maps through the center of the computational domain for different galaxy models, indicated by the panel titles. All snapshots are taken when $\langle [Fe/H] \rangle = -2.2$. The number of SNe, N_{SNe} , required to reach this mean abundance is 5600, 1300, and 14,000, respectively. The top row shows an edge-on view, while the bottom row shows a face-on view of the disk. In each panel, the left-hand side (blue–green color map) is the number density of H ($\log_{10} n_H$) while the right-hand side (purple–yellow) is the local gas abundance of $[Fe/H]$. Each panel is $6z_{eff}$ along each axis, while the scale bars indicate the relative sizes between panels. The time since the beginning of the simulation is shown. These times correspond to $1.89t_*$, $3.87t_*$, and $1.41t_*$, respectively. In all models, individual SNR are clearly resolved, and the increased homogeneity of the lower SFR models at the same $\langle [Fe/H] \rangle$ can be easily observed.

perpendicular to the disk causes them to expand more easily along the steep vertical pressure gradient. This allows metal-enriched outflows to reach the edge of the disk and be ultimately expelled (Martizzi et al. 2015). A review of the time series of these metal maps shows enriched gas getting expelled from the disk, rising within the gravitational potential before cooling and falling back, which is reminiscent of a mini galactic fountain. We note here that some gas is able to leave the simulation domain, and the outflow boundary conditions at the top and bottom of the computational box do not allow it to return. As a result, enriched material is steadily lost from the galactic disk patch. As discussed in Section 3.1 this is a small effect for the MW progenitor models but a considerable one for the dwarf galaxy model, which cannot be considered dynamically stable over longer periods of time and is unable to effectively retain the metals injected by SNe. In Section 3.1 and Appendix B we show that the MW progenitor model with low SFR and high ϵ_* exhibits the same behavior, although to a lesser degree than the dwarf-satellite model.

Having discussed the evolution and the salient features of the small patch disk simulations, we now turn our attention to quantifying the degree of metal mixing and its relevance to spectroscopic observations of stars in the MW.

4. Metal Mixing and Comparison to Observations of Metal-poor Stars

In this section we examine the mixing of metals by SNe in the surrounding gas. In Section 4.1, we consider the local

mixing around the sites where SNe, assumed to be chemically identical, recently occurred. In Section 4.2, we study the spread in $[Mg/Fe]$ abundances achieved in each of our models with SN metal injections with intrinsic variations in the yields. In this case, we compare the results of the simulations with the $[Mg/Fe]$ spreads inferred from metal-poor halo stars in the MW with the goal to constrain the SFR in the birth environments of these stars.

4.1. Understanding Local Mixing

In this section we leverage the high spatial and temporal resolution of the patch disk simulations to study the metal mixing properties of individual SNe. In each simulation, we record the time and position of all SNe, thus enabling us to study their evolution and the associated metal dispersion across the galaxy disk.

4.1.1. Metal Mixing at the Cooling Scale

The origin of the dispersion of Fe (Mg) masses around injection sites depends sensitively on the degree of overlap between the metals injected from neighboring SNR. Intuitively, a population of chemically identical SN is well mixed at a particular length scale when the dispersion of Fe (Mg) masses measured across the disk at this particular scale is modest. Here, we select the cooling radius around all of the injection sites as our characteristic scale. In order to integrate the metals into new stars, the swept-up mass must first cool (Nomoto et al. 2013; Macias & Ramirez-Ruiz 2018); therefore, the cooling

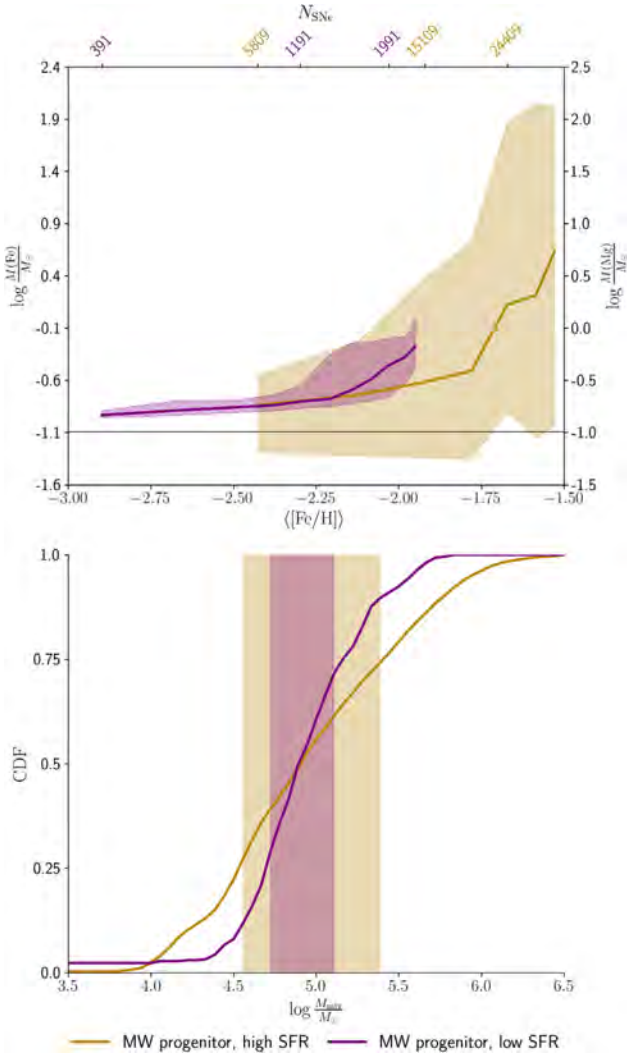


Figure 3. Top panel: Median (solid lines), 25th, and 75th percentile (shaded region) of the mass of Fe (Mg) enclosed within R_{cool} around all SN injection sites (average over 15 Myr intervals) in the MW progenitor with low SFR (purple) and the one with high SFR (yellow). The solid black line marks the mass of Fe per injected SN and thus provides a measurement of the degree of overlap between adjacent mass injection events. Both models are marginally consistent with a single enrichment model at low $\langle[Fe/H]\rangle$. Bottom panel: cumulative distribution functions (CDF) of the mixing masses derived for all injected SNe in the two MW progenitor models (colors are the same as in the top panel). The shaded region denotes the IQR for both distributions. The patchy distribution of elements in the higher SFR model translates to a wider distribution of mixing masses for the SNe.

mass yields a robust lower limit on the minimum amount of enriched gas that can be incorporated into the next generation of stars. The metal content within a cooling mass thus provides a simple test of the single enrichment star formation assumption (e.g., Karlsson et al. 2013). It is useful to recall that the cooling radius (and hence the cooling mass) depends sensitively on the mean density of the surrounding gas (Equation (1)) but only weakly on its mean metallicity (Karpov et al. 2020).

The upper panel of Figure 3 shows the enclosed Fe (Mg) mass within the cooling scales of the SNe in both MW progenitor models. Both models display an initial quasi-linear trend in the Fe (Mg) mass with metallicity, followed by a change in slope at $\langle[Fe/H]\rangle \approx -2$. The early behavior follows

the expected evolution for overlapping SNR expanding in a medium in which the enrichment of the surrounding material is dominated by recently injected metals and not by the mass of the metals residing in the ISM. At $\langle[Fe/H]\rangle \approx -2$, the mass of Fe (Mg) contained within the swept-up ISM begins to be a meaningful contribution to the total Fe (Mg) mass within a cooling radius.

In this formalism, the number of overlapping SNe within a cooling mass can be easily inferred by comparing the total enclosed mass of any element with that expected from a single SNR, which is illustrated (for Fe) by the solid black line (upper panel of Figure 3).

As expected, the dispersion of (Mg) within a cooling mass is smaller for the low-SFR model. When examining the morphology of the individual SNR in Figure 2 it is clear that this happens because neighboring remnants in this model show significant overlap. This effect is compounded by the larger cooling radii of the remnants, caused by the lower mean density of the surrounding ISM. In contrast, the high-SFR model, despite having a larger number of injected SNe at the same $\langle[Fe/H]\rangle$, shows a larger dispersion in the number of SNR that overlap at the chosen scale. Across the disk, we see regions with no overlapping remnants, while other regions show significant overlap between neighboring remnants. This emanates by virtue of the fact that individual remnants in this model remain compact enough to be restricted to scales smaller than the disk scale height. As such, individual remnants sample a wide range of density scales and thus a corresponding wide range of cooling masses.

Macías & Ramirez-Ruiz (2018) argued that the abundances of $[Mg/H]$ of stars with $[Fe/H] \lesssim -2$ could be consistent with enrichment from SN sites yielding $M_{Mg} = 0.1 M_{\odot}$. Our results suggest, that while it is unlikely (at the SFRs considered here) to form stars from gas that has been enriched by a single event, stars with enrichment by a few events are plausible at $\langle[Fe/H]\rangle \lesssim -2$. This is in broad agreement with the results of Welsh et al. (2021) who modeled the stochastic enrichment of metal-poor stars by the first SNe and found the expected number of enriching first SNe to the most metal-poor stars to be $N_{SNe} = 5_{-3}^{+13}$.

Our simulations suggest that the ISM in the galactic disk patches increased rapidly in metallicity after less than 100 Myr. With the assumption that Population III stars can only form in gas with metallicity below a critical value, it is thus worth quantifying the pristine gas fraction below a threshold metallicity. Following Pan et al. (2013), we calculate the fraction of gas with $[Fe/H] < -6$ at the onset of steady state in each of our models and find $\lesssim 0.5\%$ (high-SFR MW progenitor at $t_r \approx 20$ Myr), $\lesssim 1.5\%$ (low-SFR MW progenitor at $t_r \approx 40$ Myr) and 0% (dwarf-like satellite at $t_r \approx 120$ Myr). The ubiquity of heavy elements in the Ly α forest indicates that there has been widespread diffusion from the sites of these early SNe, which is consistent with our findings. Mackey et al. (2003) estimated that most of the star-forming material in the intergalactic medium (IGM) has reached $[Fe/H] < -3.5$ in the range $z \approx 15$ –20. Constraining how these Population III stars form at high- z is thus of great relevance.

4.1.2. Characteristic Mixing Masses

Enrichment of the ISM depends on how efficiently metals are mixed with the ambient material swept up by the individual blast waves. At the time of shell formation (i.e., cooling radius), we find the mass fraction of Fe (Mg) to be enhanced in

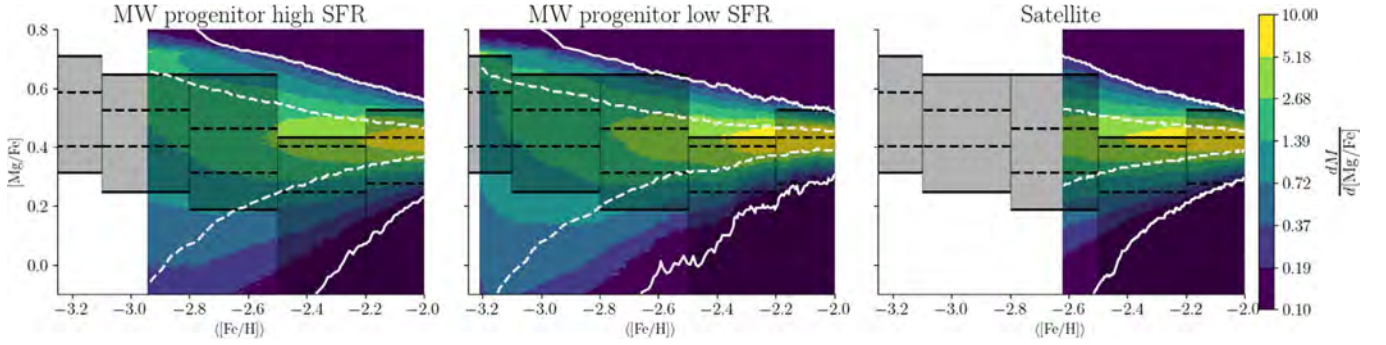


Figure 4. Mass-weighted distributions of $[Mg/Fe]$ in the cold, dense gas as a function of $\langle[Fe/H]\rangle$ for SN injection sites with intrinsic yield variations. The solid white contours indicate the 99% extent of the distributions while the dashed lines indicate the 68% extent. The black shaded regions indicate the $[Fe/H]$ bins used to bin the abundances measured by Roederer et al. (2014), the solid black lines indicate the 99% span of the sample in the bin, and the black dashed lines indicate the 68% span. From left to right, the surface density of gas in the modeled galaxy decreases.

relation to the surrounding medium for most injected remnants, although that fraction decreases as the simulation evolves. These localized Fe (Mg) enhancements are then smoothed out as the enriched gas is given more time to expand and mix throughout the disk.

Motivated by this, we calculate the scale at which the enclosed $[Fe/H]$ ($[Mg/H]$) around each SN site is less than or equal to the mean abundance, $\langle[Fe/H]\rangle$ ($\langle[Mg/H]\rangle$), of the disk. We refer to this integrated mass as the mixing mass, which broadly represents the characteristic scale at which SNRs become chemically indistinguishable from the background gas. The bottom panel of Figure 3 shows the cumulative distributions of the mixing masses in each of the two MW progenitor models. A modest fraction of all SNR reach their mixing masses within the scale height of the disk; only those that do are shown. The fraction of the remnants that are confined within $\lesssim 2z_{\text{eff}}$ of the disk is 25% for the MW progenitor model with high SFR and 20% for the model with low SFR.

The MW progenitor with low SFR shows a narrower range of mixing masses, which is indicative of a more homogeneous distribution of metals within the disk. By contrast, the high-SFR model exhibits a more patchy distribution of elements at the same $\langle[Fe/H]\rangle$, leading to a larger spread in mixing masses. The smallest mixing masses within the distribution can be understood as the masses of those SNe that happened to go off in more pristine environments at a time when the disk has already achieved a large mean metallicity, so less dilution is required to reach the background value. Conversely, the highest mixing masses are caused by SNe that occur in regions where the local abundance is higher than the disk average background abundance and are thus harder to dilute.

It is noteworthy that the range of mixing masses we derive from these models are similar to the range obtained by Macias & Ramirez-Ruiz (2018) for metal-poor stars in the same $[Fe/H]$ range, which were calculated under the assumption of mixing with a perfectly pristine background. This assumes that the cold gas that turns into new stars preserves the metal variations in the gas at a given $\langle[Fe/H]\rangle$. Having made the case that the spread of stellar abundances at a given $\langle[Fe/H]\rangle$ can be associated with the star formation properties of the progenitor disk and their end products, it is worth thinking further about the implications.

4.2. Star-forming Gas and Comparison to Observations

Motivated by the results presented in the previous section, we examine the spread of $[Mg/Fe]$ as a function of $\langle[Fe/H]\rangle$ predicted by our models, under the assumption of intrinsic yield variations. This allows us to directly compare our models to observations, given that we have two independent tracers of metal mixing. One being the spread in $[Mg/Fe]$, which is set at the onset by the assumed SN-to-SN yield variance and is then subsequently smoothed out by turbulent diffusion, and the other one being the average $\langle[Fe/H]\rangle$, whose evolution is driven by metal injection and turbulent diffusion.

Our framework does not self-consistently incorporate star formation so, in order to make a meaningful comparison, we consider the cold gas within the disk that is the most likely to form stars. We impose a temperature threshold of $T \leq 10^4$ K, associated with the cooling function temperature floor, and a density threshold of $\rho \gtrsim (\rho_0/4)$. At each simulation output we calculate the mass-weighted distributions of $[Fe/H]$ and $[Mg/Fe]$ in the gas that fulfills both of these requirements.⁹

In Figure 4, we show the distributions of $[Mg/Fe]$ as a function of $\langle[Fe/H]\rangle$. The color map indicates the gas mass (M_{\odot}) in each bin of $[Mg/Fe]$ abundance. The differences in $\langle[Fe/H]\rangle$ range covered in each panel are due to the different speeds at which the patches are enriched by SNe in combination with the different timescales over which the models come to steady state. All models are initialized at the same $\langle[Fe/H]\rangle$ but as some models relax more quickly the first distribution included may be at a lower metallicity compared to a model that relaxes more slowly (see Section 3.1). The solid white contours indicate the 99% extent of the $[Mg/Fe]$ distributions, while the dashed white lines denote the 68% extent. The metal-poor halo stars used for this comparison are taken from Roederer et al. (2014), and the specific sample selection criteria are discussed in Appendix A. We opt to compare our simulations with this sample because of its relatively large size (≈ 300 metal-poor halo stars) and the care taken by the authors to document the uncertainty of their measurements. This allows us to use the star-to-star $[Mg/Fe]$ scatter as a function of $[Fe/H]$ derived by the authors as a

⁹ We note that this leads to a slightly different mean abundance than what is considered in the previous sections where all the gas, not only the cold component, is used for the calculation.

constraint for the intrinsic $[\text{Mg}/\text{Fe}]$ elemental variations driven by turbulent diffusion.

Some obvious points should be emphasized. The degree of metal mixing of the cold gas within the disk is, as we argue in the preceding sections, directly impressed on the extent of the $[\text{Mg}/\text{Fe}]$ spread. This spread arises naturally from the intrinsic distribution of Mg and Fe yields in SNe (e.g., Kobayashi et al. 2006) and is clearly seen in the abundance determinations of metal-poor stars. In the simulations, this metal spread is initially set by the selected yield variance and is then gradually smoothed down by turbulent diffusion. We note that the exact shape of the simulated distribution of $[\text{Mg}/\text{Fe}]$ depends sensitively on the assumed SNe yields, while the shape of the outer envelope is primarily determined by turbulent diffusion, whose coefficient is sensitive to the properties of the galaxy (Table 1). As a result, the evolution of the spread of $[\text{Mg}/\text{Fe}]$ with $\langle[\text{Fe}/\text{H}]\rangle$ is an observable diagnostic of the star formation processes occurring within the disk.

In almost a literal sense, the stage is set for us to interpret the observational properties concerning metal-poor stars in the context of turbulent mixing driven by SN feedback. Figure 4 shows that the simulations provide us with information about how the derived $[\text{Mg}/\text{Fe}]$ spreads in the simulations evolve with $\langle[\text{Fe}/\text{H}]\rangle$, which depends on the star-forming properties of the system. As such, we might be able to constrain the SFR of the birth environments of metal-poor stars when the derived $[\text{Mg}/\text{Fe}]$ spreads in the simulations are unable to effectively describe the observed distributions.

There are, however, three effects that render the task of interpreting the simulations in the context of observations challenging. The first stems from the assumed SNe yield distributions, which are not well constrained and are likely sensitive to the IMF and the explosive properties of the progenitors (e.g., Arnone et al. 2005). A second challenge is that the assembly process that led to the metal-poor stars we observe today likely involves multiple populations (e.g., Bullock et al. 2001; Robertson et al. 2005; Johnston et al. 2008; Deason et al. 2016). Third, our understanding of the Milky Way’s stellar halo based on the analysis of local stellar samples is yet incomplete due to the limited sampling generated by the survey footprints. In particular, the observational sample used in this analysis suffers from incompleteness and selection effects, which are most prominent at lower $[\text{Mg}/\text{Fe}]$ abundances (Roederer et al. 2014; see also Appendix A of this work). More promising for the immediate future is to compare the high abundance tail of the $[\text{Mg}/\text{Fe}]$ distributions in the simulations with observations, with the goal to constrain the SFR of the birth environments of metal-poor stars.

In order to make a qualitative comparison between all the simulated models and the observations, we first make a cut in all data sets where they overlap in $\langle[\text{Fe}/\text{H}]\rangle$, which leaves us with simulated gas with $-2.6 < \langle[\text{Fe}/\text{H}]\rangle \leq -2.0$ (for the observations this range applies to the observed metallicity). Within this metallicity range, we identify the $[\text{Mg}/\text{Fe}]$ abundance value below which 95% of the stars are contained, which gives $[\text{Mg}/\text{Fe}] \simeq 0.45$. We then calculate for each simulation the fractional mass of cold, dense gas that has an abundance higher than this threshold: MW progenitor high SFR 21%, MW progenitor low SFR 13%, and Satellite 15%. This begins to pose a problem for the high-SFR model. Furthermore, if the SNe yields are adjusted to be compatible with the stars at lowest metallicity (where models are not yet in

steady state, but the stars show a larger dispersion in $[\text{Mg}/\text{Fe}]$), the high-SFR model is even less capable of explaining the observations. This is because, the rate of smoothing down of the yield variance depends sensitively on the turbulent diffusion coefficient, which is significantly lower for the high-SFR model (see Section 5). Obviously, the above comparison is only sketchy and should be taken as an order of magnitude estimate at present given the challenges discussed above.

It is evident from Figure 4 that the SFR leaves an imprint on the metal spread, whose amplitude at a given mean metallicity is primarily influenced by SN-driven turbulence, whose coefficient determines the speed at which the initial $[\text{Mg}/\text{Fe}]$ spread is smoothed out as the $\langle[\text{Fe}/\text{H}]\rangle$ increases in the simulations (Table 1). From the simple analysis presented above, we find evidence that the properties of the metal-poor halo stars are consistent with stellar birth sites in a MW progenitor with a low SFR or a satellite galaxy.

Our findings provide ancillary evidence that the dispersion of $[\text{Mg}/\text{Fe}]$ observed in metal-poor stars are consistent with either these stars being deposited into the stellar halo of the MW by mergers of low-mass dwarf galaxies (e.g., Bullock et al. 2001; Robertson et al. 2005; Johnston et al. 2008) or potentially in situ formation if the MW had a modest SFR, as has been recently suggested by Wang et al. (2021).

5. Discussion

Motions in a turbulent flow endure over a broad range of length and timescales. The characteristic length scales correspond to the fluctuating eddy motions that exist, with the largest scales bounded by the geometric dimensions of the flow. The diffusion coefficient associated with turbulence can be estimated as (Karlsson et al. 2013; Krumholz & Ting 2018)

$$\kappa \approx \frac{z_{\text{eff}} \langle \sigma_v \rangle}{3}, \quad (3)$$

where z_{eff} is the outer scale of the turbulence (scale height of the disk), and $\langle \sigma_v \rangle$ is the gas turbulent velocity dispersion on this scale. Table 1 gives the diffusion coefficient for all the models presented in this work. Higher diffusion coefficients indicate faster rates of mixing. For comparison, in the solar neighborhood $\kappa \approx 300 \text{ pc km s}^{-1}$ (Krumholz & Ting 2018). We note that the diffusion coefficient derived here for dwarf galaxy environments, which is larger than the ones derived for MW progenitors, is concordant with the subgrid diffusion models that are needed in cosmological simulations in order to explain the observed stellar $[\text{Fe}/\text{H}]$ abundance distributions in dwarf galaxies in the Local Group (Escala et al. 2018).

An important quality of metal mixing is the connection that exists between the variance of the spatial metal concentration to the diffusion coefficient. Krumholz & Ting (2018) used a stochastically forced diffusion framework to model the spatial metal fluctuations in galaxies and derive a simple estimate for a characteristic mixing length scale

$$x_m \approx \left(\frac{\kappa}{\Gamma} \right)^{1/4}, \quad (4)$$

where Γ is the rate of SN events per unit area. Using the values for κ and Γ listed in Table 1 along with Equation (4), we derive $x_m = 26 \text{ pc}$ and 67 pc for the high-SFR and the low-SFR models, respectively. This simple estimate is in close agreement with the

characteristic mixing mass scales calculated in Section 4.1.2 for the high-SFR and the low-SFR models at the fixed $\langle[\text{Fe}/\text{H}]\rangle \approx -2.3$: $x_{\text{mix}} = 31$ pc and $x_{\text{mix}} = 78$ pc, respectively. As we argue in Section 4, the SFR plays an important role in determining the scale of the metal abundance fluctuations and can be inferred by studying the metallicity dispersion in stars.¹⁰

The mixing mass scale measures a characteristic enlargement of the effective size of a remnant. At this scale, the metallicity fluctuations start to be smoothed out. An akin pressure length scale (Draine 2011) can be estimated by calculating the characteristic radius at which the SN blast wave expansion velocity becomes comparable to $\langle\sigma_v\rangle$:

$$x_P \approx 67 \rho_{0,-24}^{-0.37} \left(\frac{E_{\text{SN}}}{10^{51} \text{ erg}} \right)^{0.32} \left(\frac{\langle\sigma_v\rangle}{10 \text{ km s}^{-1}} \right)^{-0.4} \text{ pc}, \quad (5)$$

where $\rho_{0,-24} = \frac{\rho_0}{10^{-24} \text{ g cm}^{-3}}$. Taking ρ_0 as the midplane density in the galactic disk yields $x_P = 20$ pc and $x_P = 59$ pc for the high-SFR and the low-SFR models, respectively. We caution the reader that these length scales do not take into account galactic winds (e.g., Christensen et al. 2018) and that x_P and x_{mix} are comparable to the scale height of the disk. In Section 4.1.2, we show that a sizable number of remnants are advected by the galactic wind before they are able to effectively mix with the ISM. This implies that the winds simply remove portions of the gas that are not widely distributed and are highly correlated with the metal field. Therefore, the effect of metal removal on the dispersion of the metal field is limited. Similarly, we expect galactic shear (Yang & Krumholz 2012; Petit et al. 2015) only to be prominent on relatively longer timescales when compared with the timescale for mixing of gas by turbulent feedback from SNe (e.g., Pan & Scannapieco 2010; Pan et al. 2013).

Observations of $[\text{Mg}/\text{Fe}]$ dispersion in metal-poor stars suggest variations in the metal yields of SNe. Such intrinsic variations are preserved when the ISM is not well mixed on average at these early times. They are subsequently smoothed out by turbulent diffusion. As we have argued here, the degree of smoothing is sensitive to the SFR. The observed dispersion values in stellar abundances of stars in the Milky Way can be explained when considering the early spotty pollution of new elements from nonchemically homogeneous SNe (Audouze & Silk 1995). For a hierarchically structured ISM with SF operating on a local dynamical timescale, the size of OB stellar associations is typically comparable to the metal mixing scale (e.g., Elmegreen 1998), and the new elements should continue to be patchy and variable for stars formed in different clusters. That is, such gas variations are expected to be preserved by the SF process.

The statistics of variations of stars in chemical space can provide valuable constraints on the star-forming conditions. According to our study, the observed abundance spread of $[\text{Mg}/\text{Fe}]$ in metal-poor halo stars (Roederer et al. 2014) is consistent with the SF properties of dwarf satellites or an early low-SFR MW like the one described by Wang et al. (2021). Our findings are broadly consistent with the idea that the metal-

poor stellar content of the MW halo could in principle be explained entirely by disrupted dwarf satellites (e.g., Bullock et al. 2001; Robertson et al. 2005; Johnston et al. 2008; Frebel 2010; Roederer et al. 2018), which has recently gained stellar kinematic support (Santistevan et al. 2021).

Metal variations in halo stars thus represent an opportunity for chemical tagging studies to further elucidate their formation origins. To better understand the stellar halo and its assembly, it is crucial to select halo stars without introducing any biases, while reducing the contamination introduced by combining multiple stellar populations. In principle, large spectroscopic surveys of MW stars such as Gaia-ESO (Gilmore et al. 2012) offer a unique opportunity for reconstructing the SFH of the MW by measuring the metal abundance spreads in the Galactic field and, in particular, among stars residing in individual stellar streams.

Disentangling the SFHs of the many satellites that contributed to stars in phase-mixed galactic fields is challenging, as illustrated in Section 4.2. More optimistically, we hope that for stars residing in individual streams, metal variations may be key to understand the SFH of the progenitor galaxy. For surviving galaxies, it might be possible to deduce if there are clear differences between the formation history of stars belonging to the surviving self-bound satellite and the debris stars of the disrupted accretion event.

Our understanding of the assembly of the MW has come a long way. Nevertheless, it continues to offer major puzzles and challenges. Metal variations thus provide us with an exciting opportunity to derive, in combination with kinematic studies and stellar tagging, the contribution of satellites to the accreted stellar halo mass, as well as inferring the specific SFHs of individual galaxies.

We thank the referee for insightful questions that have helped to substantially improve the quality of the paper. We thank S. Faber, E. Kirby, A. Ji, K. Brauer, P. Macias, J. Primack and D. Zaritsky, for useful discussions. A.N.K. and E. R.-R. acknowledge support by Heising-Simons Foundation, the Danish National Research Foundation (DNRF132) and NSF (AST-1911206 and AST-1852393). This work made use of an HPC facility funded by a grant from VILLUM FONDEN (project number 16599). H.P. acknowledges support from the Danish National Research Foundation (DNRF132) and the Hong Kong government (GRF grant HKU27305119, HKU17304821). M.S.F. gratefully acknowledges support provided by NASA through Hubble Fellowship grant HST-HF2-51493.001-A awarded by the Space Telescope Science Institute, which is operated by the Association of Universities for Research in Astronomy, Inc., for NASA, under the contract NAS 5-26555.

Appendix A Observed Abundances and SN Yields

We compare our simulated results with the observations of the 313 metal-poor, $-4.5 \leq [\text{Fe}/\text{H}] \leq -1.1$, MW halo stars deduced by Roederer et al. (2014). After removing stars with upper limit measurements for either $[\text{Fe}/\text{H}]$ or $[\text{Mg}/\text{H}]$, as well as, carbon enhanced metal-poor (CEMP) stars, defined as stars with $[\text{C}/\text{Fe}] > 0.7$ (Aoki et al. 2007), we are left with 224 stars in the sample. CEMP stars exhibit anomalous abundances of C relative to Fe, several theories exist to explain this over-abundance, one likely model is that these stars have experienced mass transfer in a binary with an asymptotic giant

¹⁰ We note here that the typical abundance scatter predicted by Krumholz & Ting (2018) is smaller than the one deduced from our simulations and observed in metal-poor stars. This is to be expected, as their model is manufactured to predict abundance dispersions for the MW at solar metallicity.

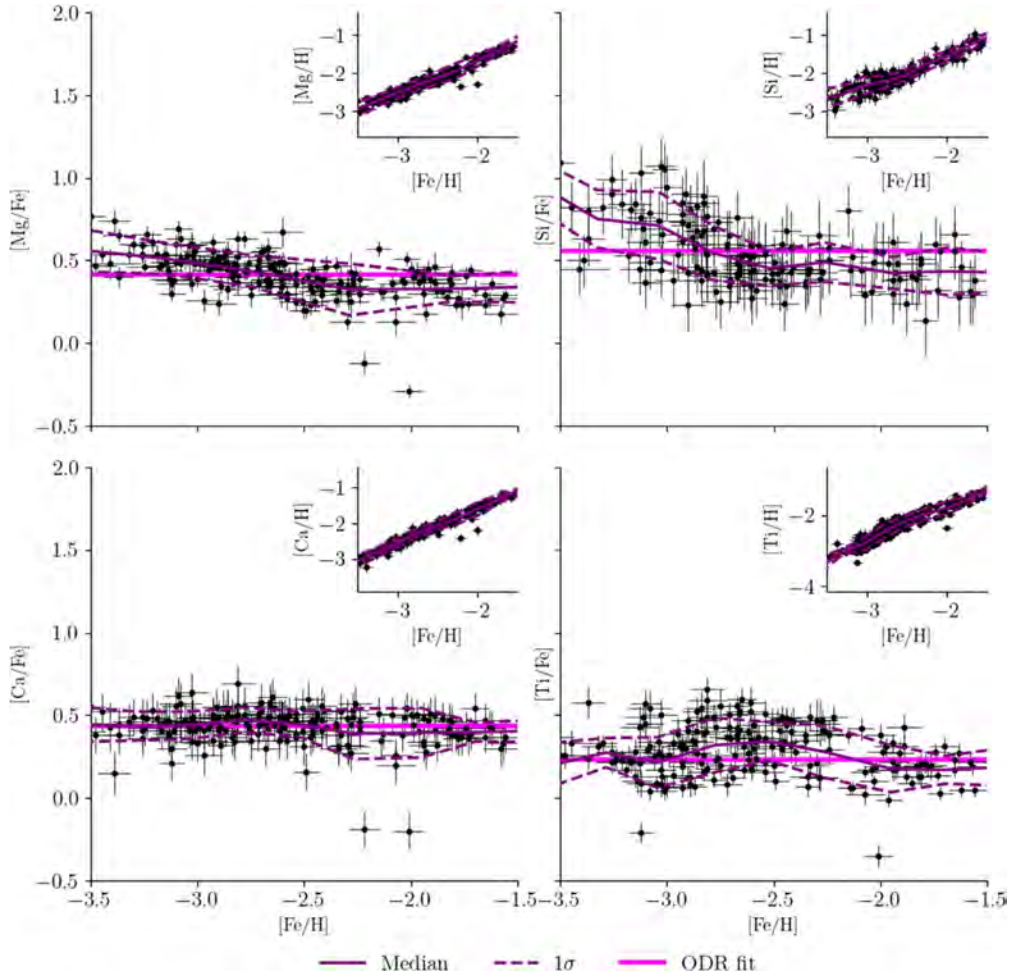


Figure A1. Abundances of selected α -elements of the metal-poor halo stars from Roederer et al. (2014), which we use as our comparison sample. From top left, to bottom right, the panels show the measured abundances of: Mg, Si, Ca, and Ti relative to Fe as function of [Fe/H]. Error bars indicate the total uncertainty as reported by Roederer et al. (2014). The solid, dark purple lines indicate the mean in 0.5 dex wide bins in [Fe/H], and the dashed lines are the 1σ spread in the same bins. The insets in each panel show the abundances of the same elements relative to H. The solid fuchsia lines indicate the best orthogonal distance regression (ODR) fit to the abundances.

branch star (Beers & Christlieb 2005). If this is the case their measured abundances will not be representative of the gas from which they formed, and we thus remove them from this sample.

In Figure A1 we show the measured abundances of the 224 stars we use from Roederer et al. (2014), in four α elements: Mg, Si, Ca, and Ti. We use the total uncertainty from their Table 12 and the method they outline to calculate uncertainties for other ratios to get $\sigma_{[X/H]}$. Also plotted are the mean and 1σ spreads calculated in 0.5 dex wide bins in [Fe/H]. We note that Ti, while not an α -element, is the result of incomplete burning and is highly correlated with α -element production. Baring the much larger uncertainties in Si measurements, the overall behavior in these element abundances are very similar to the behaviors of Mg in that they all show tight correlations with [Fe/H] with nearly constant scatter around the mean of the range of metallicity considered here. This underscores that Mg is indeed an appropriate representative of the α -elements. This is to give further credence to the idea that yield variations are indeed required by the observations.

As a point of comparison we show in Figure A2 the abundances reported to Jinabase (Abomalima & Frebel 2018) for MW halo stars marked as non-CEMP, fulfilling $-3.5 \leq [\text{Fe}/\text{H}] \leq -1.0$. When abundances are reported several times for the same star,

only one data point is shown for that star; this selection was made at random. This selection results in a total of 1056 stars included. For a subset of the stars with multiple measurements we calculate the intrinsic star-to-star scatter between reported abundances from different groups, which is indicated by the colored error bars on the panel. This intrinsic scatter is indicative of the systematic errors between different analyses. The existence and size of this scatter is the reason we decided to compare our results with observations from a single study to ensure that, to the largest degree possible, the spreads reported were intrinsic rather than being dominated by systematic uncertainties between different measurements.

A.1. SN Yields

To determine the yield ratio of the chemically identical SNe we calculate the mass ratios of Mg to H and Fe to H of the (Roederer et al. 2014) sample and fit a linear relationship. The result of this is plotted in Figure A3. The best fit has a slope of $\frac{M_{\text{Mg}}}{M_{\text{H}}} = 1.27 \frac{M_{\text{Fe}}}{M_{\text{H}}}$, fixing the mass of Mg per event to $0.10M_{\odot}$ and requiring all SNe to obey this relationship, the mass of Fe per event needs to be $M_{\text{Fe}} = 0.08M_{\odot}$.

As described in Section 2.1 we disentangle the Mg field from the Fe by allowing SNe not to be chemically identical, as

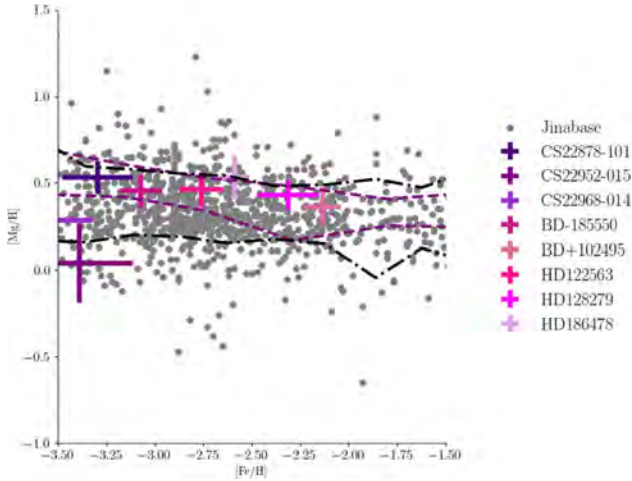


Figure A2. $[\text{Mg}/\text{Fe}]$ vs. $[\text{Fe}/\text{H}]$ abundance measurements of non-CEMP stars in the MW halo from Jinabase (Abohalima & Frebel 2018). The colored crosses show the intrinsic dispersion of measurements for a selection of stars. Black dashed-dotted lines indicate the 1σ spread of these stars in the same $[\text{Fe}/\text{H}]$ bins as used in Figure A1. The purple dashed lines are the same as in the $[\text{Mg}/\text{Fe}]$ panel in Figure A1 and have been added to aid comparison.

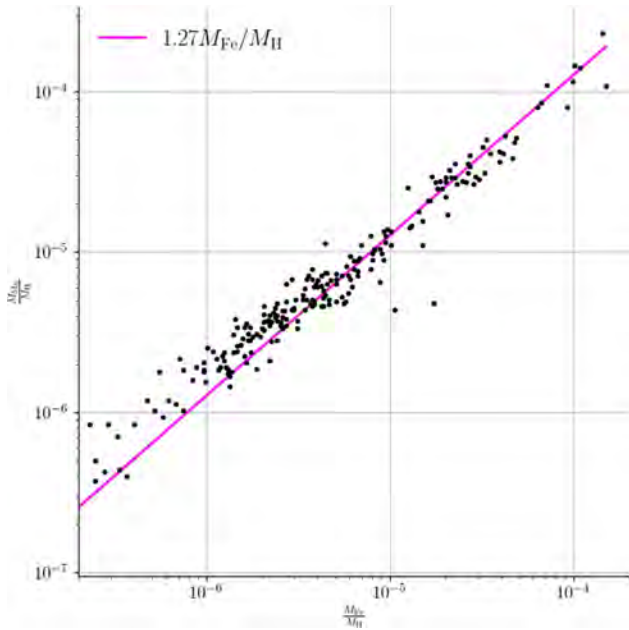


Figure A3. Mass ratio of Mg to H as a function of the same for Fe to H for the 224 stars from (Roederer et al. 2014). The solid line is the best linear fit to the data and is used to determine the mass of Fe per SNe for the chemically identical SNe models used in this project.

required by observations. We achieve this by introducing two specific $[\text{Mg}/\text{Fe}]$ yields for SN injection sites. These yield values are chosen again to match the mean we expect based on the observational data set of $[\text{Mg}/\text{Fe}] = 0.42$. We set the high-yield SN injection site to have a yield $[\text{Mg}/\text{Fe}] = 0.72$. This value is chosen based on the most highly enriched star in the data set. The low-yield SN injection site is then set to achieve the desired mean, which results in a value of $[\text{Mg}/\text{Fe}] = -1.39$.

The values of these yields as well as the range of abundances in the observational data set are visualized in Figure A4. This figure also shows the theoretically predicted yields of SN as a function of the progenitor mass and metallicity as reported by

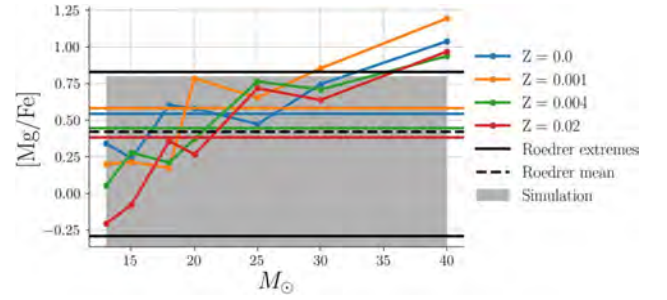


Figure A4. Yield abundances of SNe as a function of the progenitor mass and metallicity according to Kobayashi et al. (2006). The horizontal lines show the IMF-weighted average yields at the same metallicities. Also shown is the mean abundance of the (Roederer et al. 2014) sample (solid black line) as well as the abundance of the most and least enriched stars in that sample (black dashed lines). The gray box indicates the yields used in this work $[\text{Mg}/\text{Fe}] = 0.72$ and $[\text{Mg}/\text{Fe}] = -1.39$ (lower yield not visible in this panel).

Kobayashi et al. (2006). In addition, the IMF-weighted average of these yields is also shown. It is important to note that the predicted yields of SNe by Kobayashi et al. (2006), albeit uncertain, are consistent with the empirically derived constraints. Although the yields predicted for the highest mass stars are in contention with the observational constraints the IMF-weighted average yields agree well with the data. It is important to note that the observations of metal-poor stars, and in particular the empirically derived yield variations, can be effectively used to constrain the currently uncertain SN explosions models.

Appendix B

Exploring Changes in the Star Formation Efficiency

Here we investigate the effects of the SF efficiency, ϵ_* , in our simulations with chemically identical SNe. In particular, we explore the mixing properties of SNe occurring in three versions of the MW model with varying ϵ_* . We use the MW progenitor with low SFR as our base simulation. We then increase and decrease ϵ_* by a factor of 5, respectively. The parameters of these models are summarized in Table 1 in Section 2. In Figure B1 we compare the time evolution of σ_v for the three different simulations. The influence of ϵ_* on the velocity dispersion is clearly discernible. When ϵ_* is more or less extreme, there is a marked difference in the timescales for mixing of gas by the turbulence driven by SNe. ϵ_* influences

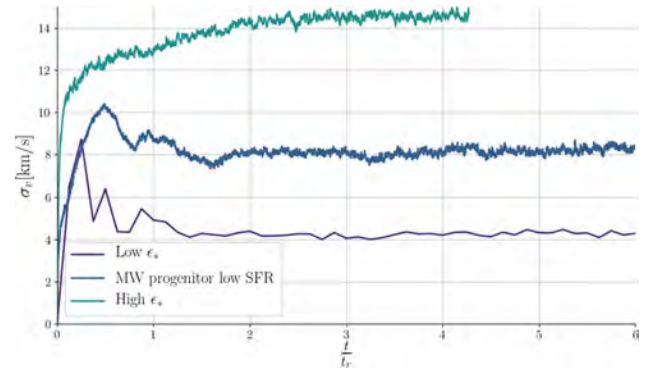


Figure B1. Comparison of the turbulent velocity dispersion, σ_v , in the three models using the same galaxy potential with varying rates of SNe per unit volume. Time is normalized by the relaxation time, t_r , in all cases. Both the base and low ϵ_* models reach a steady state, and the velocity dispersion stays relatively constant. The high ϵ_* case, however, does not reach dynamical stability, similarly to what was observed for the satellite model in Section 3.1.

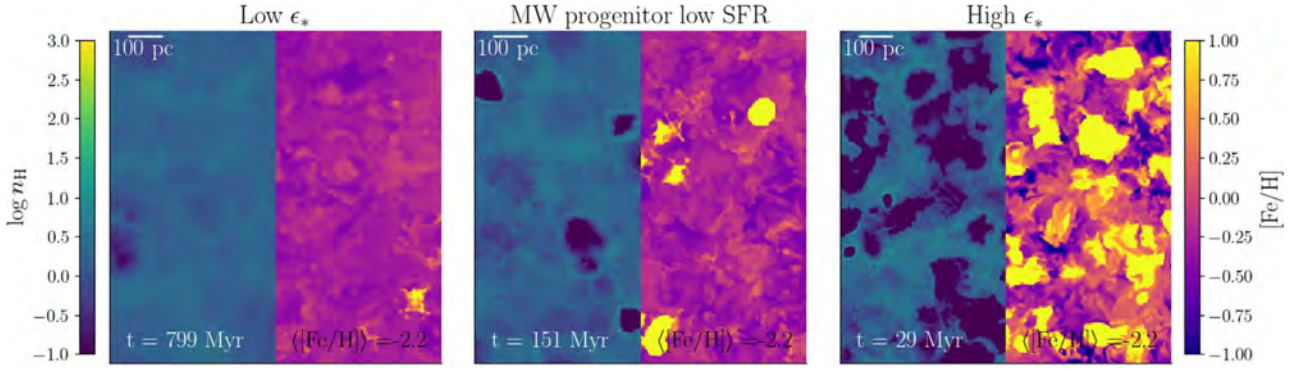


Figure B2. Same as the bottom row panels in Figure 2 but for the three MW progenitor models with varying ϵ_* . The slices are taken at the same mean metallicity as those in Figure 2. Because the total gas mass is the same in the three models the time to reach the same level of enrichment depends solely on ϵ_* . The effects of rapid enrichment for the high ϵ_* model are clearly evident in the right panel.

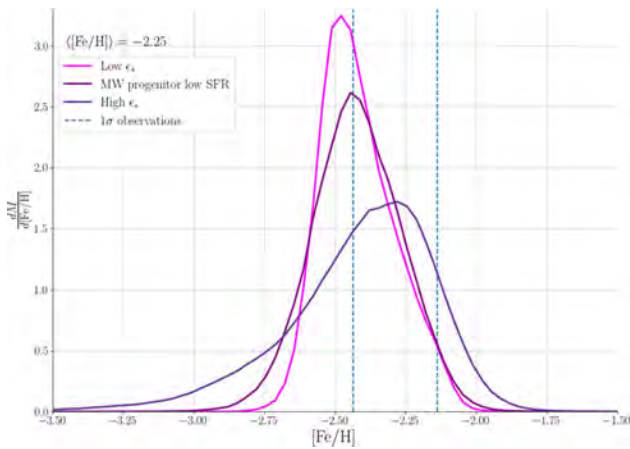


Figure B3. Comparison of the 1D distribution of $[Fe/H]$ in the three models at mean $[Fe/H] = -2.25$. Also shown are the 1σ spread of observations of $[Fe/H]$ at the same corresponding mean $[Fe/H]$ metallicity (dashed lines).

the extent to which turbulence mixes and homogenizes the gas in the face of repeated SN events. Altering ϵ_* by a factor of 5 leads to a difference of ≈ 2 in σ_v and t_r (Table 1).

The value of σ_v is set primarily by the intensity of the SN heating, which depends on the SN rate per unit volume, and the cooling rate of the shocked gas. The effect of cooling is negligible between models as they have similar gas density structures. When the energy input from SNe is equal to the binding energy of the cold gas, like in the model with highest ϵ_* and in the satellite model in Section 3.1, the disk becomes dynamically unstable and mass blow-out occurs. Over its lifetime the high ϵ_* model loses $\approx 10\%$ of its initial mass.

In Section 3.2 we discuss the complexity of element injection and transport and how our simulations capture the key qualitative feature that metallicity statistics result from a competition between stochastic injection of SNe, which produce metal inhomogeneity, and mixing by turbulence, which smooths out the abundance variations. Notably we show that simulations with higher SN rates per unit volume produce higher abundance dispersions at the same mean metallicity. This relationship is even clearer for simulations in which the galaxy potential and gas surface density are fixed. For example at $\langle [Fe/H] \rangle = -2.5$, the $[Fe/H]$ spread (measured as the 1σ of the distribution) is: 0.22, 0.27, and 0.55 for the low ϵ_* , base model and high ϵ_* , respectively. In Figure B2 we show a face-on view of the galaxy disk in the three models at the same

$\langle [Fe/H] \rangle$. As expected, the model with the highest ϵ_* has a much more patchy distribution of metals at the same mean abundance. This is because at the same mean abundance (i.e., a similar amount of SNe) the individual SNRs do not have as much time to spread and mix as they do when the rate is lower. This leads to a more patchy distribution of metals for the high ϵ_* model.

To study the abundance variations with ϵ_* we consider the distribution of $[Fe/H]$ in the cold, dense gas, which is selected in the same way as in Section 4. In Figure B3 we compare the 1D distributions of $[Fe/H]$ at $\langle [Fe/H] \rangle = -2.25$ in the three simulations. While the mean abundance of $[Fe/H]$ is similar in all three models, the shapes of the distributions are very different as well as their corresponding spreads. From Figure B3 we conclude that the high ϵ_* model is much less consistent with observations, thus reinforcing our conclusions about a preference for models with a modest SFR.

Appendix C Results with Intrinsic SN Yield Variations

Here we show the results of the three different models presented in Section 4.2. These models are similar to those presented in Section 3.2, although these models assumed no intrinsic SN yield variations. These chemically identical models are presented in Figure 2 and are used to study the mixing of Fe as a function of the global mean $[Fe/H]$ abundance. However, comparison with observations, as shown in Figure 4, are aided by having two independent tracers that can isolate the rate of SN injection and the effects of turbulent mixing. We do this in this *Letter* by introducing an intrinsic spread in yields from SN to SN, which is required by observations of metal-poor stars as described in Appendix A.

Figure C1 shows $[Mg/Fe]$ slice maps of the for each of the three galaxy models considered in this work. Individual SNRs with varying yields can be easily spotted. The influence of the metal injection rate, which is driven by the SFR, can be clearly seen when comparing the size of individual remnants between different models. Remnants are observed to reach larger physical sizes in the MW progenitor model with lower SFR than remnants in the MW progenitor model with high SFR. This produces a higher degree of smoothing in the spread of $[Mg/Fe]$ of the gas at given $\langle [Fe/H] \rangle$ in the lower-SFR models. One important feature of the comparison between our simulations and the observations in Figure 4 is that we are directly matching how the spread in $[Mg/Fe]$ evolves with

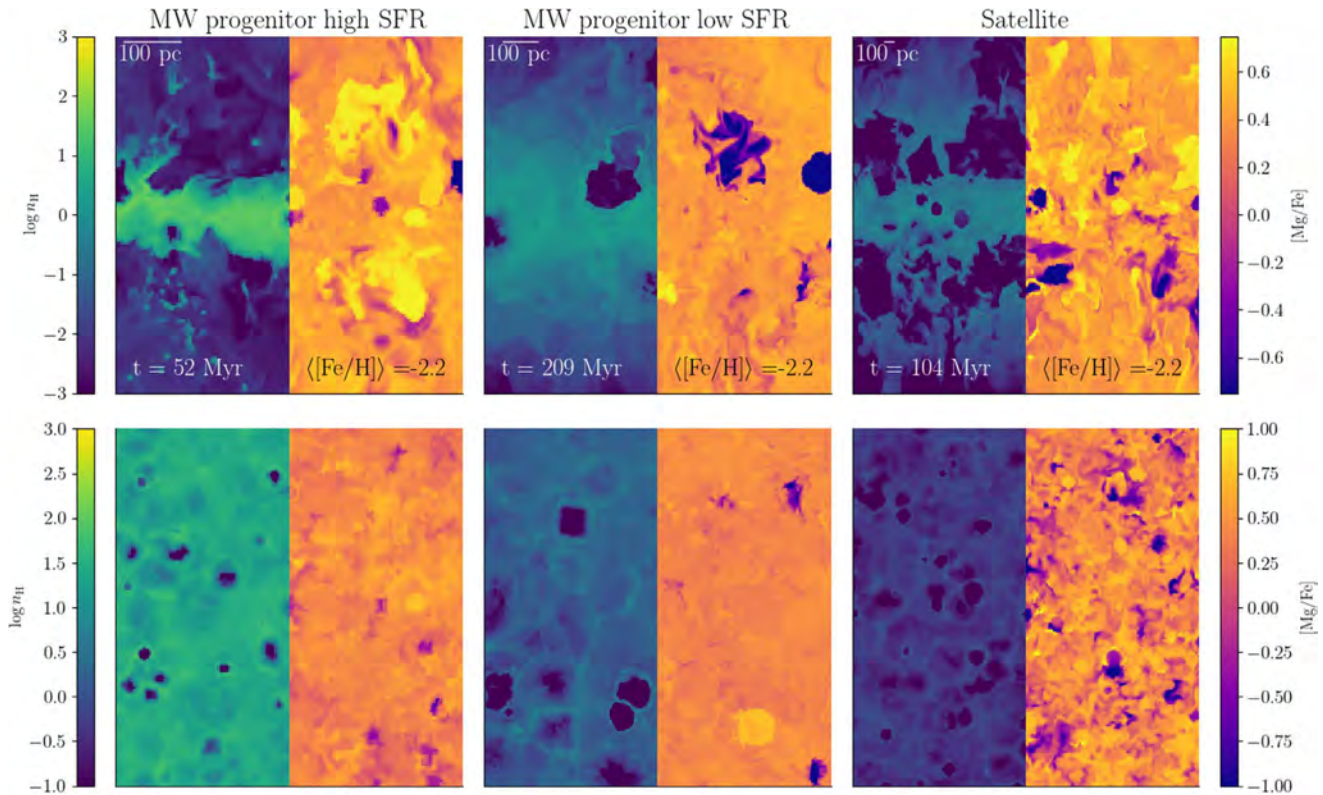


Figure C1. Same as Figure 2 but showing the $[Mg/Fe]$ abundance in place of the $[Fe/H]$ abundance from the simulations with intrinsic SN yield variations described in Section 2.1 and empirically derived in Appendix A.

$[Fe/H]$, which is initially sensitive to the assumed SN-to-SN yield variance and is then subsequently smoothed out by turbulent diffusion. As we have argued throughout this *Letter*, the strength of turbulent diffusion depends on the SFR and, as such, can be used to derive constraints on the star formation conditions giving rise to metal-poor stars.

ORCID iDs

Anne Noer Kolborg <https://orcid.org/0000-0001-7364-4964>
 Davide Martizzi <https://orcid.org/0000-0001-9497-1374>
 Enrico Ramirez-Ruiz <https://orcid.org/0000-0003-2558-3102>
 Hugo Pfister <https://orcid.org/0000-0003-0841-5182>
 Charli Sakari <https://orcid.org/0000-0002-5095-4000>
 Risa H. Wechsler <https://orcid.org/0000-0003-2229-011X>
 Melinda Soares-Furtado <https://orcid.org/0000-0001-7493-7419>

References

- Abohalima, A., & Frebel, A. 2018, *ApJS*, 238, 36
 Aoki, W., Beers, T. C., Christlieb, N., et al. 2007, *ApJ*, 655, 492
 Armillotta, L., Krumholz, M. R., & Fujimoto, Y. 2018, *MNRAS*, 481, 5000
 Arnone, E., Ryan, S. G., Argast, D., Norris, J. E., & Beers, T. C. 2005, *A&A*, 430, 507
 Audouze, J., & Silk, J. 1995, *ApJL*, 451, L49
 Beers, T. C., & Christlieb, N. 2005, *ARA&A*, 43, 531
 Bullock, J. S., Kravtsov, A. V., & Weinberg, D. H. 2001, *ApJ*, 548, 33
 Cayrel, R., Depagne, E., Spite, M., et al. 2004, *A&A*, 416, 1117
 Christensen, C. R., Dave, R., Brooks, A., Quinn, T., & Shen, S. 2018, *ApJ*, 867, 142
 Colbrook, M. J., Ma, X., Hopkins, P. F., & Squire, J. 2017, *MNRAS*, 467, 2421
 Dalcanton, J. J. 2007, *ApJ*, 658, 941
 de Avillez, M. A., & Mac Low, M.-M. 2002, *ApJ*, 581, 1047
 Deason, A. J., Mao, Y.-Y., & Wechsler, R. H. 2016, *ApJ*, 821, 5
 Draine, B. T. 2011, *Physics of the Interstellar and Intergalactic Medium* (Princeton, NJ: Princeton Univ. Press)
 Eggen, O. J., Lynden-Bell, D., & Sandage, A. R. 1962, *ApJ*, 136, 748
 Elmegreen, B. G. 1998, in *ASP Conf. Ser.*, 147, *Abundance Profiles: Diagnostic Tools for Galaxy History*, ed. D. Friedli (San Francisco, CA: ASP), 278
 Escala, I., Wetzel, A., Kirby, E. N., et al. 2018, *MNRAS*, 474, 2194
 Few, C. G., Courty, S., Gibson, B. K., Michel-Dansac, L., & Calura, F. 2014, *MNRAS*, 444, 3845
 Fielding, D., Quataert, E., Martizzi, D., & Faucher-Giguère, C.-A. 2017, *MNRAS*, 470, L39
 Fragile, P. C., Murray, S. D., Anninos, P., & Lin, D. N. C. 2003, *ApJ*, 590, 778
 Frebel, A. 2010, *AN*, 331, 474
 Frebel, A., & Norris, J. E. 2015, *ARA&A*, 53, 631
 Gilmore, G., Randich, S., Asplund, M., et al. 2012, *Msngr*, 147, 25
 Johnston, K. V., Bullock, J. S., Sharma, S., et al. 2008, *ApJ*, 689, 936
 Karlsson, T., Bromm, V., & Bland-Hawthorn, J. 2013, *RvMP*, 85, 809
 Karpov, P. I., Martizzi, D., Macias, P., et al. 2020, *ApJ*, 896, 66
 Kobayashi, C., Umeda, H., Nomoto, K., Tominaga, N., & Ohkubo, T. 2006, *ApJ*, 653, 1145
 Krumholz, M. R., & Ting, Y.-s 2018, *MNRAS*, 475, 2236
 Mac Low, M.-M., & Ferrara, A. 1999, *ApJ*, 513, 142
 Macias, P., & Ramirez-Ruiz, E. 2018, *ApJ*, 860, 89
 Mackey, J., Bromm, V., & Hernquist, L. 2003, *ApJ*, 586, 1
 Martizzi, D., Faucher-Giguère, C. A., & Quataert, E. 2015, *MNRAS*, 450, 504
 Martizzi, D., Fielding, D., Faucher-Giguère, C. A., & Quataert, E. 2016, *MNRAS*, 459, 2311
 Naiman, J. P., Pillepich, A., Springel, V., et al. 2018, *MNRAS*, 477, 1206
 Nomoto, K., Kobayashi, C., & Tominaga, N. 2013, *ARA&A*, 51, 457
 Pan, L., & Scannapieco, E. 2010, *ApJ*, 721, 1765
 Pan, L., Scannapieco, E., & Scalo, J. 2013, *ApJ*, 775, 34
 Petit, A. C., Krumholz, M. R., Goldbaum, N. J., & Forbes, J. C. 2015, *MNRAS*, 449, 2588
 Robertson, B., Bullock, J. S., Font, A. S., Johnston, K. V., & Hernquist, L. 2005, *ApJ*, 632, 872

- Roederer, I. U., Hattori, K., & Valluri, M. 2018, [AJ](#), **156**, 179
- Roederer, I. U., Preston, G. W., Thompson, I. B., et al. 2014, [AJ](#), **147**, 136
- Ryan, S. G., Norris, J. E., & Beers, T. C. 1996, [ApJ](#), **471**, 254
- Santistevan, I. B., Wetzel, A., Sanderson, R. E., et al. 2021, [MNRAS](#), **505**, 921
- Searle, L., & Zinn, R. 1978, [ApJ](#), **225**, 357
- Shen, S., Cooke, R. J., Ramirez-Ruiz, E., et al. 2015, [AJ](#), **807**, 115
- Shen, S., Kulkarni, G., Madau, P., & Mayer, L. 2017, [MNRAS](#), **469**, 4012
- Teyssier, R. 2002, [A&A](#), **385**, 337
- van Dokkum, P. G., Leja, J., Nelson, E. J., et al. 2013, [ApJL](#), **771**, L35
- Wang, Y., Nadler, E. O., Mao, Y.-Y., et al. 2021, [ApJ](#), **915**, 116
- Welsh, L., Cooke, R., & Fumagalli, M. 2021, [MNRAS](#), **500**, 5214
- Yang, C. C., & Krumholz, M. 2012, [AJ](#), **758**, 48

R-PROCESS PRODUCTION CONSTRAINTS FROM MIXING ARGUMENTS

This chapter includes the following article:

Constraints on the frequency and mass content of r-process events derived from turbulent mixing in galactic disks

Submitted to The Astrophysical Journal (ApJ)

Authors: Anne Noer Kolborg, Davide Martizzi, Phil Macias, Melinda Soares-Furtado and Enrico Ramirez-Ruiz

Constraints on the frequency and mass content of r-process events derived from turbulent mixing in galactic disks

ANNE NOER KOLBORG ^{1,2} ENRICO RAMIREZ-RUIZ ^{2,1} DAVIDE MARTIZZI ² PHIL MACIAS ² AND
MELINDA SOARES-FURTADO ^{3,*}

¹Niels Bohr Institute, University of Copenhagen, Blegdamsvej 17, DK-2100 Copenhagen, Denmark

²Department of Astronomy & Astrophysics, University of California, Santa Cruz, CA 95064, USA

³Department of Astronomy, University of Wisconsin-Madison, 475 N. Charter Street, Madison, WI 53703, USA

(Received; Revised; Accepted)

Submitted to ApJ

ABSTRACT

Metal-poor stars in the Milky Way (MW) halo display large star-to-star dispersion in their r-process abundance relative to lighter elements. This suggests a chemically diverse and unmixed interstellar medium (ISM) in the early Universe. This study aims to help shed light on the impact of turbulent mixing, driven by core collapse supernovae (cc-SNe), on the r-process abundance distribution in galactic disks. To this end, we conduct a series of simulations of small-scale galaxy patches which resolve metal mixing mechanisms at parsec scales. Our set-up includes cc-SNe feedback and enrichment from r-process sources. We find that the relative rate of the r-process events to cc-SNe is directly imprinted on the shape of the r-process distribution in the ISM, with more frequent events leading to narrower distributions. We consider also the fraction of metals that is lost on galactic winds and find that cc-SNe are able to efficiently launch highly enriched winds, especially in smaller galaxy models. This result suggests that smaller systems, e.g. dwarf galaxies, may require higher levels of enrichment in order to achieve similar mean r-process abundances as MW-like progenitor systems. Finally, we are able to place novel constraints on the production rate of r-process elements in the MW, $6 \times 10^{-7} M_{\odot}/\text{yr} \lesssim \dot{m}_{\text{rp}} \ll 4.7 \times 10^{-4} M_{\odot}/\text{yr}$, imposed by accurately reproducing the mean and dispersion of [Eu/Fe] in metal-poor stars. Our results are consistent with independent estimates from alternate methods and constitute a significant reduction in the permitted parameter space.

1. INTRODUCTION

The detailed physical ingredients required for r-process nucleosynthesis to take place were identified in the pioneering works of Burbidge et al. (1957) and Cameron (1957). Despite that, the dominant astrophysical site for r-process production in the early Universe remains highly debatable (Cowan et al. 2021), even after the landmark discovery of the kilonova associated with GW170817 (Abbott et al. 2017; Coulter et al. 2017; Kasen et al. 2017; Watson et al. 2019). To this end, metal-poor stars in the galactic halo can be used as unique probes of r-process element synthesis in the early Universe and could help elucidate the astrophysical assets of the dominant progenitor system (Snedden et al. 2008; Thielemann et al. 2017).

Abundance similarities observed among metal-poor halo stars with ages discrepant by billions of years but with a distribution that is representative of the solar system (Snedden et al. 2003; McWilliam et al. 1995; Snedden et al. 2008; Roederer et al. 2014) suggest that nuclear pathways responsible for r-process elements are rather robust and have been operating coherently over extensive periods of time in the assembly history of the Milky Way (MW). From the large star-to-star chemical abundance dispersion in r-process elements (such as Eu), with respect to the α elements (such as Mg), we can infer that the injection of r-process elements occurs at a dramatically diminished rate when compared to core-collapse supernovae (cc-SNe) (Wasserburg & Qian 2000; Fields et al. 2002). Additionally, the largest enhancements in [Eu/Fe] observed in metal poor stars imply that individual r-process sites need to synthesize a minimum of roughly $10^{-3} M_{\odot}$ r-process material (Macias & Ramirez-Ruiz 2018).

A central goal of this paper is to use a series of idealized hydrodynamic simulations of the response of galactic disks

Corresponding author: Anne Noer Kolborg
anne.kolborg@nbi.ku.dk

* NASA Hubble Postdoctoral Fellow

to SN feedback and metal mixing (Kolborg et al. 2022) to provide a deeper physical interpretation of the star-to-star r-process scatter observed in the MW in the metallicity extent [Fe/H] of approximately -3.0 to -1.5, where Fe enrichment is driven primarily by cc-SNe (Hotokezaka et al. 2018; Côté et al. 2019; Wanajo et al. 2021). The constraints derived from the abundance pattern of r-process elements in the MW may ultimately help decipher the dominant production mechanism in the early Universe.

The numerical modeling aimed at addressing the inhomogeneous enrichment of r-process elements in the MW has been primarily performed in a cosmological context (Shen et al. 2015; van de Voort et al. 2015; Naiman et al. 2018; Haynes & Kobayashi 2019; van de Voort et al. 2020, 2022). These studies are limited by resolutions of a few tens to hundreds of parsecs, and they inevitably involve “sub-grid” conjectures for SN feedback, star formation and turbulent mixing. As such, large uncertainties remain at scales at which metal injection and turbulent metal mixing are taking place. In preference, in this paper we propose to model the gas interactions in small patches of a galaxy disk simulations in order to effectively isolate the small-scale mixing effects of metals at sub parsec scales from cc-SNe and r-process producing events (such as neutron star mergers (NSM)) into the interstellar medium (ISM). Besides being computationally workable (Kolborg et al. 2022), investigating the distribution of r-process elements in these simulations and comparing them extensively with observational data of metal poor stars can, in turn, help constrain the frequency of events and the mass content of r-process per event.

This paper is structured as follows. In Section 2, we summarize the simulation setups and introduce the key parameters relevant for metal production in a wide range of galaxy models. Sections 3 through 6 present the results of our investigation. Initially, Section 3 shows the results of the turbulent mixing study in a given galaxy potential. This section serves to introduce the reader to the salient concepts and build an understanding of the key mixing processes from which we build in subsequent sections. In Section 4, we present the mixing results across the three galaxy potentials studied, while in Section 5 we investigate how changing the allowed height of r-process events influences the mixing and ejection of r-process mass. Section 6 investigates the production rate of r-process elements by studying how the spread of elements changes in response to variations in the mass per event (Section 6.1) and the relative rate of events (Section 6.2). This section concludes with a comparison between simulations and observations of [Eu/Fe] abundance of metal poor halo stars (Section 6.3). Section 7 gives a discussion of the implications of our simulation results, while Section 8 provides a final summary of our findings.

2. NUMERICAL METHODS

We use the hydrodynamic code RAMSES (Teyssier 2002) to simulate the evolution of gas in patches of galactic disks over timescales of hundreds of Myr. The fundamental simulation setup is the same as that used in Martizzi et al. (2016) and Kolborg et al. (2022), with the inclusion of a passive scalar field in order to trace the enrichment of r-process elements. In this section, we describe the salient aspects of the models as they pertain to this project. For additional details, we refer the interested reader to Martizzi et al. (2016) and Kolborg et al. (2022). The full suite of simulations used in this study are listed in Table 1.

2.1. Galaxy models

The simulations assume a static gravitational potential produced by gas, stars, and dark matter as described by Kuijken & Gilmore (1989). The parameters of this gravitational potential are varied to emulate three different types of galaxies (Kolborg et al. 2022).

The first model mimics an early MW progenitor with a high star formation rate (SFR). The second model simulates a MW progenitor with a more modest SFR. This second model is motivated by the recent findings of Wang et al. (2021), who argue that the presence of the Large Magellanic Cloud satellite suggests a MW progenitor with a less active SFR. The third model mimics a weak gravitational potential with a high gas fraction and low SFR, emulating the expected properties of a classical dwarf galaxy.

We employ cubic boxes¹ with periodic boundary conditions on the four edges perpendicular to the disk and outflow boundary conditions on the two parallel ones. The resolution of each simulation box is chosen such that the evolution of individual supernova remnants (SNR) are always well resolved. Specifically the cooling radius is resolved by at least 5 cells for least 94% of all remnants, in all galaxy models (Kolborg et al. 2022).

These various setups of galaxy disk patches at relatively high resolution, which capture the momentum injection of individual SNe, are able to effectively replicate the local conditions of galactic environments that might be representative of metal-poor stars assembled in the early MW and within accreted dwarf satellites.

2.2. Core collapse supernovae and neutron star mergers

cc-SNe and r-process events are seeded randomly with a constant rate (see the following section) and a flat distribution in space within fixed maximum allowed heights from the center of the galactic disk.

¹ RAMSES does not yet allow tall box simulations

Galaxy model	Σ_{SFR} $M_{\odot} / \text{kpc}^2 / \text{Myr}$	ρ_0 g/cm^3	z_{eff} pc	z_{SNe} pc	L pc	dx pc	T_{end} Myr	κ pc km/s	z_{NSM} z_{SNe}	f_{rp}	m_{rp} M_{\odot}
MW progenitor, high SFR	3×10^4	3.47×10^{-23}	40	100	1000	3.9	120	147	1.33	1×10^{-3}	1×10^{-2}
											1×10^{-1}
										1×10^{-2}	1×10^{-2}
										1×10^{-2}	1×10^{-3}
								1.0		1×10^{-2}	
								2.0			
MW progenitor, low SFR	1×10^3	2.08×10^{-24}	80	160	1000	3.9	250	213	1.33	1×10^{-3}	1×10^{-2}
Satellite	8×10^2	4.67×10^{-25}	365	800	4000	15.6	500	1460	1.33	1×10^{-3}	1×10^{-2}
											1×10^{-1}
										1×10^{-2}	1×10^{-2}
										1×10^{-2}	1×10^{-3}

Table 1. Overview of all the simulations presented in this project. The columns are: name of the galaxy patch model, surface density of star formation rate, mid-plane density initial condition, effective scale height of the gaseous disk, maximum vertical height of a cc-SNe, box side length, cell size, total evolution time, turbulent diffusion coefficient (Kolborg et al. 2022), maximum vertical height of an r-process event (as a fraction of the maximum cc-SNe altitude), relative rate of r-process to cc-SNe events, and mass of r-process material per r-process event.

We model cc-SNe using the sub-grid model for SN feedback implemented by Martizzi et al. (2015). In this model, each cc-SN event has an ejecta mass equal to the initial mass function (IMF) weighted average ($M_{\text{ej}} = 6.8 M_{\odot}$) and energy $E = 1 \times 10^{51}$ erg. Metals are introduced into the gas by individual cc-SNe, which are assumed to be chemically identical.

We apply the same sub-grid model of injection of mass and energy to the r-process producing events, however, we selected $M_{\text{ej}} = 1 \times 10^{-2} M_{\odot}$ and $E = 1 \times 10^{51}$ erg. These values reflect the properties of the ejecta inferred in the gravitational-wave triggered NSM event GW170717 (Kasen et al. 2017).

Although the morphology of a NSM remnant is highly asymmetric at early times (Rosswog & Ramirez-Ruiz 2002; Ramirez-Ruiz & MacFadyen 2010; Roberts et al. 2011), the subsequent radiative evolution is notably analogous to that of a SNR with similar total energy (Montes et al. 2016). The shell formation epoch, which occurs when the remnant becomes radiative, takes place by the time the mass of swept-up material reaches $M_c \approx 10^3 (n_{\text{H}}/1 \text{ cm}^{-3})^{-2/7} M_{\odot}$ (Karpov et al. 2020; Macias & Ramirez-Ruiz 2018; Cioffi et al. 1988; Thornton et al. 1998; Martizzi et al. 2015). The implications of this are twofold. First, sub-grid SN feedback models, like the ones used in this study, can be effectively used to resolve the key evolutionary phases of NSM remnants

(Montes et al. 2016). Second, our r-process injection models can be applied whether enrichment has occurred via extremely rare cc-SNe (e.g., Cowan & Thielemann 2004; Winteler et al. 2012; Nishimura et al. 2015; Mösta et al. 2018; Siegel et al. 2019), or through NSMs (e.g., Metzger et al. 2010; Roberts et al. 2011), provided that any contribution of other freshly-synthesized metals (i.e., non r-process) is less than those contained in the swept-up ISM mass by the time the blast wave reaches the cooling phase (Macias & Ramirez-Ruiz 2019). For the purposes of this study we focus our attention of NSMs as the source of r-process elements.

The maximum allowed height of standard cc-SNe events (z_{SNe}) is fixed to twice the scale height of the gaseous disk. The r-process events, on the other hand, are allowed to occur within a region defined by the parameter z_{NSM} . As a starting point, we set this value to $z_{\text{NSM}} = 1.33 z_{\text{SNe}}$. In Section 5, we explore how changes to this scale height impact the turbulent mixing process, and we discuss the limitations of our galaxy patch simulations.

2.2.1. Event and metal injection rates

The surface density rate of cc-SNe, Γ , is set by the rate of star formation in the galaxy patch, such that $\Gamma = \frac{\Sigma_{\text{SFR}}}{100 M_{\odot}}$. The rate of NSM events is set as a rate relative to standard cc-SNe, $\Gamma_{\text{NSM}} = f_{\text{rp}} \Gamma$. In this study we explore relative rates

of f_{rp} in the range $[10^{-3}, 10^{-2}]$, which is equivalent to 1 NSM event per $[100, 1000]$ cc-SNe.

For the purposes of this project, we are interested in studying the spread of r-process elements relative to elements produced by cc-SN. We select Fe as our representative cc-SNe element, with each cc-SNe yielding $M_{\text{Fe}} = 8 \times 10^{-2} M_{\odot}$ (Kolborg et al. 2022). We model r-process events as NSMs and assume that the entire ejecta is predominately comprised of r-process elements with a total mass $m_{\text{rp}} = M_{\text{ej,NSM}}$. That is, r-process events are assumed not to contribute to Fe enrichment, in our simulations.

As commonly carried out by the community, we designate Eu as the representative r-process element. We calculate the mass of Eu by applying the solar r-process abundance pattern (Asplund et al. 2009; Sneden et al. 2008) and calculating the mass fraction of Eu to all the r-process elements.

This is particularly useful when comparing with observations of metal-poor stars (Sneden et al. 2008). For the purpose of this study, we consider atomic mass number 69 as the strict lower limit for neutron capture element production ($A_{\text{min}} = 69$). In Section 7.1, we discuss the implications of this choice and the consequences for the results if $A_{\text{min}} = 90$, which corresponds to the second and third r-process peaks (Sneden et al. 2008).

α , iron peak and r-process elements are tracked as individual passive scalar fields. For the purposes of this study only iron and r-process elements are of interest and the individual scalar fields allow us to make adjustments to M_{Fe} and m_{rp} in post-processing. This approach allows us to simulate a wide range of r-process masses per event, $m_{\text{rp}} = [10^{-3}, 10^{-1}] M_{\odot}$, studying their effects on the metal enrichment of the ISM.

The metals injected into the ISM by these cataclysmic events are mixed through the galactic disk by turbulent diffusion, which is in turn driven by the energy and momentum deposition from the most common events. The advantage of galaxy patch simulations is that they allow us to effectively capture the driving of the turbulence by cc-SNe, as well as, accurately studying its effects on the mixing of other freshly synthesized metals that are produced by much rarer cataclysmic events.

2.3. Steady State

All simulations are initialized with the gas in hydrostatic equilibrium with the static gravitational potential. As cooling and SNe feedback turn on simultaneously some of the thermal pressure support falls and turbulent pressure support increases. Hence, at early times, the disk is primarily supported by thermal pressure, while at later times, the disk is supported by both thermal and turbulent pressure driven by cc-SNe. Since information needs to be effectively communicated to all regions before turbulent motions in the bulk

of the disk reach a statistical steady state, an initially transient phase is produced. The duration of this phase is usually well described by the characteristic relaxation time in our disk models, $t_r = 4z_{\text{eff}} \langle \sigma_v \rangle^{-1}$, where $\langle \sigma_v \rangle$ is the time averaged, mass-weighted velocity dispersion of the gas (Kolborg et al. 2022). In what follows, we neglect this initial phase, which lasts $\approx \frac{1}{5} T_{\text{end}}$ in all of our simulations (Table 1). In this work, we only discuss the results from the steady state of the simulations.

3. METAL MIXING IN HIGH SFR ENVIRONMENTS

In this section, we examine the mixing of elements in the MW progenitor model with high SFR. For simplicity, we limit our attention to a single instance of this model where r-process events take place at a rate relative to cc-SNe of $f_{\text{rp}} = 10^{-3}$ and each event yields a mass of r-process elements of $m_{\text{rp}} = 10^{-2} M_{\odot}$. This assumes that cc-SNe occur in a region of $z_{\text{SNe}} = 100 \text{ pc}$, while the r-process events occur in the region defined by $|z| \leq 1.33 z_{\text{SNe}}$. We use this representative model to present a detailed account of the metal mixing features that may be present in the interstellar gas. These salient features can result naturally when one examines metal turbulent mixing by events occurring at disparate rates, yet their exact properties depend on the specific galaxy model and more sensitively on f_{rp} and m_{rp} .

3.1. The Tomography of a Galaxy Patch

In Figure 1 we show the density-weighted projections of the thermodynamic properties of the gas along two axes in the simulation box. The density (left-hand column) and temperature (right-hand column) projections along an axis perpendicular to the galactic disk (top row) clearly illustrate how the momentum deposition from cc-SNe ejects gas from the disk in the form of a hot, rarefied galactic wind. From another point of view, the projection along the galactic disk plane (similar to a face-on view of the galaxy, bottom row) distinctively shows individual cc-SN and r-process remnants. They can be observed as nearly spherical regions of lower density and higher temperature gas, which are embedded in the denser, cooler, star forming gas.

In addition to momentum and energy, the individual events inject new metals: iron peak elements in the case of cc-SNe and heavy metals in the case of r-process events. These metals are mixed into the surrounding ISM by the turbulent diffusion, which is driven primarily by cc-SNe. Figure 2 shows the density-weighted projections of the metal abundances in the gas for both Fe and Eu enrichment.

Several key aspects can be noted by examining the maps shown in Figure 2. First, the rarefied galactic wind is highly enriched in Fe and Eu when compared to cold, dense gas in the mid-plane. This is primarily due to the low density of the hot wind within this region, which implies that even the mix-

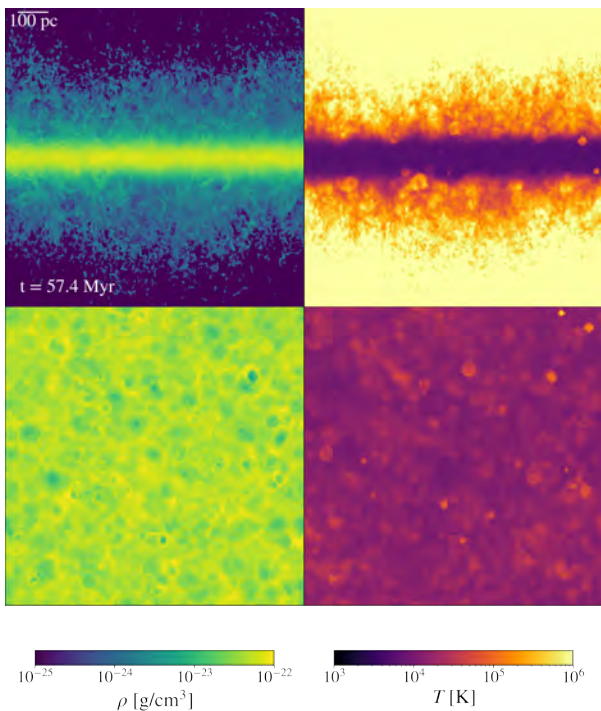


Figure 1. Density-weighted projection plots of the thermodynamic properties of the gas in the MW progenitor with high SFR (left-hand column: density; right-hand column: temperature). The top row presents an edge-on view of the galaxy disk, while the bottom row presents a face-on view. The SNe drive turbulent mixing in the disk and a galactic wind. Individual SNR are clearly visible in the plane of the disk.

ing of a small amounts of metals can lead to a comparatively high enrichment.

Second, the abundance of $[\text{Fe}/\text{H}]$ is relatively uniform across the disk and within the galactic wind region. The full span of $[\text{Fe}/\text{H}]$ variations is generally small. Across the disk, we observe localized $[\text{Fe}/\text{H}]$ variations where neighboring cc-SN remnants remain compact and fail to overlap (at scales of a few tens of pc). These localized Fe enhancements are then subsequently smoothed out as the enriched gas is given more time to expand and mix throughout the disk (Kolborg et al. 2022). Yet, individual remnants always expand to characteristic lengths that are smaller than the disk scale height.

Lastly, $[\text{Eu}/\text{H}]$ is inspected in the middle panels of Figure 2 to exhibit significantly larger scatter in abundance concentrations than $[\text{Fe}/\text{H}]$ in the left panels. This originates from the comparative rarity of r-process metal injection, which naturally produces a chemically inhomogeneous and unmixed ISM at these early epochs. As more events are injected and r-process material diffuses and mixes, we can expect these metal concentrations to be gradually smoothed out.

3.2. Metal mixing as a function of time

From visual inspection of the abundance maps alone, we can gain a clear insight regarding the differential distribution of Eu and Fe in the galactic disk. In this section, we present a quantitative description of these differences.

Figure 3 depicts the volume weighted mean and 1σ spread of the gas abundances when considering all the gas in the simulation volume (global) and the cold, dense gas in the disk. For reference, the snapshots depicted in Figures 1 and 2 correspond to a simulation time $57.4\text{Myr} \approx 0.475T_{\text{end}}$.

Our scheme does not explicitly include star formation so, for the purpose of making an informed matching, we isolate the cold, dense gas within the disk ($|z| \leq z_{\text{eff}}$), that is the most apt to form stars. We impose a temperature boundary of $T \leq 10^4\text{K}$, which is related to the cooling function temperature floor, and a density limit of $\rho \gtrsim \rho_0/4$ (see Table 1).

As the simulation evolves, the $[\text{Fe}/\text{H}]$ within the disk is gradually enriched as ensuing cc-SNe increase the mean Fe metallicity of the gas. At the same time, cc-SNe feedback drive outflows which cause Fe to spread from the disk onto the rarefied wind. The volume weighted average tends to emphasize the abundance of the hot, rarefied gas, which has a large volume filling factor. This becomes evident when examining the underlying distributions at fixed times shown in Appendix A. The global gas distribution of $[\text{Fe}/\text{H}]$ has a very narrow peak at high metallicities (which drives the mean value) and a fairly long tail at lower metallicities (which influences the spread calculation). By contrast, the global and disk $[\text{Fe}/\text{H}]$ distributions are rather similar when considering the mass weighted distributions. A similar behavior is seen for the $[\text{Eu}/\text{H}]$ distributions, albeit with much broader "peaks" given the lesser degree of metal mixing which results from less frequent injections.

Initially, the metal distributions of both $[\text{Fe}/\text{H}]$ and $[\text{Eu}/\text{H}]$ are highly inhomogeneous because there are significant regions that contain unmixed material. Due to its much more frequent injection, $[\text{Fe}/\text{H}]$ is more uniformly distributed than $[\text{Eu}/\text{H}]$. The impact of higher metal injection rates on the abundance of $[\text{Fe}/\text{H}]$ is twofold. First, the spread in the distribution is much narrower than the one seen for $[\text{Eu}/\text{H}]$ in both the global and the cold, dense gas at all times in the simulation. In other words, there is a higher degree of homogenization of Fe than Eu as cc-SN products migrate and mix across the disk more effectively. Second, the evolution of the mean metallicity with time, which is caused by the rate of metal injection, is much swifter for $[\text{Fe}/\text{H}]$ than for $[\text{Eu}/\text{H}]$. As time evolves, the localized inhomogeneities in both $[\text{Fe}/\text{H}]$ and $[\text{Eu}/\text{H}]$ are smoothed out and the evolution of the mean abundance becomes more gradual as each new injection of metals contributes progressively less to the total metal content. Yet r-process products migrate and mix throughout the box much more slowly. This is because large amount of freshly synthesized r-process material are injected

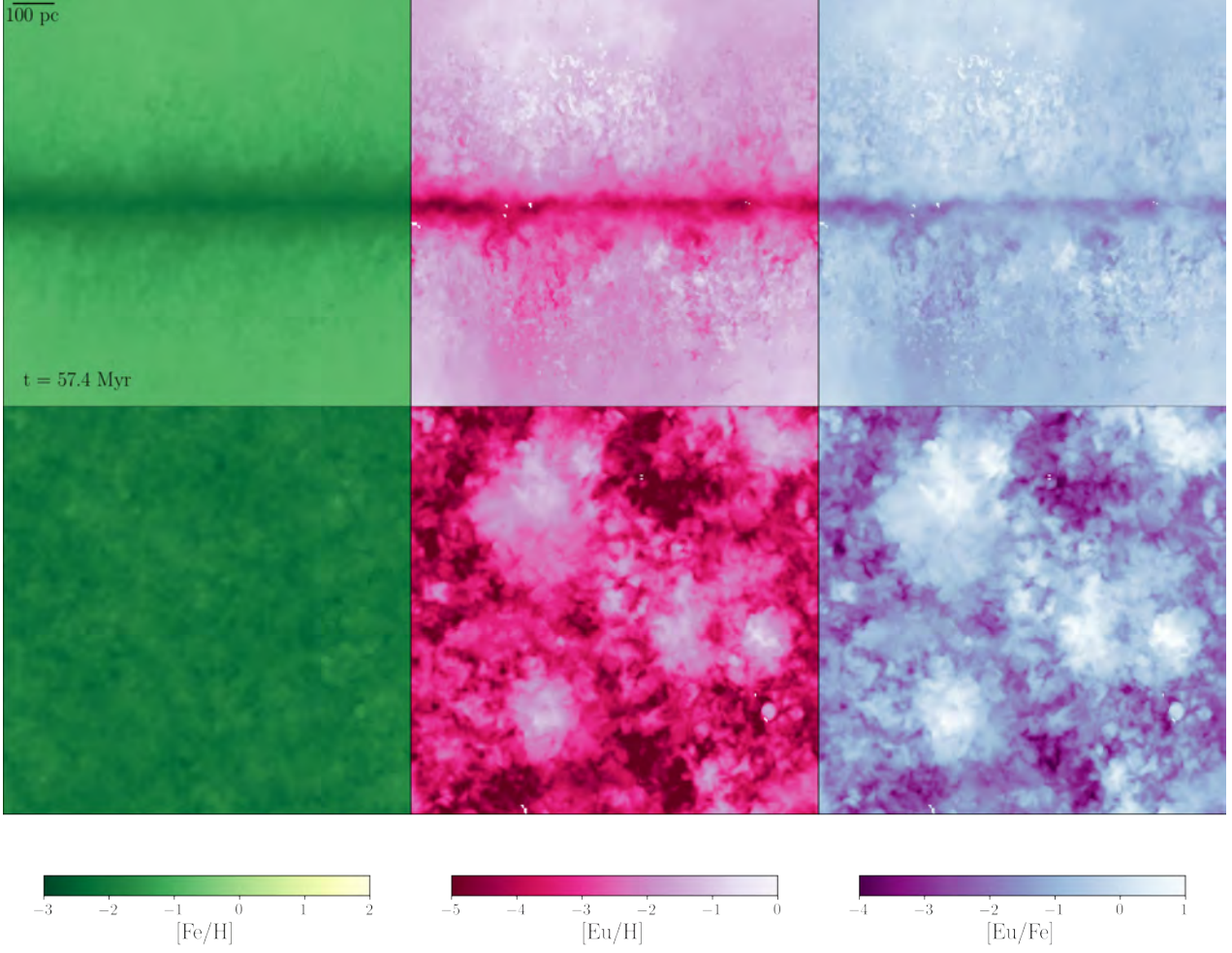


Figure 2. Density weighted projection plots of the metal mixing properties of the gas in the galaxy patch simulation shown in Figure 1. The top row presents an edge-on view of the galaxy disk, while the bottom presents a face-on view. The panels show the abundances of [Fe/H] (left), [Eu/H] (middle) and [Eu/Fe] (right). Both Fe and Eu are efficiently ejected from the galactic disk and drastically increase the metal abundance in the galactic wind region. The effects of the relative rate of metal injection on the metal mixing of Fe and Eu are clearly seen; the less frequently injected Eu is less evenly distributed than Fe, which is injected more frequently.

at a rate that is usually faster than the the rate at which turbulent mixing smooths them down.

3.3. Mass loading factor

Through injection of energy and momentum, cc-SNe drive material out of the disk and launch galactic winds. In this section, we consider the mass loading factor of the wind, which is commonly defined as (e.g. [Martizzi et al. 2016](#); [Li & Bryan 2020](#)):

$$\eta(z) = \frac{\dot{M}_{\text{out}}(z)}{\text{SFR}}, \quad (1)$$

\dot{M}_{out} denotes the rate at which mass is leaving the galaxy.

Analogously, the metal mass loading factor is defined as the ratio of the mass in metals leaving the galaxy to the ratio

of mass of metals that are injected ([Li & Bryan 2020](#)):

$$\eta_{Z_i}(z) = \frac{\dot{M}_{Z_i, \text{out}}(z)}{\dot{M}_{Z_i, \text{inj}}}. \quad (2)$$

Here we calculate the rate of metal injection as

$$\dot{M}_{Z_i, \text{inj}} = \dot{n}_{\text{SNc}} M_{\text{ej}} y_{Z_i} f_{Z_i}. \quad (3)$$

y_{Z_i} is the fractional yield of element Z_i produced by a particular event ejecting a mass M_{ej} , so that $M(Z_i) = M_{\text{ej}} y_{Z_i}$. The parameter f_{Z_i} denotes the fraction of events that produce metal Z_i relative to the rate of cc-SNe. For cc-SN elements $f_{Z_i} = 1.0$, while for r-process elements $f_{Z_i} = f_{\text{rp}}$.

We estimated the rate at which mass leaves the disk by measuring the mass flux that streams through a surface parallel to the disk with an out-flowing z -velocity. We measure

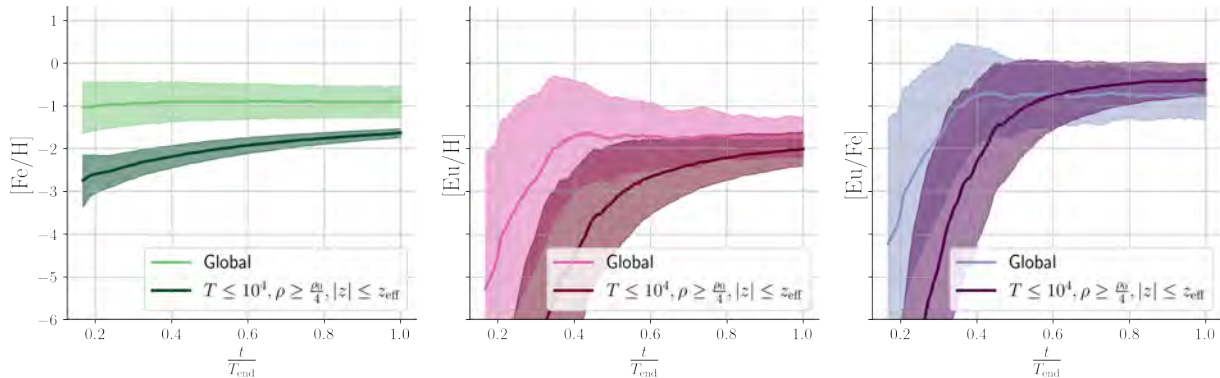


Figure 3. Temporal evolution of the volume weighted mean and 1σ spread of the abundances of $[\text{Fe}/\text{H}]$ (left), $[\text{Eu}/\text{H}]$ (middle) and $[\text{Eu}/\text{Fe}]$ (right) for the MW progenitor with high SFR. The global values refer to the mean and spread when considering all the gas in the simulation volume, while the cold, dense, disk material is defined by gas located at $|z| \leq z_{\text{eff}}$ and with the following thermodynamic properties: $T \leq 1 \times 10^4$ K and $\rho \geq \rho_4/4 \approx 1 \times 10^{-23}$ g cm $^{-3}$. The spread in $[\text{Fe}/\text{H}]$ is always significantly less than the spread of $[\text{Eu}/\text{X}]$ due to cc-SN metals being injected at much higher rates.

the outflow rate at three different heights. In order of increasing height from the disk midplane, the chosen distances are as follows: $|z| = 3z_{\text{eff}}$, $|z| = 2z_{\text{SNe}}$, and $|z| = \frac{l}{2} - dx$. The last measurement height is one cell size away from the edge of the simulation domain. The physical size of the relative heights are listed in Table 1 for each galaxy model.

It is important to note that the local boxes we consider in this study do not have a clearly defined escape velocity (Martizzi et al. 2016) and the wind mass loading factor is observed to decline with increasing box height. Martizzi et al. (2016) studied SNe feedback in the galaxy patch simulations and argue that the structure of the galactic winds are not always well captured by these boxes. However, in the case of the MW progenitor with high SFR simulation (equivalent to their model FX-ULTRA-MW-L8), they found that the global wind properties are well modelled within $|z| \lesssim 200$ pc, which is equivalent to $2z_{\text{SNe}}$ for that model. Therefore, we proceeded with the analysis of the wind loading, focusing on results from heights comparable to this value. Moreover, Li & Bryan (2020) compared loading factors from a wide range of simulations, including the work by Martizzi et al. (2016), and found similar values reported across different global and local studies. This lends further credence to the robustness of the derived loading factors in this study.

Figure 4 shows the evolution of the loading factors relating to the total mass, cc-SN elements, and r-process elements during the steady state of the simulation. The mass loading factor has a nearly constant value throughout the evolution of the simulation, with values that are consistent with the results of Martizzi et al. (2016). The evolution of loading factor of Fe closely traces η_M . This seems natural to expect for a galactic wind driven primarily by momentum injection from the same cc-SNe that are also injecting Fe. Interestingly, η_{Ziron} , indicates that only about $\approx 10\%$ of the injected metals are in-

corporated into the galactic winds. The evolution of η_{Zrp} , on the other hand, is much less smooth and contains large metal outbursts. The location of these outbursts closely follow the injection timing of r-process events, which are marked by dark vertical lines in Figure 4.

The rise of r-process material in the wind takes place near the local injection sites, which produce large amounts of heavy elements. This freshly synthesized r-process material does not have time to mix effectively within the disk before being expelled. The smoothing of the individual outburst with z is caused by r-process metals further mixing with wind material. It is noteworthy that the loading factors of cc-SN and r-process elements are very similar to each other at all times in the simulation, suggesting that r-process metals are carried out of the disk by winds driven by cc-SNe only after mixing significantly with the ISM. On average, the mass loading factor of iron elements is $\approx 7.5\%$, while the mass loading factor of r-process elements is $\approx 11\%$ (both measured at $|z| = 2z_{\text{SNe}}$). The slightly higher mass loading factor implies that r-process elements are retained slightly less effectively than cc-SN elements. This is closely related to the r-process metal outbursts captured in Figure 2, which occurs because individual r-process events do not have time to mix effectively with the surrounding ISM before being expelled from the disk.

4. METAL MIXING IN DIFFERENT GALAXY TYPES

In this section, we consider the influence of the galaxy potential on the turbulent mixing of the freshly synthesized metals. To facilitate comparison, we assume standard values for all parameters that do not relate to the galaxy type. More explicitly, the relative rate of NSM to cc-SN events is set to $f_{\text{TP}} = 10^{-3}$, the mass per event is set to $m_{\text{TP}} = 10^{-2} M_{\odot}$, and the scale height of NSM is set to $z_{\text{NSM}} = 1.33z_{\text{SNe}}$.

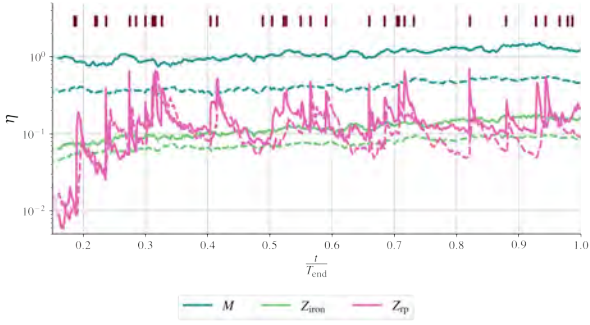


Figure 4. Evolution of the loading factors of the total, iron and r-process mass (see legend) as a function of time in the MW progenitor with high SFR. The loading factor is shown for two different heights in the potential: $|z| = 3z_{\text{eff}}$ (solid lines) and $|z| = 2z_{\text{SNe}}$ (dashed lines). The dark vertical lines indicate the timing of r-process injections in the disk. The iron loading factor evolves very similarly to the total mass loading factor albeit with a different normalization. The r-process loading factor is strongly correlated with the injection of new r-process events. Interestingly, the loading factors of iron and r-process elements are comparable to each other, suggesting that both metal groups are carried away at similar rates irrespective of their very different injection rates.

4.1. Abundance evolution

Figure 5 illustrates the evolution of the (volume-weighted) mean and spread of the $[\text{Fe}/\text{H}]$, $[\text{Eu}/\text{H}]$, and $[\text{Eu}/\text{Fe}]$ abundances as a function of time in each of the three galaxy potentials. Similar to Figure 3, the mean and spread are shown for all the gas in the box (global) and the cold, dense gas within the disk. For all galaxy types, the global spread is observed to be larger than the spread of the cold, dense gas. We also see a significant offset between the mean abundance of the global gas and the cold, dense gas for all galaxy models. This offset is the smallest for the satellite model and is related to the lower gas density in the disk, which naturally leads to a higher volume filling factor of the enriched material in both the wind and the disk regions.

As a whole, galaxy models with lower SFRs take longer to achieve the same mean $[\text{Fe}/\text{H}]$ metallicity. As such, Fe is given more time to migrate throughout the disk. This is because the lower-density gas associated with a low SFR allows each cc-SN remnant to reach larger physical sizes than remnants in higher-density environments. As such, galactic disks with lower SFRs show less spread in abundances at a comparable average $[\text{Fe}/\text{H}]$ metallicity. As anticipated, the spread of $[\text{Eu}/\text{H}]$ is generally larger than that of $[\text{Fe}/\text{H}]$, particularly in the cold, dense gas phase.

In contrast with $[\text{Fe}/\text{H}]$, the $[\text{Eu}/\text{H}]$ spread is primarily driven by the relative rate of r-process to cc-SN events (which is the same in all simulations) and is less dependent on the SFR. It is compelling to note that the evolution of $[\text{Eu}/\text{H}]$ for the MW progenitor with low SFR is rather odd (see mid-

dle panel in Figure 5). This transpires because the SFR is so low in this model that the galaxy patch is host to only two r-process events over its entire evolution. As a result, very metal poor stars in this model will not be enriched with any r-process material until after the first event takes place. This behavior clearly illustrates that galaxies with very low global SFRs might not be enriched with r-process material, as it is commonly expected to be the case for ultra faint dwarf (UFD) galaxies in the MW halo. Most of these systems are very metal poor and exhibiting low r-process enhancements (Cowan et al. 2021). A notable exception is Reticulum-II, which has been shown to contain several highly enriched stars (Ji et al. 2016a,b, 2022; Roederer et al. 2016). In this context, it is interesting to consider the likelihood that any one small system hosts an r-process event given the very low SFRs associated with these systems.

4.2. Mass loading factors

One of our goals in this study is to understand the effects that turbulence driven by cc-SNe in galactic disks has on metal mixing. cc-SNe increase the mean metallicity of the gas in the disk and drive turbulent mixing, which prompts the metals to diffuse across the disk. At the same time, the momentum and energy that goes into driving turbulence launches galactic winds and drives metals out of the disk. Figure 6 shows the temporal evolution of the loading factors of mass, iron, and r-process metals for the three different galaxy potentials. The loading factors are all measured at $|z| = 2z_{\text{SNe}}$ (see Table 1). As expected, the mass loading factor is significantly larger for weaker galaxy potentials, highlighting the greater relative importance of cc-SN energetics in these systems. This result is consistent with what is frequently ascertained in dwarf galaxy simulations (e.g., Fielding et al. 2017).

During the simulations, the satellite galaxy model and the MW progenitor with low SFR release $\approx 35\%$ and $\approx 10\%$ of their initial mass to cc-SNe-driven winds, respectively. In contrast, the MW progenitor model with high SFR loses $\lesssim 5\%$ of its initial mass (Kolborg et al. 2022). This mass loss is naturally explained by the mass loading factors observed for these less massive systems. The associated larger mass loading factors in low mass systems are, for example, necessary in order to interpret the observed galaxy stellar mass function (e.g., Li & Bryan 2020).

Across the different galaxy potentials, the loading factor of iron and r-process elements are remarkably similar to each other, with a major caveat being that the MW progenitor with low SFR undergoes very low r-process mass loading before the first event occurs at $t \approx 0.6T_{\text{end}}$.

Models with fewer cc-SNe give the freshly synthesized r-process metals more time to diffuse and travel across the disk and, as a result, show less prominent r-process outbursts

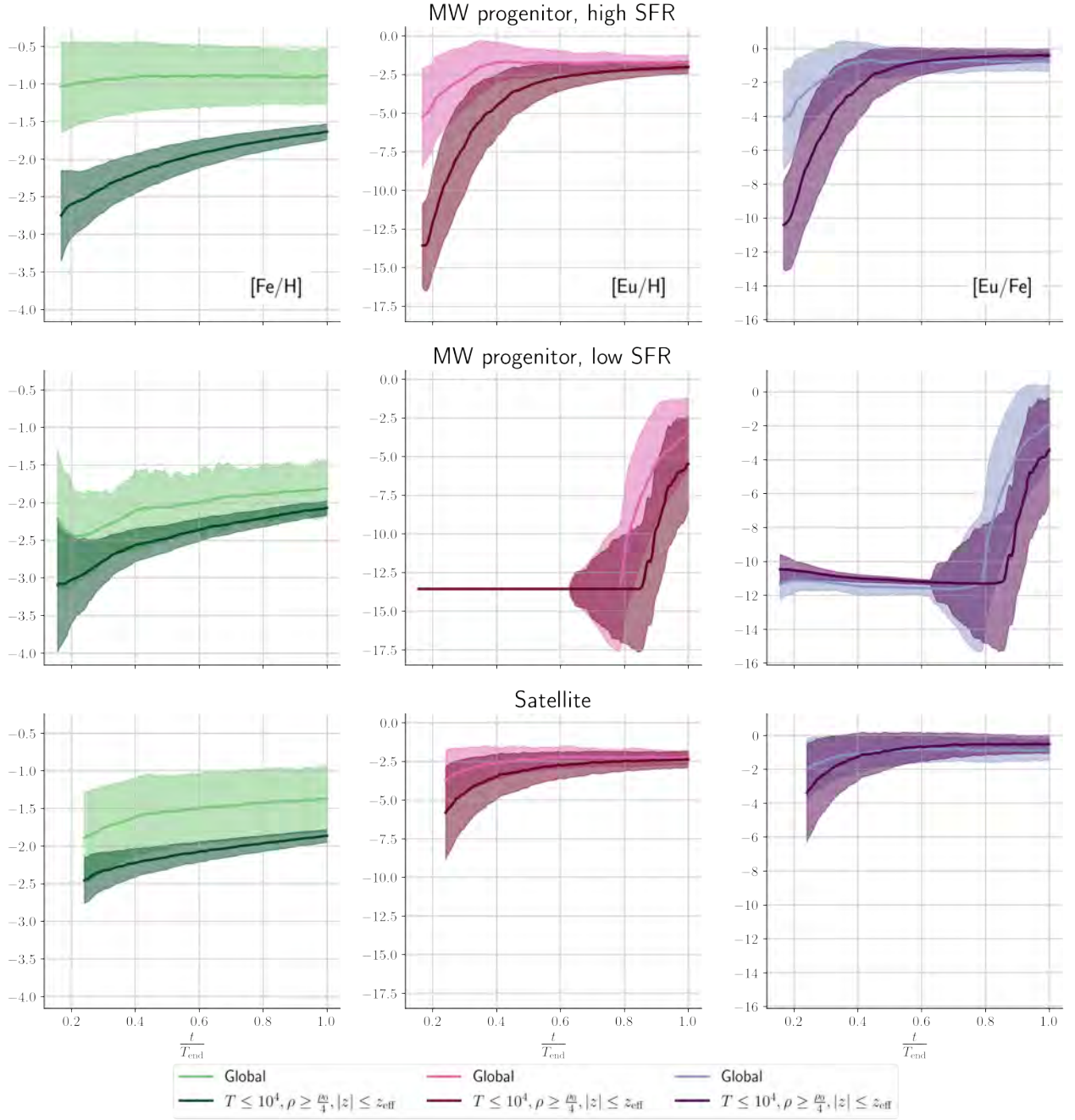


Figure 5. The temporal evolution of the volume weighted mean and 1σ of [Fe/H] (left), [Eu/H] (middle), and [Eu/Fe] (right) in each of the three galaxy potentials. From top to bottom we present the results for the MW progenitor with high SFR, the MW progenitor with low SFR, and the satellite model. The abundances were calculated for all the gas in the box (global) and for the cold, dense gas in the disk as done in Figure 3. Overall, the evolution of the abundances are similar in all three galaxy potentials. Yet, the difference between the global and the cold, dense gas mean values is smaller for the weaker galactic potentials, implying larger volume filling factors of enriched gas in all gas phases.

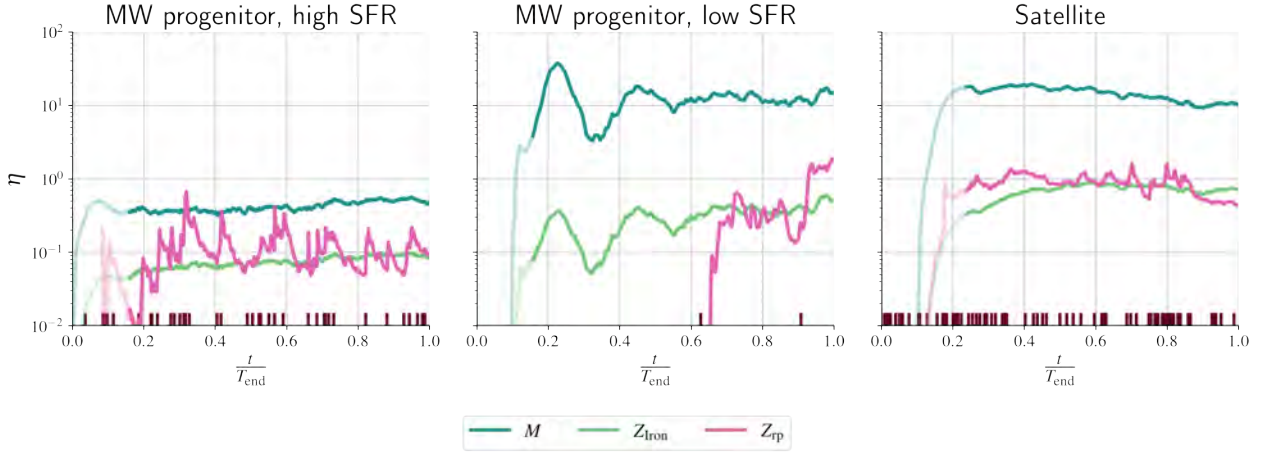


Figure 6. Loading factors of total, iron and r-process mass (see legend) measured at $|z| = 2z_{\text{SNe}}$ for three different galaxy potentials: MW progenitor with high SFR (left); MW progenitor with low SFR; and satellite galaxy (right). The dark vertical lines along the bottom of each panel denote the times at which r-process events take place. The times are normalized to the run times of the simulations (see Table 1). The initial phase (before steady-state is reached) is indicated by lower opacity color. The loading factors are generally larger for weaker gravitational potentials. The weaker gravitational potentials also display smaller differences in loading factors at greater distances from the disk (see Appendix B), indicating the material streams from the disk more easily.

when compare with the MW progenitor with high SFR. The average mass loading factor of iron and r-process elements in satellite galaxy model (MW progenitor with low SFR), at $|z| = 2z_{\text{SNe}}$, are $\approx 70\%$ ($\approx 30\%$) and $\approx 89\%$ ($\approx 22\%$), indicating significantly less retention of metals in the ISM than the MW progenitor with high SFR. In essence, higher mass injection rates of r-process material are necessary in a satellite galaxy in order to average $[\text{Eu}/\text{H}]$ abundance comparable to a more massive system.

5. VARYING THE SCALE HEIGHTS OF R-PROCESS INJECTION AND ITS EFFECT ON METAL MIXING

Here we examine the impact of altering the scale height of r-process metal injection sites on metal mixing. The galaxy patch setup does not lend itself well to studying large offsets from the disk (e.g., Rosswog et al. 2003; Zheng & Ramirez-Ruiz 2007; Kelley et al. 2010; Behroozi et al. 2014; Zevin et al. 2022), as would be expected for systems with long merger timescales (t_{delay}) and large velocity kicks (v_{kick}). This setup can, however, be used to probe the impact of modest event offsets, $\bar{z} \approx 140(t_{\text{delay}}/10\text{Myr})(v_{\text{kick}}/20\text{km s}^{-1})$ pc, on the subsequent mixing efficacy, as could be envisaged for r-process production in fast-merging double neutron stars (Ramirez-Ruiz et al. 2015; Safarzadeh et al. 2019) or rare cc-SNe (Winteler et al. 2012; Nishimura et al. 2015; Mösta et al. 2018). These prompt channels are commonly argued to be more effective at enriching very metal poor stars with r-process products (e.g., Siegel et al. 2019; Cowan & Sneden 2006), which is the central focus of this study.

In this section, we present results for three different simulations. For these runs, we use the same galaxy type. We select the MW progenitor with high SFR in view of the fact that, as we argued in Section 4, r-process products in this model are given the smallest amount of time to migrate throughout the disk. As such, the effects of varying the scale height of metal injection should be particularly obvious for this model. The relative rate and mass per event of r-process events remain unchanged. That is, $f_{\text{rp}} = 10^{-3}$ and $m_{\text{rp}} = 10^{-2} M_{\odot}$. Yet, the maximum allowed height of NSM is varied between the following three scale heights: $z_{\text{NSM}} = z_{\text{SNe}}$, $z_{\text{NSM}} = 1.33z_{\text{SNe}}$, $z_{\text{NSM}} = 2z_{\text{SNe}}$. To facilitate comparison, the injection procedure for cc-SNe remains the same in all simulations.

5.1. Mass loading of r-process elements

It is natural to expect that the event scale height will influence the rate at which r-process material is lost via galactic winds. We explore this assumption here by examining the consequences of increasing z_{NSM} on η_{Zrp} .

We expect η_{M} and η_{Ziron} to remain unchanged in these models as cc-SNe, whose injection properties are the same in all models, dominate the energy and momentum injection in the

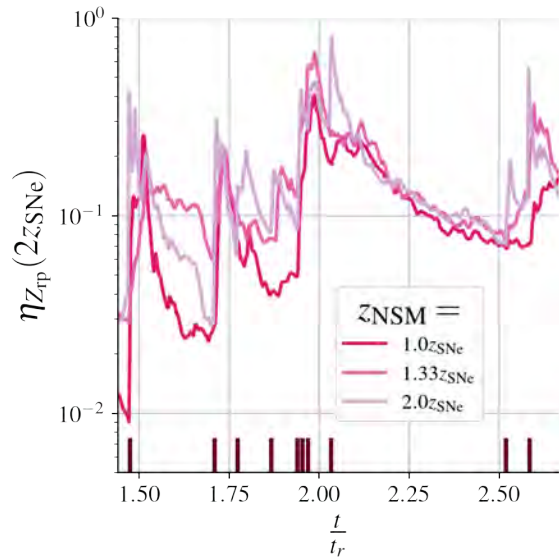


Figure 7. The temporal evolution of the metal r-process loading factor, η_{Zrp} , in units of the characteristic relaxation time, t_r , for varying z_{NSM} in the MW progenitor high SFR model. η_{Zrp} is measured here at $|z| = 2z_{\text{SNe}}$. The dark vertical lines denote the times at which r-process events transpire. The r-process retention is slightly altered by changes in z_{NSM} , with more prominent metal outbursts observed when injection takes place at higher scale heights.

disk. In essence, cc-SNe are primarily responsible for driving both the turbulent mixing and the resulting galactic wind in these models. This is confirmed by our simulations which show that the average η_{M} and η_{Ziron} are similar to within a few percent in all simulations.

In contrast, the average mass loading factor of r-process elements vary perceptibly with z_{NSM} (see Figure 7). More precisely, the values of η_{Zrp} measured at $|z| = 2z_{\text{SNe}}$, are $\approx 8.2\%$ ($z_{\text{NSM}} = z_{\text{SNe}}$), $\approx 12.3\%$ ($z_{\text{NSM}} = 1.33z_{\text{SNe}}$)² and $\approx 12.6\%$ ($z_{\text{NSM}} = 2z_{\text{SNe}}$). As expected, the model where r-process events are confined to a region that is significantly larger than the one for cc-SNe shows the largest η_{Zrp} , indicating slightly less effective retention of r-process metals in the ISM.

5.2. Abundance evolution

Having found only a small increase in η_{Zrp} with r-process event offsets, we now consider if the location of events are capable of altering the metal abundance of the ISM. Figure 8 shows the volume-weighted mean and 1σ of $[\text{Eu}/\text{Fe}]$ as a function of the mean $[\text{Fe}/\text{H}]$ for the global (left) and cold, dense, disk gas (right) in the three simulations. The definition

² There is a small difference between the average reported here and in section 3.3. The number reported in this section includes only the time that is common among the three simulations, this shorter time span leads to small differences in the reported figures.

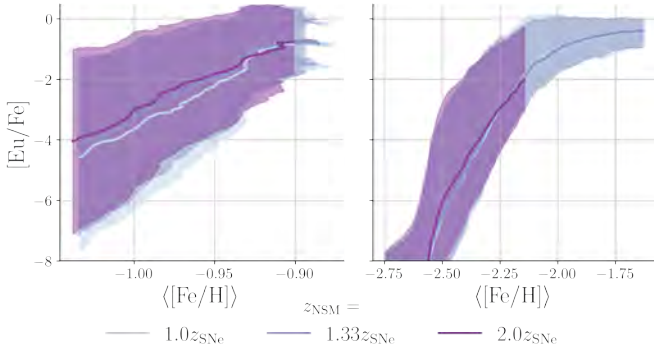


Figure 8. The temporal evolution of the volume weighted mean and 1σ of $[Eu/Fe]$ as a function of the global mean $[Fe/H]$ abundance in MW progenitor with high SFR simulations with varying z_{NSM} (see legend). The $[Eu/Fe]$ abundance is shown in the left panel for the entire simulation box and in the right panel for the cold, dense gas in the disk (defined as for Figures 3 and 5). We note no discernible difference in the mean abundance of the gas, suggesting that the offset of events does not strongly influence the observed abundances of r-process elements within the limits examined here.

of cold, dense disk gas remains unchanged from Sections 3.2 and 4.1.

While there is a trend of slightly higher mean $[Eu/Fe]$ abundances with increasing event offsets in the global measurement, we note no discernible difference when considering only the cold, dense gas. This is to be expected as the retention of r-process material in these models is $\gtrsim 90\%$. Both the mass loading factors and abundances are found to be similar across models with different allowable scale heights of r-process events. Thus, we conclude that the range of offsets examined here do not produce measurable changes in observed galaxy properties.

We caution the reader that global disk galaxy simulations are necessary in order to study the mixing effects of r-process metals deposited by NSM with large kicks and long merger times. This will require a large range of scales to be resolved simultaneously, which is exceedingly challenging given the complexity of the interplay between the various galaxy assembly mechanisms at all scales. Considering the somewhat emerging stage of modeling in the field, this study amounts to a sizable improvement within the stated limitations in our understanding of how the location of metal injection within the galaxy influences the inhomogeneous enrichment of the ISM and the mixing of r-process elements.

6. ON THE REPERCUSSIONS OF THE PRODUCTION RATE OF R-PROCESS MATERIAL ON METAL MIXING

The purpose of this paper is to help isolate some of the key mechanisms that regulate turbulent mixing of r-process elements in galactic disks and, in particular, how the statistics of abundance variations in stars can help constraint astrophysi-

cal r-process synthesis models. It seems reasonable to expect that a general r-process production scheme we would have m_{rp} and f_{rp} as essential parameters. Motivated by this, in this section, we examine more closely how the shape of the distribution of $[Eu/Fe]$ abundances in the ISM changes in response to shifts in the mass per event and the relative rate of the r-process events.

First, we consider changes in m_{rp} , keeping all other parameters fixed. Next, we consider changes in f_{rp} while keeping m_{rp} constant. Finally, we address how the statistics of variations of metal poor halo stars in chemical space can provide valuable constraints on m_{rp} and f_{rp} . Throughout this analysis, we focus on the results derived from the MW progenitor with high SFR model and the satellite galaxy model.

6.1. The role of m_{rp}

The key to using galaxy patch models productively is to isolate the role of key parameters and then to analyse the simulations so that we can learn the role of these model ingredients on metal mixing. In this analysis we first begin by isolating the role of m_{rp} .

Figure 9 shows the stacked one-dimensional distributions of $[Eu/Fe]$ within the cold, dense gas at each average $[Fe/H]$ metallicity. The color bar notes the fractional mass in each bin. The filled-in contours represent the standard enrichment model (i.e., $f_{rp} = 10^{-3}$ and $m_{rp} = 10^{-2} M_{\odot}$), while the line contours denote the model with m_{rp} increased by a factor of 10 (i.e., $m_{rp} = 10^{-1} M_{\odot}$). The left-hand panel shows our results from the MW progenitor with high SFR model, while the right-hand panel reveals our outcomes from the satellite galaxy model.

In both galaxy models, as expected, the shape of the contours is unchanged by altering m_{rp} . The main difference is an increase in the mean abundance of $[Eu/Fe]$, as the mass of r-process injected over time is augmented in the box. The metal dispersion, on the other hand, stays the same as the relative rate of metal mixing, which is controlled by the cc-SN rate, remains unchanged.

6.2. The role of f_{rp}

Our findings in Section 6.1 provide supporting evidence that while the average $[Eu/Fe]$ abundance can be altered by changes in m_{rp} , the dispersion of the $[Eu/Fe]$ abundance can only be modified by varying f_{rp} .

It is to this issue that we now turn our attention. Figure 10 shows how the stacked one-dimensional distributions of $[Eu/Fe]$ as a function of the average $[Fe/H]$ metallicity within the cold, dense gas are altered when f_{rp} is modified. This result should be directly compared with those presented in Figure 9. For both of the models considered in Figure 10, the relative rate of r-process event is changed from $f_{rp} = 10^{-3}$ to $f_{rp} = 10^{-2}$ while keeping all other inputs constant.

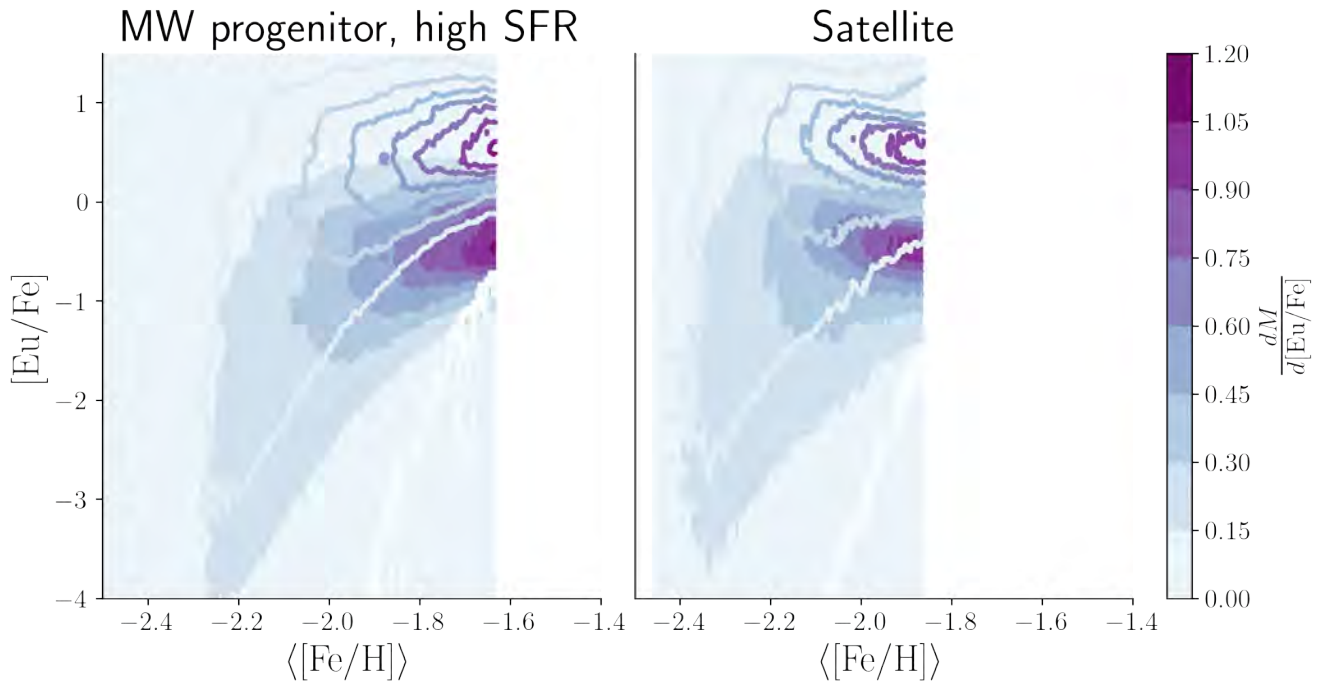


Figure 9. Stacked 1d distributions of [Eu/Fe] within the cold, dense gas at each average [Fe/H] metallicity. Contours show the fractional mass per bin in this abundance plane and the effects of altering the mass per event while keeping the relative rate ($f_{\text{rp}} = 10^{-3}$) constant. Filled in contours represent the simulations with $m_{\text{rp}} = 1 \times 10^{-2} M_{\odot}$, while line contours represent $m_{\text{rp}} = 1 \times 10^{-1} M_{\odot}$. Results are shown for two galaxy models: the MW progenitor high SFR model (left panel) and satellite galaxy model (right panel). Increasing the mass per event shifts the abundance distributions to higher mean [Eu/Fe] at constant mean [Fe/H], while the abundance spread, which is driven by turbulent mixing, remains unchanged.

Some conspicuous points should be underscored from Figure 10. First, it is important to note that the [Fe/H] abundance is determined solely by the cc-SNe, whose rate remains unchanged in all simulations. Thus, changes in f_{rp} lead simply to adding more r-process material, thereby increasing the mean [Eu/Fe] abundance but producing very little change in the overall Fe mass. Second, the relative injection rate, f_{rp} , alters both the evolution of the mean [Eu/Fe] abundance, as well as, the [Eu/Fe] spread. This is because the total amount of metals injected is significantly increased with time but at the expense of augmenting the number of injection sites and not the total mass per event as was done in Section 6.1. As such, the mean separation between injection sites is substantially decreased, which helps the effectiveness of turbulent mixing in smoothing metal inhomogeneities. As expected, this diminishes the [Eu/Fe] abundance spread. Finally, the mean [Eu/Fe] abundance increases more swiftly when f_{rp} is augmented, causing the model to spend more time at higher relative abundances in the plane depicted in Figure 10. By its very nature, a mass build up at higher relative abundances is naturally produced in these models.

Motivated by the results presented in Sections 6.1 and 6.2, we direct our efforts to comparing our models to observations

under the assumption that the selected cold gas within the disk is the most likely to form stars.

6.3. Constrains from observations of metal poor halo stars

Having considered the influence of m_{rp} and f_{rp} on the mean and spread of [Eu/Fe] as a function of the mean [Fe/H] abundance, we dedicate ourselves to comparing the simulated abundance distributions with the observed stellar abundances in the MW halo. We do this in order to provide useful constraints on the operating conditions of r-process production models in the early Universe.

The metal-poor halo stars for this analysis are taken from Roederer et al. (2014). Our selection has a twofold rationale. First, this data set constitutes the largest homogeneously reduced sample of its kind (about 300 metal-poor halo stars). And, second, the authors have systematically and scrupulously documented the uncertainty of their measurements. This allows us to use the star-to-star [Eu/Fe] scatter and mean as a function of [Fe/H] derived by Roederer et al. (2014) as a constraint for r-process production models in the $[m_{\text{rp}}, f_{\text{rp}}]$ plane.

In Figure 11, we show the distributions of [Eu/Fe] as a function of the average abundance of [Fe/H] within the cold, dense gas in the disk for both the MW progenitor with high SFR (left panel) and the satellite galaxy model (right panel).

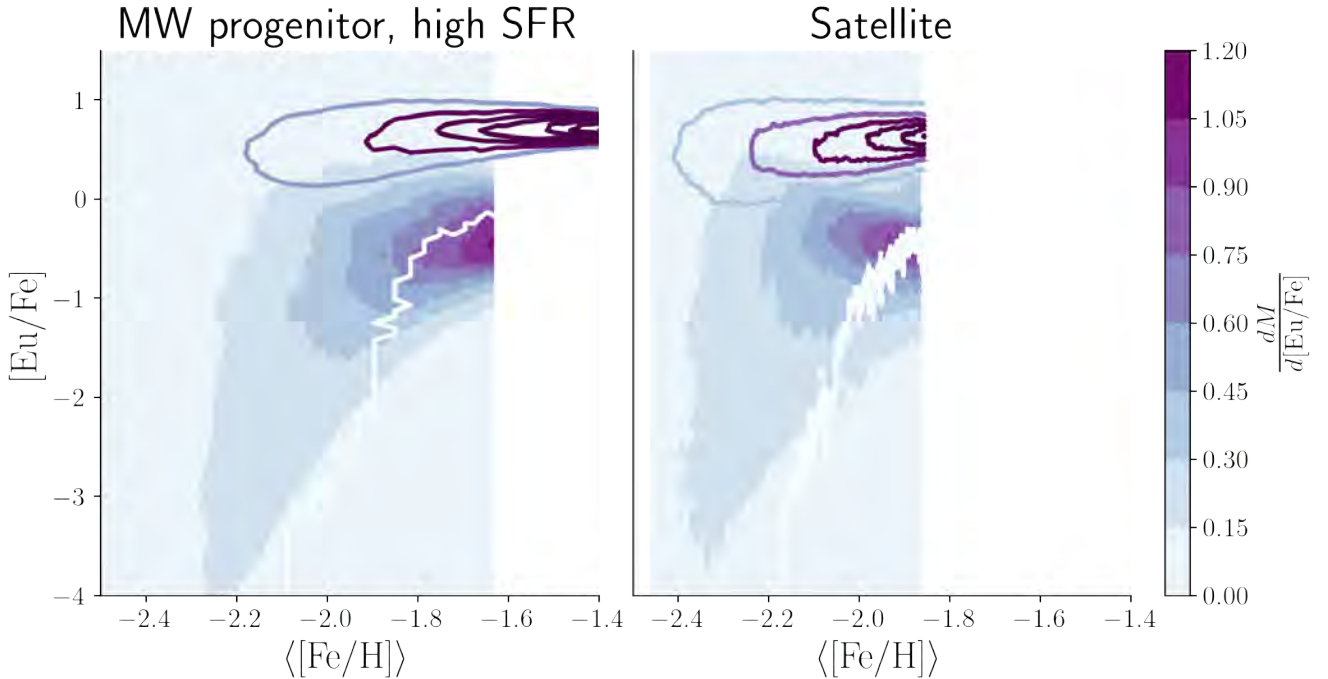


Figure 10. Stacked 1d distributions of [Eu/Fe] within the cold, dense gas at each average [Fe/H] metallicity. Results are shown for the same two galaxy models as in Figure 9. Color indicates the fractional mass per bin in this abundance plane. Filled in contours represent the simulations with $f_{\text{rp}} = 10^{-3}$, while line contours represent $f_{\text{rp}} = 10^{-2}$, in both cases $m_{\text{rp}} = 1 \times 10^{-2} M_{\odot}$. Changing the relative rate of events from $f_{\text{rp}} = 10^{-3}$ to $f_{\text{rp}} = 10^{-2}$ reduces the spread of abundances and leads to more cold, dense gas at higher [Eu/Fe] abundances.

The color indicates the fractional mass in a given bin. Also shown are the abundances and measurement uncertainties of the MW halo stars, as reported by Roederer et al. (2014). The parameters of the r-process events have been adjusted to achieve a reasonable agreement with the observations for both models. Shown is a representative model that effectively recovers both the mean and the spread in [Eu/Fe] as a function of [Fe/H] for the sample of MW halo stars that we selected. The representative values used to generate the models in Figure 11 are $f_{\text{rp}} = 10^{-2}$ and $m_{\text{rp}} = 5 \times 10^{-3} M_{\odot}$, respectively. Given that the MW progenitor with high SFR model retains the r-process products more effectively, the mean [Eu/Fe] is slightly more elevated compared to the satellite model, albeit within the uncertainties of the data and the range of applicability of the simulations (e.g., results are only shown after steady state is reached).

From the simple model comparison presented in Figure 11, we find clear evidence that the properties of the metal-poor halo stars are consistent with stellar birth sites in a MW progenitor with a high SFR or a satellite galaxy. It is, however, important to note that model comparison is hindered by the fact that the observational sample used in this analysis is impaired by incompleteness and selection effects, which are most evident at low [Eu/Fe] abundances.

7. DISCUSSION

Observations of [Eu/Fe] in metal-poor stars suggest relative yields and variations of yields in r-process production events. Such inherent fluctuations are evident when r-process events inject metals at rates that are significantly reduced when compared to cc-SN rates. These fluctuations are smoothed out by turbulent diffusion driven by cc-SNe, which sets the rate of metal mixing. As we have contended in this paper, the degree of fluctuations along with the mean abundances of [Eu/Fe] are sensitive to the relative mass injection rate of r-process and, to a lesser extent, to the type of galaxy environment.

7.1. Production rate of r-process elements

The total r-process mass in the MW is estimated to be $M_{\text{tot, rp}} \approx 2.3 \times 10^4 M_{\odot}$ (Hotokezaka et al. 2018). Combining this number with an estimate of the age of the MW ($t_{\text{MW}} \approx 1 \times 10^{10}$ yr), one can calculate an average production rate of r-process elements in the galaxy as

$$\dot{m}_{\text{rp}} \approx \frac{M_{\text{tot, rp}}}{t_{\text{MW}}} \approx 2.3 \times 10^{-6} M_{\odot}/\text{yr}. \quad (4)$$

Hotokezaka et al. (2018) used this relationship to estimate the mass production rate of r-process events in the MW as

$$R_{\text{MW}} \approx 230 / \text{Myr} \left(\frac{m_{\text{rp}}}{0.01 M_{\odot}} \right)^{-1}. \quad (5)$$

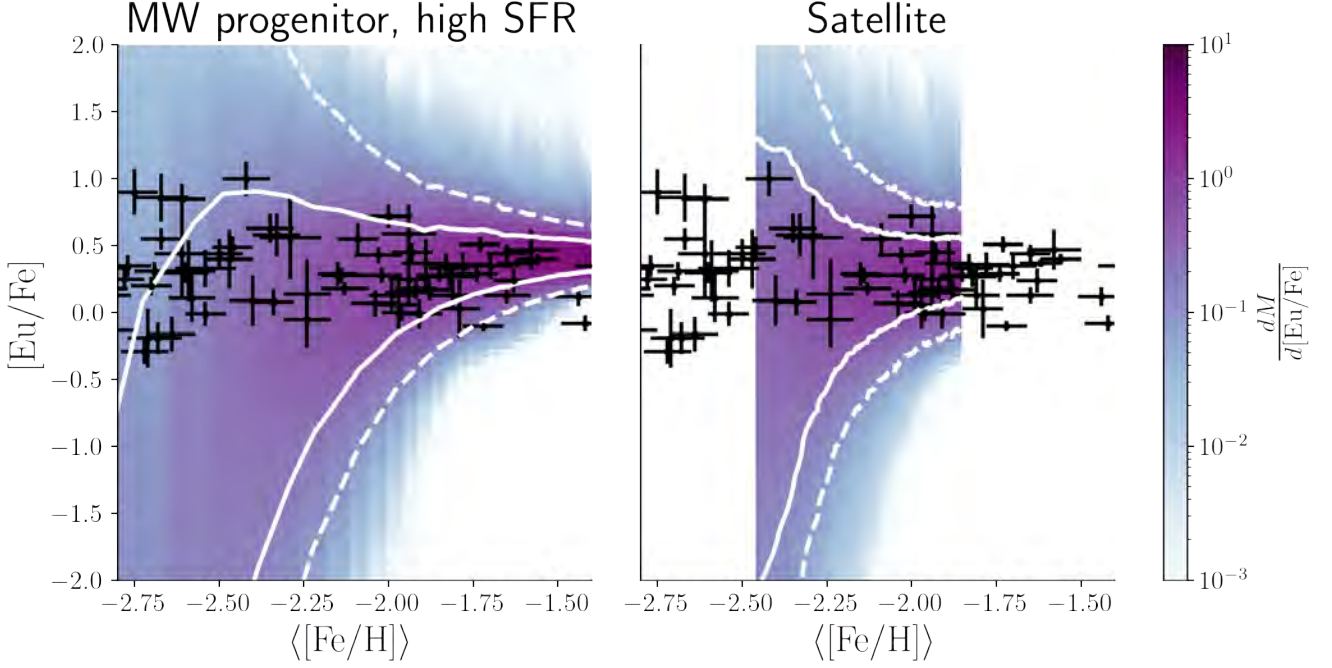


Figure 11. Stacked 1d distributions of $[\text{Eu}/\text{Fe}]$ in the cold, dense gas at each average $[\text{Fe}/\text{H}]$ metallicity in the MW progenitor with high SFR model (left panel) and satellite galaxy model (right panel). The color indicates the fractional mass in each bin, the white solid (dashed) lines indicate the 1σ (2σ) spread of the distribution. In both models, $f_{\text{rp}} = 10^{-2}$ and $m_{\text{rp}} = 5 \times 10^{-3} M_{\odot}$. We consider the cold, dense gas within the disk as the most likely to form stars. The black symbols indicate the abundances of metal poor halo stars with uncertainties as reported by Roederer et al. (2014). The mean $[\text{Eu}/\text{Fe}]$ abundance in high SFR model is slightly elevated when compared to the satellite galaxy model as expected from the ability of this model to more effectively retain r-process material.

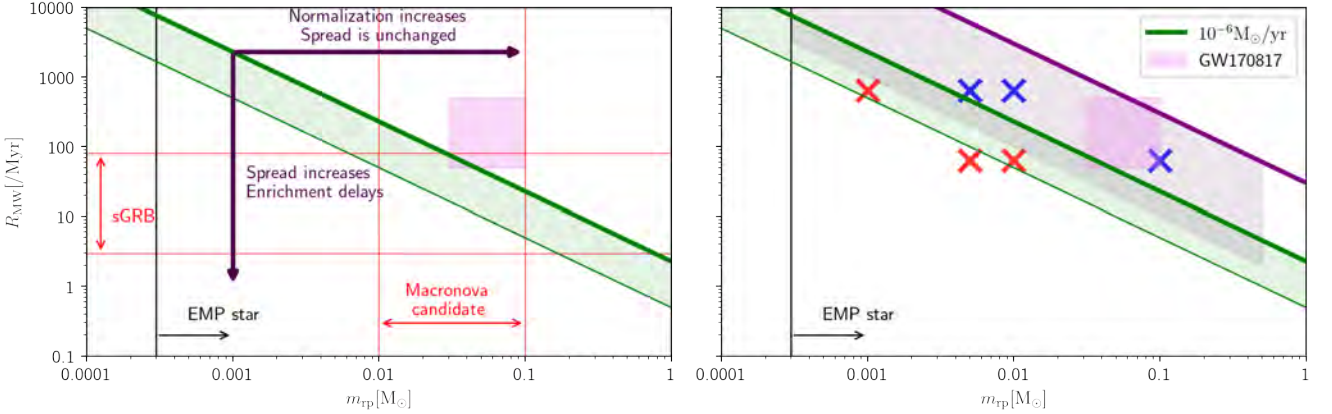


Figure 12. The constraints derived for r-process production events in the $[m_{\text{rp}}, R_{\text{MW}}]$ plane, which has been adapted from Hotokezaka et al. (2018). The left panel includes a compilation of the production rate of r-process element constraints in the MW: the constraints from GW170818, limits on rates from short gamma-ray burst observations, the mass limits from extremely metal-poor stars (Macias & Ramirez-Ruiz 2018), and the mass limits from macronova candidates. The derived relationships between the mean and spread of abundances when the rate or mass per event are altered are highlighted in the left panel. On the right-hand panel we show the constraints derived from turbulent mixing simulations. The red symbols indicate simulations that do not successfully explain the data while the blue symbols are for simulations that give a reasonable description of the $[\text{Eu}/\text{Fe}]$ abundances (see also Appendix C). The lavender shaded region highlights the parameter space for which simulations provide a reasonable description of the data. The upper limit for the mass production rate (purple line) arise naturally from the highest $[\text{Eu}/\text{Fe}]$ abundance measurement (see text). Models above this region are stringently ruled out given that there are very few selection effects against uncovering the highest $[\text{Eu}/\text{Fe}]$ metal poor stars.

This relationship is represented by the thick green line in Figure 12 along which the production rate of r-process elements is unchanged. The shaded region below the line is limited by the same relationship by for a lower total r-process mass in the MW. This relationship is set by $\dot{m}_{\text{rp}} \approx 1 \times 10^{-7} M_{\odot}/\text{yr}$, which is thought to give a strict lower limit to \dot{m}_{rp} based on the minimum amount of r-process mass in stars in the MW (Kasen et al. 2017; Hotokezaka et al. 2018).

The shaded-pink region in Figure 12 shows the range of values in the $[m_{\text{rp}}, R_{\text{MW}}]$ plane derived from observations of GW170817 (Kasen et al. 2017; Kilpatrick et al. 2017; Waxman et al. 2018; Hotokezaka et al. 2018). We also show in this plane the estimates of the rates of short gamma-ray bursts (R_{MW}), which are believed to be an observational signature of NSM (Eichler et al. 1989; Lee et al. 2005; Lee & Ramirez-Ruiz 2007) and the mass constraints (m_{rp}) from observations of afterglows of sGRBs (Roberts et al. 2011; Hotokezaka et al. 2013; Tanvir et al. 2013; Berger et al. 2013; Yang et al. 2015; Jin et al. 2016; Kasen et al. 2015; Kasliwal et al. 2017; Kilpatrick et al. 2017; Murguia-Berthier et al. 2017; Ascenzi et al. 2019), referred to in Figure 12 as macronova candidates. Finally, the vertical black line marks the lower limit on r-process mass per event as deduced by Macias & Ramirez-Ruiz (2018) based on observations of metal poor halo stars in the MW.

In the left panel of Figure 12 we call attention to the results from our turbulent mixing study, which explores how the abundance distribution of $[\text{Eu}/\text{Fe}]$ is altered by m_{rp} and f_{rp} (i.e., R_{MW}). As highlighted by the horizontal arrow, changing m_{rp} while keeping f_{rp} constant shifts the mean abundance at a fixed $[\text{Fe}/\text{H}]$ abundance but does not alter the scatter. This implies that the observed spread of abundances can not be used to constraint m_{rp} . In contrast, as underscored by the vertical arrow, f_{rp} changes both the spread and the mean of the $[\text{Eu}/\text{Fe}]$ abundance distributions at a fixed $[\text{Fe}/\text{H}]$ abundance.

The results of the galaxy patch simulations of the MW progenitor with high SFR model are shown in the right panel of Figure 12. To accurately position our simulations in the $[m_{\text{rp}}, R_{\text{MW}}]$ plane, we follow Beniamini et al. (2016) who estimates an average rate of cc-SNe in the MW to be

$$\tilde{n}_{\text{SNe,MW}} \approx 6.4 \times 10^4 \text{ Myr}^{-1}. \quad (6)$$

This allows us to chart the relative rate of r-process to cc-SN events from the local boxes to standard MW values by assuming constant relative rates across the galaxy. Then it follows that

$$R_{\text{MW, rp}} = f_{\text{rp}} \tilde{n}_{\text{SNe,MW}}. \quad (7)$$

We divide the simulations broadly into two distinct groups by how well they describe the observed abundances of MW halo stars (Roederer et al. 2014). We consider both the mean and the spread of $[\text{Eu}/\text{Fe}]$ abundance in bins of $[\text{Fe}/\text{H}]$, as well as, the range of $[\text{Fe}/\text{H}]$ abundance over which there is

rough agreement when making these comparisons. In Appendix C we present the results of the simulations with varying m_{rp} and f_{rp} and how they compare to observations. The blue symbols indicate reasonable agreement between observations and simulations, while the red symbols indicate little to no overlap between the abundances predicted by the simulations and those observed in the comparison sample.

Obviously, the comparison presented in Figure 12 is only cursory and should be taken as an order of magnitude estimate at present. Having said this, the results of our metal mixing study allow us to clearly define a model confidence region within the $[m_{\text{rp}}, R_{\text{MW}}]$ plane, which is specified by the lavender shaded region in the left panel. The lavender region is restrained by a strict upper limit (purple line). Such a limit can be derived by the underlying fact that simulations above this boundary will naturally produce stars with a mean abundance of $[\text{Eu}/\text{Fe}] = 1.4$, which is higher than the abundance of the most r-process enhanced star in the Roederer et al. (2014) sample: $[\text{Eu}/\text{Fe}] = 1.37$. The slope of the line is derived from the mass ratios of Eu and Fe production leading to $[\text{Eu}/\text{Fe}] = 1.4$. This value can be written as a production rate with $\dot{m}_{\text{rp,max}} \approx 4.7 \times 10^{-4} M_{\odot}/\text{yr}$. The lavender region presented in the left panel of Figure 12 is in remarkable good agreement with previous independent constraints derived both theoretically and empirically and provide a significant reduction in the permissible parameter space.

7.2. Co-production of light and heavy r-process elements?

Several astrophysical processes might be required to explain the solar r-process abundance pattern of both the lighter neutron capture elements (between the first and second r-process peaks at $A \approx 80$ and $A \approx 130$, respectively) and heavier nuclei such as Eu (Cowan et al. 2021). A fascinating characteristic that emerges when comparing the relative abundances of metal poor halo stars is the robustness of the pattern for elements with $A \geq 137$ (Snedden et al. 2008). In this study we have selected to model the r-process mass contribution as that comprised by all elements with $A \geq 69$. If, for example, we change the minimum atomic number from $A_{\text{min}} = 69$ to $A_{\text{min}} = 90$ the average abundances of $[\text{Eu}/\text{Fe}]$ shift by +0.68 dex with no other changes to the results presented in Figure 12. Appendix C includes the simulated distributions for m_{rp} calculated with and without this shifting (i.e., with $A_{\text{min}} = 69$ and $A_{\text{min}} = 90$). This simply implies that constraints on \dot{m}_{rp} are sensitive to whether r-process sites, which are assumed in this paper to be standard, are responsible for producing all r-process elements or only the heavier ones. If Eu is produced by sources that only produce heavier r-process elements ($A \geq 90$), this implies that the derived constraints on \dot{m}_{rp} should be lower by 0.68 dex when compared to those illustrated in Figure 12.

7.3. On the origin of the metal poor halo stars

The MW halo is expected to have been assembled from stars originally residing in disrupted satellites (e.g. Naidu et al. 2021; Santistevan et al. 2021). The presence of r-process enhanced stars (Beers & Christlieb 2005; Holmbeck et al. 2020) in several dwarf galaxy systems and the orbital properties of r-process enhanced stars in the halo (Roederer et al. 2018) indicate that such stars likely were accreted from disrupted satellites. From a theoretical perspective, Hirai et al. (2022) recently performed hydrodynamic zoom-in cosmological simulations, focusing on a MW-like galaxies. They found that the vast majority (90%) of r-process enhanced stars ($[\text{Eu}/\text{Fe}] > 0.7$) are formed early in the evolution of a galaxy and concluded that the majority of these r-process enhanced stars were accreted from disrupted satellite galaxies.

Our results support the hypothesis that both MW-like and dwarf-like galaxy systems are capable of producing stars with r-process abundances similar to those observed in the MW halo. It is, however, important to note that retention of r-process elements in satellite galaxies is found to be smaller than in MW-like progenitors (Section 4). This implies that viable mass production rates in satellite galaxies should be larger (by a factor of a few) than those presented in Figure 12 for a MW-like progenitor. Retention of r-process elements might also be significantly reduced for r-process events with large offsets from the star forming disk, such as expected for NSM with long delay times and large kick velocities. With that said, systems with large displacements are thought to be much less effective at polluting low metallicity gas with r-process material in the early Universe (e.g., Siegel et al. 2019).

8. SUMMARY AND CONCLUSIONS

In this paper we study the patchy enrichment of the ISM using numerical simulations at kpc scales that are able to resolve the mixing of metals by cc-SNe-driven turbulence. By investigating the statistics of variations of cc-SN and r-process products in these simulations, we are able to derive constraints on the allowed range of the production rate of r-process elements in the MW. By systematically varying the model parameters, we were able to identify some of the physical process that we believe are most relevant to explain the mean and dispersion of $[\text{Eu}/\text{Fe}]$ abundances in metal-poor stars. Our salient findings are:

- cc-SNe inject freshly synthesized metals and drive turbulent mixing which causes metals to diffuse across the disk (Figure 1). By virtue of their much more frequent injection, cc-SNe products (for example, Fe) are more evenly distributed than r-process elements (for example, Eu) synthesized in rarer events. This dif-

ference naturally produces an ISM with r-process elements that are nonuniform and highly undiluted at early epochs (Figure 2). These congenital variations are most notable when r-process sources inject metals at rates that are considerably decreased compared to cc-SN rates (Sections 3 and 4).

- The momentum and energy that goes into driving turbulence in the disk also launches galactic winds and flings metals out of the disk (Figure 4). The rarefied galactic wind is highly enriched in both Fe and Eu compared to the star forming gas in the disk (Figure 2). This result implies that a considerable mass of r-process elements might reside in the hot inter galactic medium (Sections 3 and 4).
- The metal mass loading factors of cc-SN and r-process products are not exactly the same, suggesting that r-process metals are launched by winds before they are able to be efficiently mixed with the ISM (Figure 2). However, models with fewer cc-SNe give r-process elements more time to diffuse and mix in the disk and, as a result, show winds with less prominent Eu-enriched outbursts (Sections 3 and 4).
- Across different galaxy models, the metal mass loading factors of iron and r-process elements are rather similar. However, the magnitude of the loading factors depend on the specific galaxy potential, with larger mass loading factors found in less massive galaxies (Figure 6). Implicitly, higher mass injection rates of r-process material are required in a satellite galaxy in order to achieve an average $[\text{Eu}/\text{H}]$ abundance comparable with a MW-like progenitor galaxy (Section 4).
- The r-process metal mass loading factor shows a measurable increase with increasing allowed height of r-process events (Figure 7). Despite this, the $[\text{Eu}/\text{Fe}]$ abundances, especially in the cold, dense gas phase, are found to be very similar across models (Figure 8). Thus, we conclude that no measurable changes in observed galaxy properties are expected for the range of offsets we are able to probe in these simulations (Section 5).
- The degree of fluctuations in and the mean of $[\text{Eu}/\text{Fe}]$ abundances in the cold, dense gas are found to be highly responsive to the mass injection rate of r-process (Section 6) and, to a lesser extent, to the type of galaxy (Section 4). Concretely, increasing the r-process mass per event increases the mean $[\text{Eu}/\text{Fe}]$ abundance (Figure 9), while increasing the rate of r-process events relative to cc-SNe increases the mean $[\text{Eu}/\text{Fe}]$ abundance and reduces the $[\text{Eu}/\text{Fe}]$ spread (Figure 10).

- Observations of [Eu/Fe] in metal-poor stars are used to derive constraints on the mass per event and the event rate of r-process sources (Section 7). The constraints presented are in notable agreement with other independently derived confinements and produce a marked reduction in the permitted parameter range (Figure 12).
- Our findings give credence to the idea that stars with r-process abundances similar to those observed in the MW halo can be manufactured by both MW-like and dwarf-like galaxy progenitors (Figure 11). Although we note that r-process mass retention in satellite galaxies is found to be smaller than in MW-like progenitors and, as such, the viable mass production rates should be appropriately higher (Section 6).

1 We thank C. Sakari, K. Ruiz-Rocha, A. Ji, D. Kasen, N.
 2 Imara and L. Kenoly for insightful discussions. This work
 3 made use of an HPC facility funded by a grant from VIL-
 4 LUM FONDEN (project number 16599). A.N.K. and E.R.-
 5 R. acknowledge support by the Heising-Simons Founda-
 6 tion, the Danish National Research Foundation (DNRF132)
 7 and NSF (AST-2206243, AST-1911206 and AST-1852393).
 8 PM gratefully acknowledges support from NASA grant 14-
 9 WPS14-0048. M.S.F gratefully acknowledges support pro-
 10 vided by NASA through Hubble Fellowship grant HST-HF2-
 11 51493.001-A awarded by the Space Telescope Science Insti-
 12 tute, which is operated by the Association of Universities for
 13 Research in Astronomy, In., for NASA, under the contract
 14 NAS 5-26555.

REFERENCES

- Abbott, B. P., Abbott, R., Abbott, T. D., et al. 2017, *ApJL*, 850, L40, doi: [10.3847/2041-8213/aa93fc](https://doi.org/10.3847/2041-8213/aa93fc)
- Ascenzi, S., Coughlin, M. W., Dietrich, T., et al. 2019, *MNRAS*, 486, 672, doi: [10.1093/mnras/stz891](https://doi.org/10.1093/mnras/stz891)
- Asplund, M., Grevesse, N., Sauval, A. J., & Scott, P. 2009, *Annu. Rev. Astron. Astrophys.*, 47, 481, doi: [10.1146/annurev.astro.46.060407.145222](https://doi.org/10.1146/annurev.astro.46.060407.145222)
- Beers, T. C., & Christlieb, N. 2005, *ARA&A*, 43, 531, doi: [10.1146/annurev.astro.42.053102.134057](https://doi.org/10.1146/annurev.astro.42.053102.134057)
- Behroozi, P. S., Ramirez-Ruiz, E., & Fryer, C. L. 2014, *ApJ*, 792, 123, doi: [10.1088/0004-637X/792/2/123](https://doi.org/10.1088/0004-637X/792/2/123)
- Beniamini, P., Hotokezaka, K., & Piran, T. 2016, *ApJ*, 832, 149, doi: [10.3847/0004-637X/832/2/149](https://doi.org/10.3847/0004-637X/832/2/149)
- Berger, E., Fong, W., & Chornock, R. 2013, *ApJL*, 774, L23, doi: [10.1088/2041-8205/774/2/L23](https://doi.org/10.1088/2041-8205/774/2/L23)
- Burbidge, E. M., Burbidge, G. R., Fowler, W. A., & Hoyle, F. 1957, *Reviews of Modern Physics*, 29, 547, doi: [10.1103/RevModPhys.29.547](https://doi.org/10.1103/RevModPhys.29.547)
- Cameron, A. G. W. 1957, *PASP*, 69, 201, doi: [10.1086/127051](https://doi.org/10.1086/127051)
- Cioffi, D. F., McKee, C. F., & Bertschinger, E. 1988, *ApJ*, 334, 252, doi: [10.1086/166834](https://doi.org/10.1086/166834)
- Côté, B., Eichler, M., Arcones, A., et al. 2019, *ApJ*, 875, 106, doi: [10.3847/1538-4357/ab10db](https://doi.org/10.3847/1538-4357/ab10db)
- Coulter, D. A., Foley, R. J., Kilpatrick, C. D., et al. 2017, *Science*, 358, 1556, doi: [10.1126/science.aap9811](https://doi.org/10.1126/science.aap9811)
- Cowan, J. J., & Sneden, C. 2006, *Nature*, 440, 1151, doi: [10.1038/nature04807](https://doi.org/10.1038/nature04807)
- Cowan, J. J., Sneden, C., Lawler, J. E., et al. 2021, *Reviews of Modern Physics*, 93, 015002, doi: [10.1103/RevModPhys.93.015002](https://doi.org/10.1103/RevModPhys.93.015002)
- Cowan, J. J., & Thielemann, F.-K. 2004, *Physics Today*, 57, 10.47, doi: [10.1063/1.1825268](https://doi.org/10.1063/1.1825268)

- Eichler, D., Livio, M., Piran, T., & Schramm, D. N. 1989, *Nature*, 340, 126, doi: [10.1038/340126a0](https://doi.org/10.1038/340126a0)
- Fielding, D., Quataert, E., Martizzi, D., & Faucher-Giguère, C.-A. 2017, *MNRAS*, 470, L39, doi: [10.1093/mnras/slx072](https://doi.org/10.1093/mnras/slx072)
- Fields, B. D., Truran, J. W., & Cowan, J. J. 2002, *ApJ*, 575, 845, doi: [10.1086/341331](https://doi.org/10.1086/341331)
- Haynes, C. J., & Kobayashi, C. 2019, *MNRAS*, 483, 5123, doi: [10.1093/mnras/sty3389](https://doi.org/10.1093/mnras/sty3389)
- Hirai, Y., Beers, T. C., Chiba, M., et al. 2022, *MNRAS*, 517, 4856, doi: [10.1093/mnras/stac2489](https://doi.org/10.1093/mnras/stac2489)
- Holmbeck, E. M., Hansen, T. T., Beers, T. C., et al. 2020, *ApJS*, 249, 30, doi: [10.3847/1538-4365/ab9c19](https://doi.org/10.3847/1538-4365/ab9c19)
- Hotokezaka, K., Beniamini, P., & Piran, T. 2018, *International Journal of Modern Physics D*, 27, 1842005, doi: [10.1142/S0218271818420051](https://doi.org/10.1142/S0218271818420051)
- Hotokezaka, K., Kyutoku, K., Tanaka, M., et al. 2013, *ApJL*, 778, L16, doi: [10.1088/2041-8205/778/1/L16](https://doi.org/10.1088/2041-8205/778/1/L16)
- Ji, A. P., Frebel, A., Chiti, A., & Simon, J. D. 2016a, *Nature*, 531, 610, doi: [10.1038/nature17425](https://doi.org/10.1038/nature17425)
- Ji, A. P., Frebel, A., Simon, J. D., & Chiti, A. 2016b, *ApJ*, 830, 93, doi: [10.3847/0004-637X/830/2/93](https://doi.org/10.3847/0004-637X/830/2/93)
- Ji, A. P., Simon, J. D., Roederer, I. U., et al. 2022, arXiv e-prints, arXiv:2207.03499. <https://arxiv.org/abs/2207.03499>
- Jin, Z.-P., Hotokezaka, K., Li, X., et al. 2016, *Nature Communications*, 7, 12898, doi: [10.1038/ncomms12898](https://doi.org/10.1038/ncomms12898)
- Karpov, P. I., Martizzi, D., Macias, P., et al. 2020, *ApJ*, 896, 66, doi: [10.3847/1538-4357/ab8f23](https://doi.org/10.3847/1538-4357/ab8f23)
- Kasen, D., Fernández, R., & Metzger, B. D. 2015, *MNRAS*, 450, 1777, doi: [10.1093/mnras/stv721](https://doi.org/10.1093/mnras/stv721)
- Kasen, D., Metzger, B., Barnes, J., Quataert, E., & Ramirez-Ruiz, E. 2017, *Nature*, 551, 80, doi: [10.1038/nature24453](https://doi.org/10.1038/nature24453)
- Kasliwal, M. M., Korobkin, O., Lau, R. M., Wollaeger, R., & Fryer, C. L. 2017, *ApJL*, 843, L34, doi: [10.3847/2041-8213/aa799d](https://doi.org/10.3847/2041-8213/aa799d)
- Kelley, L. Z., Ramirez-Ruiz, E., Zemp, M., Diemand, J., & Mandel, I. 2010, *ApJL*, 725, L91, doi: [10.1088/2041-8205/725/1/L91](https://doi.org/10.1088/2041-8205/725/1/L91)
- Kilpatrick, C. D., Foley, R. J., Kasen, D., et al. 2017, *Science*, 358, 1583, doi: [10.1126/science.aaq0073](https://doi.org/10.1126/science.aaq0073)
- Kolborg, A. N., Martizzi, D., Ramirez-Ruiz, E., et al. 2022, *ApJL*, 936, L26, doi: [10.3847/2041-8213/ac8c98](https://doi.org/10.3847/2041-8213/ac8c98)
- Kuijken, K., & Gilmore, G. 1989, *MNRAS*, 239, 605, doi: [10.1093/mnras/239.2.605](https://doi.org/10.1093/mnras/239.2.605)
- Lee, W. H., & Ramirez-Ruiz, E. 2007, *New Journal of Physics*, 9, 17, doi: [10.1088/1367-2630/9/1/017](https://doi.org/10.1088/1367-2630/9/1/017)
- Lee, W. H., Ramirez-Ruiz, E., & Granot, J. 2005, *ApJL*, 630, L165, doi: [10.1086/496882](https://doi.org/10.1086/496882)
- Li, M., & Bryan, G. L. 2020, *ApJL*, 890, L30, doi: [10.3847/2041-8213/ab7304](https://doi.org/10.3847/2041-8213/ab7304)
- Macias, P., & Ramirez-Ruiz, E. 2018, *ApJ*, 860, 89, doi: [10.3847/1538-4357/aac3e0](https://doi.org/10.3847/1538-4357/aac3e0)
- . 2019, *ApJL*, 877, L24, doi: [10.3847/2041-8213/ab2049](https://doi.org/10.3847/2041-8213/ab2049)
- Martizzi, D., Faucher-Giguère, C.-A., & Quataert, E. 2015, *MNRAS*, 450, 504, doi: [10.1093/mnras/stv562](https://doi.org/10.1093/mnras/stv562)
- Martizzi, D., Fielding, D., Faucher-Giguère, C.-A., & Quataert, E. 2016, *MNRAS*, 459, 2311, doi: [10.1093/mnras/stw745](https://doi.org/10.1093/mnras/stw745)
- McWilliam, A., Preston, G. W., Sneden, C., & Searle, L. 1995, *AJ*, 109, 2757, doi: [10.1086/117486](https://doi.org/10.1086/117486)
- Metzger, B. D., Martínez-Pinedo, G., Darbha, S., et al. 2010, *MNRAS*, 406, 2650, doi: [10.1111/j.1365-2966.2010.16864.x](https://doi.org/10.1111/j.1365-2966.2010.16864.x)
- Montes, G., Ramirez-Ruiz, E., Naiman, J., Shen, S., & Lee, W. H. 2016, *ApJ*, 830, 12, doi: [10.3847/0004-637X/830/1/12](https://doi.org/10.3847/0004-637X/830/1/12)
- Mösta, P., Roberts, L. F., Halevi, G., et al. 2018, *ApJ*, 864, 171, doi: [10.3847/1538-4357/aad6ec](https://doi.org/10.3847/1538-4357/aad6ec)
- Murguia-Berthier, A., Ramirez-Ruiz, E., Kilpatrick, C. D., et al. 2017, *ApJL*, 848, L34, doi: [10.3847/2041-8213/aa91b3](https://doi.org/10.3847/2041-8213/aa91b3)
- Naidu, R. P., Conroy, C., Bonaca, A., et al. 2021, *ApJ*, 923, 92, doi: [10.3847/1538-4357/ac2d2d](https://doi.org/10.3847/1538-4357/ac2d2d)
- Naiman, J. P., Pillepich, A., Springel, V., et al. 2018, *MNRAS*, 477, 1206, doi: [10.1093/mnras/sty618](https://doi.org/10.1093/mnras/sty618)
- Nishimura, N., Takiwaki, T., & Thielemann, F.-K. 2015, *ApJ*, 810, 109, doi: [10.1088/0004-637X/810/2/109](https://doi.org/10.1088/0004-637X/810/2/109)
- Ramirez-Ruiz, E., & MacFadyen, A. I. 2010, *ApJ*, 716, 1028, doi: [10.1088/0004-637X/716/2/1028](https://doi.org/10.1088/0004-637X/716/2/1028)
- Ramirez-Ruiz, E., Trenti, M., MacLeod, M., et al. 2015, *ApJL*, 802, L22, doi: [10.1088/2041-8205/802/2/L22](https://doi.org/10.1088/2041-8205/802/2/L22)
- Roberts, L. F., Kasen, D., Lee, W. H., & Ramirez-Ruiz, E. 2011, *ApJL*, 736, L21, doi: [10.1088/2041-8205/736/1/L21](https://doi.org/10.1088/2041-8205/736/1/L21)
- Roederer, I. U., Hattori, K., & Valluri, M. 2018, *AJ*, 156, 179, doi: [10.3847/1538-3881/aadd9c](https://doi.org/10.3847/1538-3881/aadd9c)
- Roederer, I. U., Preston, G. W., Thompson, I. B., Shectman, S. A., & Sneden, C. 2014, *ApJ*, 784, 158, doi: [10.1088/0004-637X/784/2/158](https://doi.org/10.1088/0004-637X/784/2/158)
- Roederer, I. U., Mateo, M., Bailey, John I., I., et al. 2016, *AJ*, 151, 82, doi: [10.3847/0004-6256/151/3/82](https://doi.org/10.3847/0004-6256/151/3/82)
- Rosswog, S., & Ramirez-Ruiz, E. 2002, *MNRAS*, 336, L7, doi: [10.1046/j.1365-8711.2002.05898.x](https://doi.org/10.1046/j.1365-8711.2002.05898.x)
- Rosswog, S., Ramirez-Ruiz, E., & Davies, M. B. 2003, *MNRAS*, 345, 1077, doi: [10.1046/j.1365-2966.2003.07032.x](https://doi.org/10.1046/j.1365-2966.2003.07032.x)
- Safarzadeh, M., Ramirez-Ruiz, E., Andrews, J. J., et al. 2019, *ApJ*, 872, 105, doi: [10.3847/1538-4357/aaf0e](https://doi.org/10.3847/1538-4357/aaf0e)
- Santistevan, I. B., Wetzel, A., Sanderson, R. E., et al. 2021, *MNRAS*, 505, 921, doi: [10.1093/mnras/stab1345](https://doi.org/10.1093/mnras/stab1345)
- Shen, S., Cooke, R. J., Ramirez-Ruiz, E., et al. 2015, *ApJ*, 807, 115, doi: [10.1088/0004-637X/807/2/115](https://doi.org/10.1088/0004-637X/807/2/115)
- Siegel, D. M., Barnes, J., & Metzger, B. D. 2019, *Nature*, 569, 241, doi: [10.1038/s41586-019-1136-0](https://doi.org/10.1038/s41586-019-1136-0)
- Sneden, C., Cowan, J. J., & Gallino, R. 2008, *ARA&A*, 46, 241, doi: [10.1146/annurev.astro.46.060407.145207](https://doi.org/10.1146/annurev.astro.46.060407.145207)
- Sneden, C., Cowan, J. J., Lawler, J. E., et al. 2003, *ApJ*, 591, 936, doi: [10.1086/375491](https://doi.org/10.1086/375491)

- Tanvir, N. R., Levan, A. J., Fruchter, A. S., et al. 2013, *Nature*, 500, 547, doi: [10.1038/nature12505](https://doi.org/10.1038/nature12505)
- Teyssier, R. 2002, *A&A*, 385, 337, doi: [10.1051/0004-6361:20011817](https://doi.org/10.1051/0004-6361:20011817)
- Thielemann, F. K., Eichler, M., Panov, I. V., & Wehmeyer, B. 2017, *Annual Review of Nuclear and Particle Science*, 67, 253, doi: [10.1146/annurev-nucl-101916-123246](https://doi.org/10.1146/annurev-nucl-101916-123246)
- Thornton, K., Gaudlitz, M., Janka, H. T., & Steinmetz, M. 1998, *ApJ*, 500, 95, doi: [10.1086/305704](https://doi.org/10.1086/305704)
- van de Voort, F., Pakmor, R., Bieri, R., & Grand, R. J. J. 2022, *MNRAS*, 512, 5258, doi: [10.1093/mnras/stac710](https://doi.org/10.1093/mnras/stac710)
- van de Voort, F., Pakmor, R., Grand, R. J. J., et al. 2020, *MNRAS*, 494, 4867, doi: [10.1093/mnras/staa754](https://doi.org/10.1093/mnras/staa754)
- van de Voort, F., Quataert, E., Hopkins, P. F., Kereš, D., & Faucher-Giguère, C.-A. 2015, *MNRAS*, 447, 140, doi: [10.1093/mnras/stu2404](https://doi.org/10.1093/mnras/stu2404)
- Wanajo, S., Hirai, Y., & Prantzos, N. 2021, *MNRAS*, 505, 5862, doi: [10.1093/mnras/stab1655](https://doi.org/10.1093/mnras/stab1655)
- Wang, Y., Nadler, E. O., Mao, Y.-Y., et al. 2021, *ApJ*, 915, 116, doi: [10.3847/1538-4357/ac024a](https://doi.org/10.3847/1538-4357/ac024a)
- Wasserburg, G. J., & Qian, Y. Z. 2000, *ApJL*, 529, L21, doi: [10.1086/312455](https://doi.org/10.1086/312455)
- Watson, D., Hansen, C. J., Selsing, J., et al. 2019, *Nature*, 574, 497, doi: [10.1038/s41586-019-1676-3](https://doi.org/10.1038/s41586-019-1676-3)
- Waxman, E., Ofek, E. O., Kushnir, D., & Gal-Yam, A. 2018, *MNRAS*, 481, 3423, doi: [10.1093/mnras/sty2441](https://doi.org/10.1093/mnras/sty2441)
- Winteler, C., Käppeli, R., Perego, A., et al. 2012, *ApJL*, 750, L22, doi: [10.1088/2041-8205/750/1/L22](https://doi.org/10.1088/2041-8205/750/1/L22)
- Yang, B., Jin, Z.-P., Li, X., et al. 2015, *Nature Communications*, 6, 7323, doi: [10.1038/ncomms8323](https://doi.org/10.1038/ncomms8323)
- Zevin, M., Nugent, A. E., Adhikari, S., et al. 2022, *ApJL*, 940, L18, doi: [10.3847/2041-8213/ac91cd](https://doi.org/10.3847/2041-8213/ac91cd)
- Zheng, Z., & Ramirez-Ruiz, E. 2007, *ApJ*, 665, 1220, doi: [10.1086/519544](https://doi.org/10.1086/519544)

APPENDIX

A. MASS AND VOLUME WEIGHTED DISTRIBUTIONS

In Section 3.2 we discussed the evolution of the volume weighted mean and spread of $[\text{Fe}/\text{H}]$, $[\text{Eu}/\text{H}]$ and $[\text{Eu}/\text{Fe}]$ in all the gas in the simulation volume, as well as, in the cold, dense gas in the disk. We showed that the global mean abundances are always higher than those of the cold, dense gas, and we argued that this is due to the larger volume filling factor of the gas in the wind region. We present here data to support this claim.

In the top row of Figure 13 we reproduce Figure 3, adding vertical lines to indicate three specific times in the simulation. These times are selected to more closely examine the structures of the volume and mass weighted abundance distributions. The subsequent three rows in the figure correspond to each of these time slices. In these rows the solid lines outline the volume weighted distributions (the color of the lines are the same as in the top row with darker color indicating cold, dense, disk gas while lighter color refers to the global gas values). We also note the mean value of these abundances with an arrow. The dashed lines show the equivalent distributions but weighted by gas mass rather than volume.

We first investigate the $[\text{Fe}/\text{H}]$ distributions. The volume weighted distribution of all the gas shows a sharp peak at relatively high abundances, where the mean of the distribution lies. Furthermore, this distribution has a long tail on the lower abundance side, at all time slices considered. The volume weighted distribution of the cold, dense gas is much more symmetric and peaks at lower metallicity values. Thus, there are considerable differences between the two distributions when considering the volume weighted distributions. However, the mass weighted distributions are rather similar (dashed lines in Figure 13). Hence, we conclude that the difference in mean abundance between the global and the cold, dense gas is driven by the higher abundance of the hot, diffuse gas in the disk winds being emphasized in the volume weighted distributions of the global gas.

We now turn our attention to the $[\text{Eu}/\text{X}]$ distributions and see many similar behaviors as seen in the $[\text{Fe}/\text{H}]$ distributions. First, the volume weighted distribution of the global gas abundance is off-set at high metallicity when compared to all other distributions. Second, there is a nearly perfect overlap between the volume weighted distribution of the cold, dense gas and the mass weighted distributions of both the global and the cold, dense gas phases. Finally, the volume weighted global distribution features a tail at the low enrichment side. The distributions $[\text{Eu}/\text{X}]$ are generally much broader than those of $[\text{Fe}/\text{H}]$ indicating that the r-process elements are less well mixed in all gas phases than Fe is. As time increases in the simulation the offset between the mean of the global and the cold, dense disk gas slowly decreases. This is caused by gas mixing in the ISM.

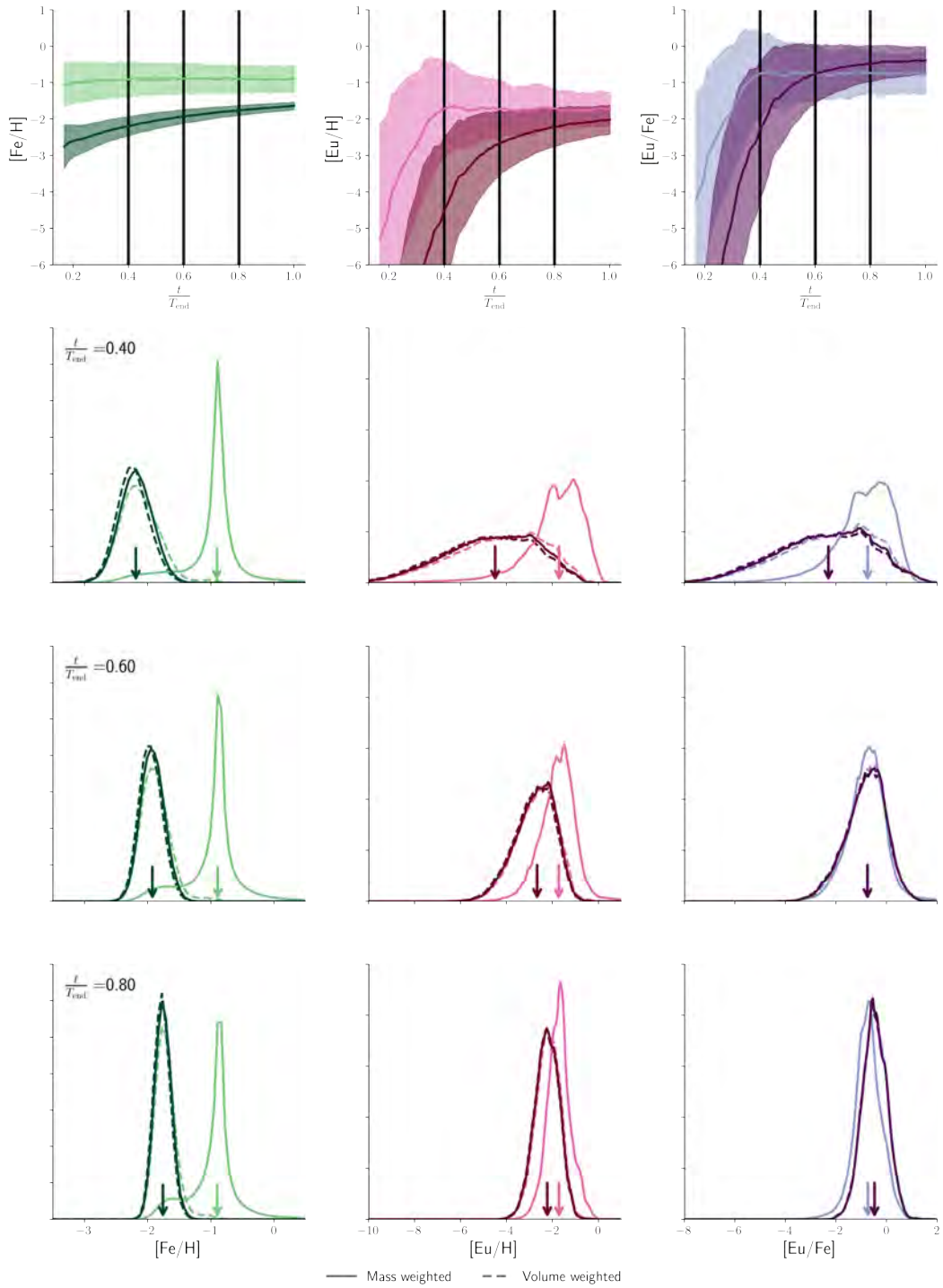


Figure 13. The abundance distributions at three distinct times in the metal mixing evolution of the MW progenitor with high SFR simulation. The top row is the same as Figure 3. The subsequent three rows show the distributions of $[\text{Fe}/\text{H}]$, $[\text{Eu}/\text{H}]$ and $[\text{Eu}/\text{Fe}]$ at each of the three times indicated by vertical, black lines in the top row. The colors indicate the gas phase; lighter color for global values and darker for cold, dense disk gas. The solid lines show the volume weighted distributions while the dashed lines give the mass weighted distributions. The arrows show the mean value of the volume weighted distributions.

B. LOADING IN ALL GALAXY POTENTIALS

In Section 4 we presented the loading factors of the total, iron and r-process mass in three galaxy potentials but we limited our attention to results for $|z| = 2z_{\text{SNe}}$. For completeness we present here the results for these loading factors at varying heights. In the middle row of Figure 14 we present an expanded version of Figure 6. The top and bottom rows of the figure show the same corresponding loading factors at $|z| = 3z_{\text{eff}}$ and $|z| = \frac{l}{2} - dx$, respectively. Across all galaxy potentials, the loading factors are larger when measured closest to the disk and decrease as we approach the edge of the box. This effect is caused (partly) by circulation of material in the wind whereby some of the ejected material falls back. The drop in loading factor is strongest in the MW progenitor with high SFR and smallest in the satellite galaxy model indicating that material is more efficiently launched when residing in a weaker galaxy potential.

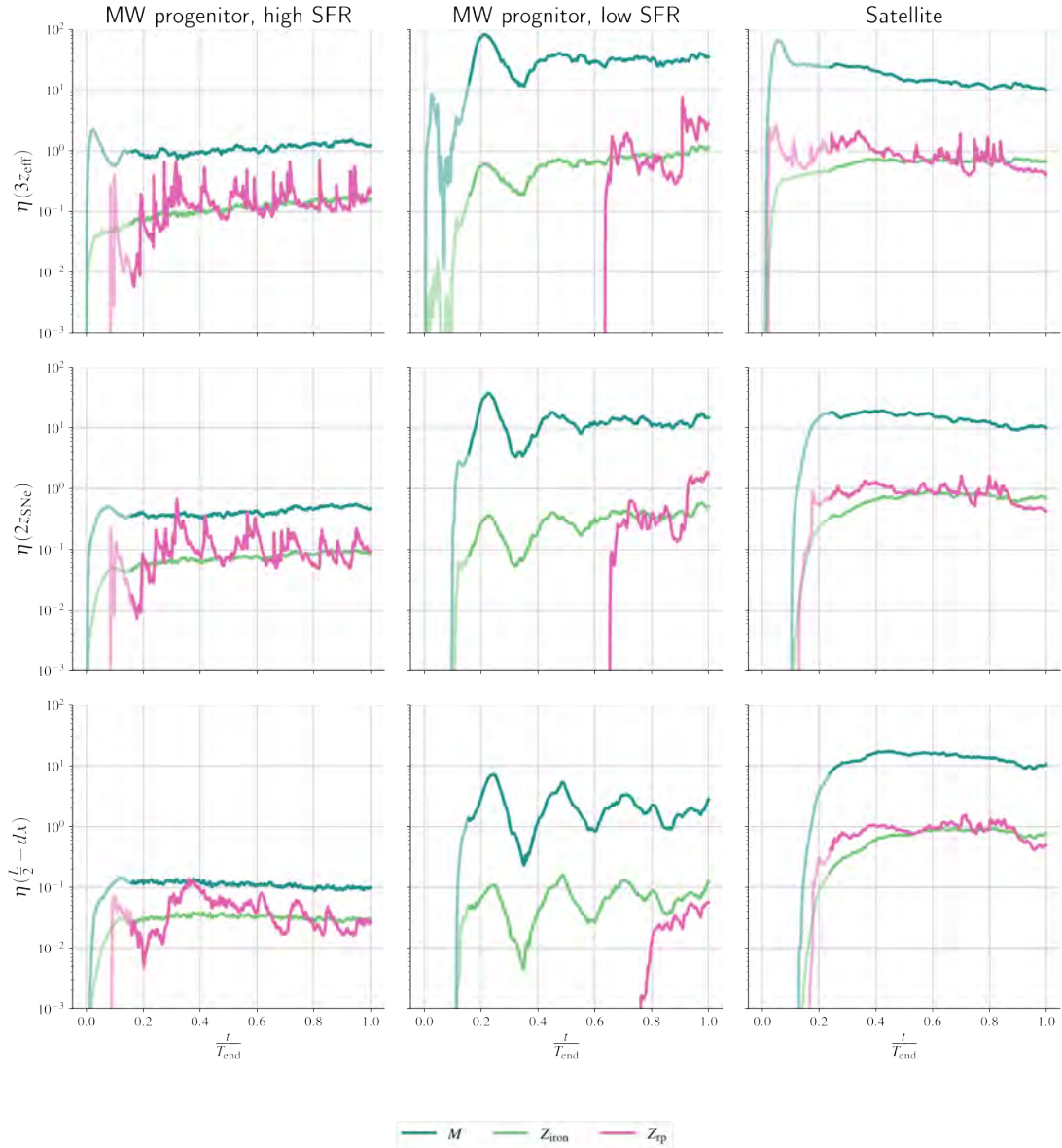


Figure 14. Loading factors for the total, iron and r-process mass (see legend) in each of the three galaxy patch models: MW progenitor with high SFR (left hand column), MW progenitor with low SFR (middle column) and satellite galaxy model (right hand column). Each row corresponds to mass outflow at increasing distance from the disk mid-plane: $3z_{\text{eff}}$ (top row), $2z_{\text{SNe}}$ (middle row) and $\frac{l}{2} - dx$ (bottom row). The middle row of this Figure is equivalent to Figure 6 although it has been extended to a slightly lower η values.

C. R-PROCESS PRODUCTION RATE IN THE MILKY WAY

We expand here on the presentation of our results in Sections 6.3, 7.1 and 7.2, and show how the abundances derived from various simulations compare with observations. Figure 15 shows the 50% and 90% contours of the distributions of [Eu/Fe] abundance as a function of the median [Fe/H] abundance of the cold, dense, disk gas. In the left (right) hand column we present the results when taking $A = 69$ ($A = 90$) as a lower limit for r-process elements. The r-process mass per event increases with each row, while the relative rate of r-process events is indicated by the color (see legend). We also include the 50% and 90% widths of the corresponding abundances of the metal-poor halo stars (Roederer et al. 2014), which are calculated in 0.23 dex wide [Fe/H] bins.

In Section 6.3 we showed the comparison between the best fitting r-process parameters and the observations. In Figure 15 we show how models with other parameter combinations fit the data. When choosing the best fit we take into account how well the simulations reproduce the mean of the observations, as well as, the abundance spread. This is done only for the range of metallicity over which the model is in steady state. We strongly disfavor models that predict a large number of stars with greater [Eu/Fe] abundances than those observed.

In Section 7.2 we discussed the dependence on the constraints of \dot{m}_{rp} on the assumed range of r-process elements. Figure 15 shows how the distributions of [Eu/Fe] change as a function of the average [Fe/H] when we change A_{min} . When an r-process pattern that includes only the heavy r-process elements ($A_{\text{min}} = 90$) is assumed, the relative mass of Eu to all the r-process elements increases and thus, the distribution of [Eu/Fe] shifts by +0.68 dex.

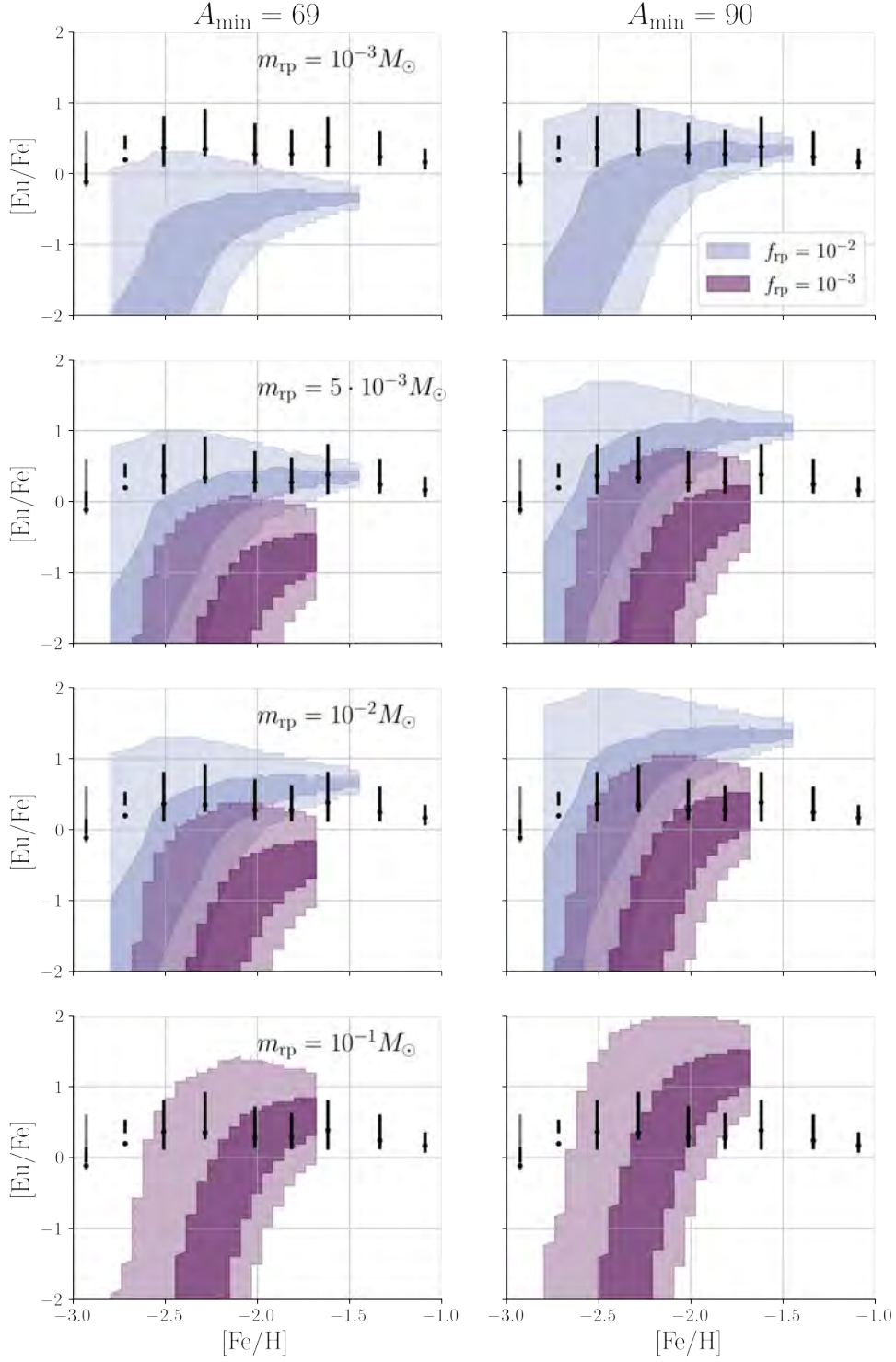


Figure 15. The simulated 50% and 90 % contours of the abundance distribution in the MW progenitor with high SFR when m_{rp} and f_{rp} are altered. The black and gray bars indicate the 50% and 90% spreads of the metal-poor MW halo stars (Roederer et al. 2014) in bins of $[\text{Fe}/\text{H}]$. The left hand columns use the Eu mass fraction to all r-process elements, while the right hand uses the fraction relative only to the heavy r-process elements (defined here as $A > 90$).

CONCLUSIONS & OUTLOOK

The aim of this thesis has been to study SNe-driven mixing process in the ISM with the goal of understanding metal enrichment, especially of r-process elements. Using small box fluid dynamic simulations of patches of galactic disks we have been able to resolve the dynamics of SNR and isolate the feedback driven mixing mechanisms on parsec scales.

The main findings of this work and contributions to the research field of galactic chemical evolution are:

We show that the SFR of a galaxy patch is directly imprinted on the dispersion of cc-SNe products (e.g. α -elements) in the gas. Higher SFR leads to greater dispersion because: i) metals are injected faster than they are able to mix. and, ii) high SFR requires high gas densities which hinders efficient mixing. The observed α -element spread of the MW halo stars is consistent with an accretion origin for those stars.

When comparing two metals from different sources (e.g. Fe and Eu) a higher relative rate of injection (more similar source rates) leads to smaller spreads in abundance.

Metal mass per event (which is still debated for sources of r-process production) has little to no impact on the shape of the abundance distribution. However, spread of r-process abundances in metal poor stars combined with mixing studies, such as those

done in this work, can be used to derive constraints on the total production rate of r-process elements. Using this method we have derived new constraints on the production rate of r-process elements in the MW. These new constraints are consistent with previous, independent estimates of the rate and constitute a considerable reduction in the allowed parameter space for the production rate.

We have used the galaxy patch simulations to study the mass loading factors of galactic winds and find that the loading factors of metals from cc-SNe and NSM-like sources are very similar to each other. This suggests that r-process elements are carried out of the galaxy by SNe driven dynamics and the NSM events have little impact on this process. This result also predicts the presence of significant masses of r-process elements in the hot IGM, a result which may be observationally testable in the future.

Finally, smaller galaxy systems are found to have higher over all loading factors, consistent with observations of mass outflow from e.g. dwarf galaxy systems. This result, in combination with the measured loading factors of r-process elements in these systems suggests that smaller galaxies may require higher masses of r-process enrichment to reach similar mean abundances of e.g. $[\text{Eu}/\text{Fe}]$ as MW-like galaxy systems.

BIBLIOGRAPHY

- Abbott, B. P., Abbott, R., Abbott, T. D., Acernese, F., Ackley, K., Adams, C., Adams, T., Addesso, P., Adhikari, R. X., Adya, V. B., Affeldt, C., Afrough, M., Agarwal, B., Agathos, M., Agatsuma, K., Aggarwal, N., Aguiar, O. D., Aiello, L., Ain, A., ... Virgo Collaboration. (2017). On the Progenitor of Binary Neutron Star Merger GW170817. *ApJ*, 850(2), Article L40, L40. <https://doi.org/10.3847/2041-8213/aa93fc>
- Abohalima, A., & Frebel, A. (2018). JINAbase—A Database for Chemical Abundances of Metal-poor Stars. *ApJS*, 238(2), Article 36, 36. <https://doi.org/10.3847/1538-4365/aadfe9>
- Argast, D., Samland, M., Thielemann, F. .-, & Qian, Y. .-. (2004). Neutron star mergers versus core-collapse supernovae as dominant r-process sites in the early Galaxy. *A&A*, 416, 997–1011. <https://doi.org/10.1051/0004-6361:20034265>
- Argast, D., & Samland, M. (2004). Constraints on the Astrophysical Nature of r-Process Nucleosynthesis Sites from Inhomogeneous Chemical Evolution Models. *PASA*, 21(2), 161–166. <https://doi.org/10.1071/AS04021>
- Armillotta, L., Krumholz, M. R., & Fujimoto, Y. (2018). Mixing of metals during star cluster formation: statistics and implications for chemical tagging. *MNRAS*, 481(4), 5000–5013. <https://doi.org/10.1093/mnras/sty2625>
- Arnone, E., Ryan, S. G., Argast, D., Norris, J. E., & Beers, T. C. (2005). Mg abundances in metal-poor halo stars as a tracer of early Galactic mixing. *A&A*, 430, 507–522. <https://doi.org/10.1051/0004-6361:20041034>
- Barklem, P. S., Christlieb, N., Beers, T. C., Hill, V., Bessell, M. S., Holmberg, J., Marsteller, B., Rossi, S., Zickgraf, F. .-, & Reimers, D. (2005). The Hamburg/ESO R-process

- enhanced star survey (HERES). II. Spectroscopic analysis of the survey sample. *A&A*, 439(1), 129–151. <https://doi.org/10.1051/0004-6361:20052967>
- Bartos, I., & Márka, S. (2019). Early Solar System r-process Abundances Limit Collapsar Origin. *ApJ*, 881(1), Article L4, L4. <https://doi.org/10.3847/2041-8213/ab3215>
- Beniamini, P., Hotokezaka, K., & Piran, T. (2016). r-process Production Sites as Inferred from Eu Abundances in Dwarf Galaxies. *ApJ*, 832(2), Article 149, 149. <https://doi.org/10.3847/0004-637X/832/2/149>
- Beniamini, P., & Piran, T. (2019). The Gravitational waves merger time distribution of binary neutron star systems. *MNRAS*, 487(4), 4847–4854. <https://doi.org/10.1093/mnras/stz1589>
- Bullock, J. S., Kravtsov, A. V., & Weinberg, D. H. (2001). Hierarchical Galaxy Formation and Substructure in the Galaxy's Stellar Halo. *ApJ*, 548(1), 33–46. <https://doi.org/10.1086/318681>
- Semi-analytic modelling of DM halo accretion of satellite galaxies by a MW sized host halo. They use RR Lyrae stars as standard candles and produced observational predictions for SDSS. Within the framework of their model they find support for the stellar halo of the MW consisting entirely of stars from disrupted dwarf galaxies. This work seems to lay the groundwork for Johnston et al 2018
- Burbidge, E. M., Burbidge, G. R., Fowler, W. A., & Hoyle, F. (1957). Synthesis of the Elements in Stars. *Reviews of Modern Physics*, 29(4), 547–650. <https://doi.org/10.1103/RevModPhys.29.547>
- Cameron, A. (1957). Nuclear Reactions in stars and nucleogenesis. *Publications of the Astronomical Society of the Pacific*, 69(408).
- Cayrel, R., Depagne, E., Spite, M., Hill, V., Spite, F., François, P., Plez, B., Beers, T., Primas, F., Andersen, J., Barbuy, B., Bonifacio, P., Molaro, P., & Nordström, B. (2004). First stars V - Abundance patterns from C to Zn and supernova yields in the early Galaxy. *A&A*, 416, 1117–1138. <https://doi.org/10.1051/0004-6361:20034074>
- Cescutti, G., François, P., Matteucci, F., Cayrel, R., & Spite, M. (2006). The chemical evolution of barium and europium in the Milky Way. *A&A*, 448(2), 557–569. <https://doi.org/10.1051/0004-6361:20053622>

- Chevalier, R. A. (1977). The Interaction of Supernovae with the Interstellar Medium. *Annual Review of Astronomy and Astrophysics*, 15(1), 175–196. <https://doi.org/10.1146/annurev.aa.15.090177.001135>
- Chiappini, C., Matteucci, F., & Romano, D. (2001). Abundance Gradients and the Formation of the Milky Way. *ApJ*, 554(2), 1044–1058. <https://doi.org/10.1086/321427>
- Cioffi, D. F., Mckee, C. F., & Bertschinger, E. (1988). Dynamics of Radiative Supernova Remnants. *The Astrophysical Journal*, 334(100), 252–265.
- Côté, B., Belczynski, K., Fryer, C. L., Ritter, C., Paul, A., Wehmeyer, B., & O’Shea, B. W. (2017). Advanced LIGO Constraints on Neutron Star Mergers and r-process Sites. *ApJ*, 836(2), Article 230, 230. <https://doi.org/10.3847/1538-4357/aa5c8d>
- Côté, B., Eichler, M., Arcones, A., Hansen, C. J., Simonetti, P., Frebel, A., Fryer, C. L., Pignatari, M., Reichert, M., Belczynski, K., & Matteucci, F. (2019). Neutron Star Mergers Might Not Be the Only Source of r-process Elements in the Milky Way. *ApJ*, 875(2), Article 106, 106. <https://doi.org/10.3847/1538-4357/ab10db>
- Côté, B., Fryer, C. L., Belczynski, K., Korobkin, O., Chruślińska, M., Vassh, N., Mumpower, M. R., Lippuner, J., Sprouse, T. M., Surman, R., & Wollaeger, R. (2018). The Origin of r-process Elements in the Milky Way. *ApJ*, 855(2), Article 99, 99. <https://doi.org/10.3847/1538-4357/aaad67>
- Coulter, D. A., Foley, R. J., Kilpatrick, C. D., Drout, M. R., Piro, A. L., Shappee, B. J., Siebert, M. R., Simon, J. D., Ulloa, N., Kasen, D., Madore, B. F., Murguia-Berthier, A., Pan, Y. .-, Prochaska, J. X., Ramirez-Ruiz, E., Rest, A., & Rojas-Bravo, C. (2017). Swope Supernova Survey 2017a (SSS17a), the optical counterpart to a gravitational wave source. *Science*, 358(6370), 1556–1558. <https://doi.org/10.1126/science.aap9811>
- Cowan, J. J., & Sneden, C. (2006). Heavy element synthesis in the oldest stars and the early Universe. *Nature*, 440(7088), 1151–1156. <https://doi.org/10.1038/nature04807>
- Cowan, J. J., Sneden, C., Lawler, J. E., Aprahamian, A., Wiescher, M., Langanke, K., Marti*****nez-Pinedo, G., & Thielemann, F.-K. (2021). Origin of the heaviest elements: The rapid neutron-capture

- process. *Reviews of Modern Physics*, 93(1), Article 015002, 015002. <https://doi.org/10.1103/RevModPhys.93.015002>
- Cowan, J. J., & Thielemann, F.-K. (2004). R-process nucleosynthesis in supernovae. *Physics Today*, 57(10), 10.47. <https://doi.org/10.1063/1.1825268>
- Dalcanton, J. J. (2007). The Metallicity of Galaxy Disks: Infall versus Outflow. *ApJ*, 658(2), 941–959. <https://doi.org/10.1086/508913>
- de Avillez, M. A., & Mac Low, M.-M. (2002). Mixing Timescales in a Supernova-driven Interstellar Medium. *ApJ*, 581(2), 1047–1060. <https://doi.org/10.1086/344256>
- De Donder, E., & Vanbeveren, D. (2004). The influence of neutron star mergers on the galactic chemical enrichment of r-process elements. *New A*, 9(1), 1–16. [https://doi.org/10.1016/S1384-1076\(03\)00070-8](https://doi.org/10.1016/S1384-1076(03)00070-8)
- Deason, A. J., Mao, Y.-Y., & Wechsler, R. H. (2016). The Eating Habits of Milky Way-mass Halos: Destroyed Dwarf Satellites and the Metallicity Distribution of Accreted Stars. *ApJ*, 821(1), Article 5, 5. <https://doi.org/10.3847/0004-637X/821/1/5>
- Draine, B. T. (2011). *Physics of the Interstellar and Intergalactic Medium*.
- Dvorkin, I., Daigne, F., Goriely, S., Vangioni, E., & Silk, J. (2021). The impact of turbulent mixing on the galactic r-process enrichment by binary neutron star mergers. *MNRAS*, 506(3), 4374–4388. <https://doi.org/10.1093/mnras/stab2003>
- Eggen, O. J., Lynden-Bell, D., & Sandage, A. R. (1962). Evidence from the motions of old stars that the Galaxy collapsed. *ApJ*, 136, 748. <https://doi.org/10.1086/147433>
- Emerick, A., Bryan, G. L., & Mac Low, M.-M. (2020). Simulating Metal Mixing of Both Common and Rare Enrichment Sources in a Low-mass Dwarf Galaxy. *ApJ*, 890(2), Article 155, 155. <https://doi.org/10.3847/1538-4357/ab6efc>
- Feng, Y., & Krumholz, M. R. (2014). Early turbulent mixing as the origin of chemical homogeneity in open star clusters. *Nature*, 513(7519), 523–525. <https://doi.org/10.1038/nature13662>
- Fielding, D., Quataert, E., Martizzi, D., & Faucher-Giguere, C.-A. (2017). How Supernovae Launch Galactic Winds. 5, 1–5. <https://doi.org/10.1093/mnras1/s1x072>

- Frebel, A. (2010). Stellar archaeology: Exploring the Universe with metal-poor stars. *Astronomische Nachrichten*, 331(5), 474–488. <https://doi.org/10.1002/asna.201011362>
- Frebel, A. (2008). Observing the r-Process Signature in the Oldest Stars. *arXiv e-prints*, Article arXiv:0812.1227, arXiv:0812.1227.
- Frebel, A., & Norris, J. E. (2015). Near-Field Cosmology with Extremely Metal-Poor Stars. *Annual Review of Astronomy and Astrophysics*, 53(1), 631–688. <https://doi.org/10.1146/annurev-astro-082214-122423>
- Gilmore, G., Randich, S., Asplund, M., Binney, J., Bonifacio, P., Drew, J., Feltzing, S., Ferguson, A., Jeffries, R., Micela, G., Negueruela, I., Prusti, T., Rix, H. .-. , Vallenari, A., Alfaro, E., Allende-Prieto, C., Babusiaux, C., Bensby, T., Blomme, R., ... Gaia-ESO Survey Team. (2012). The Gaia-ESO Public Spectroscopic Survey. *The Messenger*, 147, 25–31.
- Goriely, S., Bauswein, A., & Janka, H.-T. (2011). r-process Nucleosynthesis in Dynamically Ejected Matter of Neutron Star Mergers. *ApJ*, 738(2), Article L32, L32. <https://doi.org/10.1088/2041-8205/738/2/L32>
- Hansen, C. J. (2022). Heavy Elements – They came out of the blue. *arXiv e-prints*, Article arXiv:2203.07396, arXiv:2203.07396.
- Haynes, C. J., & Kobayashi, C. (2019). Galactic simulations of r-process elemental abundances. *MNRAS*, 483(4), 5123–5134. <https://doi.org/10.1093/mnras/sty3389>
- Hirai, Y., Beers, T. C., Chiba, M., Aoki, W., Shank, D., Saitoh, T. R., Okamoto, T., & Makino, J. (2022). Origin of highly r-process-enhanced stars in a cosmological zoom-in simulation of a Milky Way-like galaxy. *MNRAS*, 517(4), 4856–4874. <https://doi.org/10.1093/mnras/stac2489>
- Hirai, Y., Ishimaru, Y., Saitoh, T. R., Fujii, M. S., Hidaka, J., & Kajino, T. (2015). Enrichment of r-process Elements in Dwarf Spheroidal Galaxies in Chemo-dynamical Evolution Model. *ApJ*, 814(1), Article 41, 41. <https://doi.org/10.1088/0004-637X/814/1/41>
- Hirai, Y., Ishimaru, Y., Saitoh, T. R., Fujii, M. S., Hidaka, J., & Kajino, T. (2017). Early chemo-dynamical evolution of dwarf galaxies deduced from enrichment of r-process elements. *MNRAS*, 466(2), 2474–2487. <https://doi.org/10.1093/mnras/stw3342>

- Hotokezaka, K., Beniamini, P., & Piran, T. (2018). Neutron star mergers as sites of r-process nucleosynthesis and short gamma-ray bursts. *International Journal of Modern Physics D*, 27(13), Article 1842005, 1842005. <https://doi.org/10.1142/S0218271818420051>
- Hotokezaka, K., Piran, T., & Paul, M. (2015). Short-lived ^{244}Pu points to compact binary mergers as sites for heavy r-process nucleosynthesis. *Nature Physics*, 11(12), 1042. <https://doi.org/10.1038/nphys3574>
- Ishimaru, Y., & Wanajo, S. (1999). Enrichment of the R-Process Element Europium in the Galactic Halo. *ApJ*, 511(1), L33–L36. <https://doi.org/10.1086/311829>
- Ishimaru, Y., Wanajo, S., & Prantzos, N. (2015). Neutron Star Mergers as the Origin of r-process Elements in the Galactic Halo Based on the Sub-halo Clustering Scenario. *ApJ*, 804(2), Article L35, L35. <https://doi.org/10.1088/2041-8205/804/2/L35>
- Janiuk, A. (2017). Microphysics in the Gamma-Ray Burst Central Engine. *ApJ*, 837(1), Article 39, 39. <https://doi.org/10.3847/1538-4357/aa5f16>
- Ji, A. P., Drout, M. R., & Hansen, T. T. (2019). The Lanthanide Fraction Distribution in Metal-poor Stars: A Test of Neutron Star Mergers as the Dominant r-process Site. *ApJ*, 882(1), Article 40, 40. <https://doi.org/10.3847/1538-4357/ab3291>
- Ji, A. P., Frebel, A., Simon, J. D., & Chiti, A. (2016). Complete Element Abundances of Nine Stars in the r-process Galaxy Reticulum II. *ApJ*, 830(2), Article 93, 93. <https://doi.org/10.3847/0004-637X/830/2/93>
- Johnson, J. (n.d.). *Origin of the elements*. <https://www.astronomy.ohio-state.edu/johnson.3064/nucleo/index.html> (accessed: 15.01.2023)
- Johnston, K. V., Bullock, J. S., Sharma, S., Font, A., Robertson, B. E., & Leitner, S. N. (2008). Tracing Galaxy Formation with Stellar Halos. II. Relating Substructure in Phase and Abundance Space to Accretion Histories. *ApJ*, 689(2), 936–957. <https://doi.org/10.1086/592228>
- Kasen, D., Metzger, B., Barnes, J., Quataert, E., & Ramirez-Ruiz, E. (2017). Origin of the heavy elements in binary neutron-star mergers from a gravitational-wave event. *Nature*, 551(7678), 80–84. <https://doi.org/10.1038/nature24453>
- Kim, C. G., & Ostriker, E. C. (2015). Momentum injection by supernovae in the interstellar medium. *Astrophysical Journal*, 802(2), 99. <https://doi.org/10.1088/0004-637X/802/2/99>

- Knödelsder, J. (2003). Supernova Nucleosynthesis. In *Final stages of stellar evolution*.
- Kobayashi, C., Umeda, H., Nomoto, K., Tominaga, N., & Ohkubo, T. (2006). Galactic chemical evolution: Carbon through Zinc. *The Astrophysical Journal*, 653, 1145–1171. <https://doi.org/10.1086/508914>
- Lattimer, J. M., & Schramm, D. N. (1974). Black-Hole-Neutron-Star Collisions. *ApJ*, 192, L145. <https://doi.org/10.1086/181612>
- Li, M., & Bryan, G. L. (2020). Simple Yet Powerful: Hot Galactic Outflows Driven by Supernovae. *ApJ*, 890(2), Article L30, L30. <https://doi.org/10.3847/2041-8213/ab7304>
- MacFadyen, A. I., & Woosley, S. E. (1999). Collapsars: Gamma-Ray Bursts and Explosions in “Failed Supernovae”. *ApJ*, 524(1), 262–289. <https://doi.org/10.1086/307790>
- Macias, P., & Ramirez-Ruiz, E. (2019). Constraining Collapsar r-process Models through Stellar Abundances. *ApJ*, 877(2), Article L24, L24. <https://doi.org/10.3847/2041-8213/ab2049>
- Martizzi, D., Faucher-Giguère, C. A., & Quataert, E. (2015). Supernova feedback in an inhomogeneous interstellar medium. *Monthly Notices of the Royal Astronomical Society*, 450(1), 504–522. <https://doi.org/10.1093/mnras/stv562>
- Martizzi, D., Fielding, D., Faucher-Giguère, C. A., & Quataert, E. (2016). Supernova feedback in a local vertically stratified medium: Interstellar turbulence and galactic winds. *Monthly Notices of the Royal Astronomical Society*, 459(3), 2311–2326. <https://doi.org/10.1093/mnras/stw745>
- Mathews, G. J., Bazan, G., & Cowan, J. J. (1992). Evolution of Heavy-Element Abundances as a Constraint on Sites for Neutron-Capture Nucleosynthesis. *ApJ*, 391, 719. <https://doi.org/10.1086/171383>
- Matteucci, F., & Greggio, L. (1986). Relative roles of type I and II supernovae in the chemical enrichment of the interstellar gas. *A&A*, 154(1-2), 279–287.
- Matteucci, F., Romano, D., Arcones, A., Korobkin, O., & Rosswog, S. (2014). Europium production: neutron star mergers versus core-collapse supernovae. *MNRAS*, 438(3), 2177–2185. <https://doi.org/10.1093/mnras/stt2350>
- Mckee, C. F., & Ostriker, J. P. (1977). A Theory of the Interstellar Medium: Three components regulated by supernova explosions in an inhomogenous substrate. *The Astrophysical Journal*, 218, 148–169.

- McWilliam, A., Preston, G. W., Sneden, C., & Searle, L. (1995). Spectroscopic Analysis of 33 of the Most Metal Poor Stars. II. *AJ*, 109, 2757. <https://doi.org/10.1086/117486>
- Metzger, B. D. (2017). Welcome to the Multi-Messenger Era! Lessons from a Neutron Star Merger and the Landscape Ahead. *arXiv e-prints*, Article arXiv:1710.05931, arXiv:1710.05931.
- Murguia-Berthier, A., Ramirez-Ruiz, E., Kilpatrick, C. D., Foley, R. J., Kasen, D., Lee, W. H., Piro, A. L., Coulter, D. A., Drout, M. R., Madore, B. F., Shappee, B. J., Pan, Y. .-, Prochaska, J. X., Rest, A., Rojas-Bravo, C., Siebert, M. R., & Simon, J. D. (2017). A Neutron Star Binary Merger Model for GW170817/GRB 170817A/SSS17a. *ApJ*, 848(2), Article L34, L34. <https://doi.org/10.3847/2041-8213/aa91b3>
- Naidu, R. P., Conroy, C., Bonaca, A., Zaritsky, D., Weinberger, R., Ting, Y.-S., Caldwell, N., Tacchella, S., Han, J. J., Speagle, J. S., & Cargile, P. A. (2021). Reconstructing the Last Major Merger of the Milky Way with the H₃ Survey. *arXiv e-prints*, Article arXiv:2103.03251, arXiv:2103.03251.
- Nomoto, K., Kobayashi, C., & Tominaga, N. (2013). Nucleosynthesis in Stars and the Chemical Enrichment of Galaxies. *Annual Review of Astronomy and Astrophysics*, 51(1), 457–509. <https://doi.org/10.1146/annurev-astro-082812-140956>
- Pan, L., & Scannapieco, E. (2010). Mixing in Supersonic Turbulence. *ApJ*, 721(2), 1765–1782. <https://doi.org/10.1088/0004-637X/721/2/1765>
- Pan, L., Scannapieco, E., & Scalo, J. (2012). The pollution of pristine material in compressible turbulence. *Journal of Fluid Mechanics*, 700, 459–489. <https://doi.org/10.1017/jfm.2012.143>
- Ramirez-Ruiz, E., Trenti, M., MacLeod, M., Roberts, L. F., Lee, W. H., & Saladino-Rosas, M. I. (2015). Compact Stellar Binary Assembly in the First Nuclear Star Clusters and r-process Synthesis in the Early Universe. *ApJ*, 802(2), Article L22, L22. <https://doi.org/10.1088/2041-8205/802/2/L22>
- Recchi, S., Calura, F., & Kroupa, P. (2009). The chemical evolution of galaxies within the IGIMF theory: the [α/Fe] ratios and downsizing. *A&A*, 499(3), 711–722. <https://doi.org/10.1051/0004-6361/200811472>

- Recchi, S., Matteucci, F., & D'Ercole, A. (2001). Dynamical and chemical evolution of gas-rich dwarf galaxies. *MNRAS*, 322(4), 800–820. <https://doi.org/10.1046/j.1365-8711.2001.04189.x>
- Roberts, L. F., Kasen, D., Lee, W. H., & Ramirez-Ruiz, E. (2011). Electromagnetic Transients Powered by Nuclear Decay in the Tidal Tails of Coalescing Compact Binaries. *ApJ*, 736(1), Article L21, L21. <https://doi.org/10.1088/2041-8205/736/1/L21>
- Robertson, B., Bullock, J. S., Font, A. S., Johnston, K. V., & Hernquist, L. (2005). A Cold Dark Matter, Stellar Feedback, and the Galactic Halo Abundance Pattern. *ApJ*, 632(2), 872–881. <https://doi.org/10.1086/452619>
- Roederer, I. U., Sneden, C., Lawler, J. E., Sobek, J. S., Cowan, J. J., & Boesgaard, A. M. (2018). Consistent Iron Abundances Derived from Neutral and Singly Ionized Iron Lines in Ultraviolet and Optical Spectra of Six Warm Metal-poor Stars. *ApJ*, 860(2), Article 125, 125. <https://doi.org/10.3847/1538-4357/aac6df>
- Rosswog, S., Davies, M. B., Thielemann, F. .-, & Piran, T. (2000). Merging neutron stars: asymmetric systems. *A&A*, 360, 171–184.
- Rosswog, S., Liebendörfer, M., Thielemann, F. .-, Davies, M. B., Benz, W., & Piran, T. (1999). Mass ejection in neutron star mergers. *A&A*, 341, 499–526.
- Ryan, S. G., Norris, J. E., & Beers, T. C. (1996). Extremely Metal-poor Stars. II. Elemental Abundances and the Early Chemical Enrichment of the Galaxy. *ApJ*, 471, 254. <https://doi.org/10.1086/177967>
- Safarzadeh, M., Sarmiento, R., & Scannapieco, E. (2019). On Neutron Star Mergers as the Source of r-process-enhanced Metal-poor Stars in the Milky Way. *ApJ*, 876(1), Article 28, 28. <https://doi.org/10.3847/1538-4357/ab1341>
- Santistevan, I. B., Wetzell, A., Sanderson, R. E., El-Badry, K., Samuel, J., & Faucher-Giguère, C.-A. (2021). The origin of metal-poor stars on prograde disc orbits in FIRE simulations of Milky Way-mass galaxies. *MNRAS*, 505(1), 921–938. <https://doi.org/10.1093/mnras/stab1345>
- Scalo, J., & Elmegreen, B. G. (2004). Interstellar Turbulence II: Implications and Effects. *ARA&A*, 42(1), 275–316. <https://doi.org/10.1146/annurev.astro.42.120403.143327>
- Searle, L., & Zinn, R. (1978). Composition of halo clusters and the formation of the galactic halo. *ApJ*, 225, 357–379. <https://doi.org/10.1086/156499>

- Shank, D., Beers, T. C., Placco, V. M., Gudin, D., Catapano, T., Holmbeck, E. M., Ezzeddine, R., Roederer, I. U., Sakari, C. M., Frebel, A., & Hansen, T. T. (2022). The R-Process Alliance: Chemo-Dynamically Tagged Groups II. An Extended Sample of Halo *r*-Process-Enhanced Stars. *arXiv e-prints*, Article arXiv:2208.09712, arXiv:2208.09712.
- Shen, S., Cooke, R. J., Ramirez-Ruiz, E., Madau, P., Mayer, L., & Guedes, J. (2015). THE HISTORY of R-PROCESS ENRICHMENT in the MILKY WAY. *Astrophysical Journal*, 807(2), 115. <https://doi.org/10.1088/0004-637X/807/2/115>
- Siegel, D. M. (2019). GW170817 -the first observed neutron star merger and its kilonova: Implications for the astrophysical site of the r-process. *European Physical Journal A*, 55(11), Article 203, 203. <https://doi.org/10.1140/epja/i2019-12888-9>
- Siegel, D. M., Barnes, J., & Metzger, B. D. (2019). Collapsars as a major source of r-process elements. *Nature*, 569(7755), 241–244. <https://doi.org/10.1038/s41586-019-1136-0>
- Siegel, D. M., & Metzger, B. D. (2017). Three-Dimensional General-Relativistic Magnetohydrodynamic Simulations of Remnant Accretion Disks from Neutron Star Mergers: Outflows and *r*-Process Nucleosynthesis. *Phys. Rev. Lett.*, 119(23), Article 231102, 231102. <https://doi.org/10.1103/PhysRevLett.119.231102>
- Simonetti, P., Matteucci, F., Greggio, L., & Cescutti, G. (2019). A new delay time distribution for merging neutron stars tested against Galactic and cosmic data. *MNRAS*, 486(2), 2896–2909. <https://doi.org/10.1093/mnras/stz991>
- Snedden, C., Cowan, J. J., & Gallino, R. (2008). Neutron-capture elements in the early galaxy. *ARA&A*, 46, 241–288. <https://doi.org/10.1146/annurev.astro.46.060407.145207>
- Snedden, C., McWilliam, A., Preston, G. W., Cowan, J. J., Burris, D. L., & Armosky, B. J. (1996). The Ultra-Metal-poor, Neutron-Capture-rich Giant Star CS 22892-052. *ApJ*, 467, 819. <https://doi.org/10.1086/177656>
- Spitoni, E., Matteucci, F., Recchi, S., Cescutti, G., & Pipino, A. (2009). Effects of galactic fountains and delayed mixing in the chemical evolution of the Milky Way. *A&A*, 504(1), 87–96. <https://doi.org/10.1051/0004-6361/200911768>
- Suess, H. E., & Urey, H. C. (1956). Abundances of the Elements. *Reviews of Modern Physics*, 28(1).

- Symbalisty, E., & Schramm, D. N. (1982). Neutron Star Collisions and the r-Process. *Astrophys. Lett.*, 22, 143.
- Takahashi, K., Witt, J., & Janka, H. -. (1994). Nucleosynthesis in neutrino-driven winds from protoneutron stars II. The r-process. *A&A*, 286, 857–869.
- Taylor, G. (1950). The Formation of a Blast Wave by a Very Intense Explosion I. Theoretical discussion. *Proceedings of the Royal Society A: Mathematical, Physical and Engineering Sciences*, 201(1065), 175–186. <https://doi.org/10.1098/rspa.1950.0050>
- Thielemann, F.-K., Eichler, M., Panov, I., Pignatari, M., & Wehmeyer, B. (2017). Making the Heaviest Elements in a Rare Class of Supernovae. In A. W. Alsabti & P. Murdin (Eds.), *Handbook of supernovae* (p. 1843). https://doi.org/10.1007/978-3-319-21846-5_81
- Thornton, K., Gaudlitz, M., Janka, H.-T., & Steinmetz, M. (1998). Energy Input and Mass Redistribution by Supernovae in the Interstellar Medium. *The Astrophysical Journal*, 500(1), 95–119. <https://doi.org/10.1086/305704>
- Timmes, F. X., Woosley, S. E., & Weaver, T. A. (1995). Galactic Chemical Evolution: Hydrogen through Zinc. *ApJS*, 98, 617. <https://doi.org/10.1086/192172>
- Travaglio, C., Galli, D., Gallino, R., Busso, M., Ferrini, F., & Straniero, O. (1999). Galactic Chemical Evolution of Heavy Elements: From Barium to Europium. *ApJ*, 521(2), 691–702. <https://doi.org/10.1086/307571>
- Tumlinson, J., Peeples, M. S., & Werk, J. K. (2017). The Circumgalactic Medium. *Annual Review of Astronomy and Astrophysics*, 55(1), 389–432. <https://doi.org/10.1146/annurev-astro-091916-055240>
- van de Voort, F., Pakmor, R., Bieri, R., & Grand, R. J. J. (2022). The impact of natal kicks on galactic r-process enrichment by neutron star mergers. *MNRAS*, 512(4), 5258–5268. <https://doi.org/10.1093/mnras/stac710>
- van de Voort, F., Pakmor, R., Grand, R. J. J., Springel, V., Gómez, F. A., & Marinacci, F. (2020). Neutron star mergers and rare core-collapse supernovae as sources of r-process enrichment in simulated galaxies. *MNRAS*, 494(4), 4867–4883. <https://doi.org/10.1093/mnras/staa754>
- van de Voort, F., Quataert, E., Hopkins, P. F., Kereš, D., & Faucher-Giguère, C.-A. (2015). Galactic r-process enrichment by neutron star mergers in cosmological

- simulations of a Milky Way-mass galaxy. *Monthly Notices of the Royal Astronomical Society*, 447(1), 140–148. <https://doi.org/10.1093/mnras/stu2404>
- Vangioni, E., Goriely, S., Daigne, F., François, P., & Belczynski, K. (2016). Cosmic neutron-star merger rate and gravitational waves constrained by the r-process nucleosynthesis. *MNRAS*, 455(1), 17–34. <https://doi.org/10.1093/mnras/stv2296>
- Wanajo, S., & Ishimaru, Y. (2006). r-process calculations and Galactic chemical evolution. *Nucl. Phys. A*, 777, 676–699. <https://doi.org/10.1016/j.nuclphysa.2005.10.012>
- Wang, Y., Nadler, E. O., Mao, Y.-Y., Adhikari, S., Wechsler, R. H., & Behroozi, P. (2021). UniverseMachine: Predicting Galaxy Star Formation over Seven Decades of Halo Mass with Zoom-in Simulations. *arXiv e-prints*, Article arXiv:2102.11876, arXiv:2102.11876.
- Watson, D., Hansen, C. J., Selsing, J., Koch, A., Malesani, D. B., Andersen, A. C., Fynbo, J. P. U., Arcones, A., Bauswein, A., Covino, S., Grado, A., Heintz, K. E., Hunt, L., Kouveliotou, C., Leloudas, G., Levan, A. J., Mazzali, P., & Pian, E. (2019). Identification of strontium in the merger of two neutron stars. *Nature*, 574(7779), 497–500. <https://doi.org/10.1038/s41586-019-1676-3>
- Wehmeyer, B., Fröhlich, C., Côté, B., Pignatari, M., & Thielemann, F. -. (2019). Using failed supernovae to constrain the Galactic r-process element production. *MNRAS*, 487(2), 1745–1753. <https://doi.org/10.1093/mnras/stz1310>
- Wehmeyer, B., Pignatari, M., & Thielemann, F. -. (2015). Galactic evolution of rapid neutron capture process abundances: the inhomogeneous approach. *MNRAS*, 452(2), 1970–1981. <https://doi.org/10.1093/mnras/stv1352>
- Wheeler, J. C., Cowan, J. J., & Hillebrandt, W. (1998). The r-Process in Collapsing O/Ne/Mg Cores. *ApJ*, 493(2), L101–L104. <https://doi.org/10.1086/311133>
- Wheeler, J. C., Sneden, C., & Truran, J., James W. (1989). Abundance ratios as a function of metallicity. *ARA&A*, 27, 279–349. <https://doi.org/10.1146/annurev.aa.27.090189.001431>
- Woosley, S. E. (1993). Gamma-Ray Bursts from Stellar Mass Accretion Disks around Black Holes. *ApJ*, 405, 273. <https://doi.org/10.1086/172359>

- Woosley, S. E., Wilson, J. R., Mathews, G. J., Hoffman, R. D., & Meyer, B. S. (1994). The r-Process and Neutrino-heated Supernova Ejecta. *ApJ*, 433, 229. <https://doi.org/10.1086/174638>
- Woosley, S., & Weaver, T. A. (1995). The evolution and explosion of massive stars II. Explosive hydrodynamics and nucleosynthesis. *The Astrophysical Journal*, 101, 181–235.
- Xiang, M., & Rix, H.-W. (2022). A time-resolved picture of our Milky Way's early formation history. *Nature*, 603(7902), 599–603. <https://doi.org/10.1038/s41586-022-04496-5>
- Yang, C. C., & Krumholz, M. (2012). Thermal-instability-driven turbulent mixing in galactic disks. I. Effective mixing of metals. *Astrophysical Journal*, 758(1), 1–35. <https://doi.org/10.1088/0004-637X/758/1/48>